Abstract

BOND, RYAN BOMAR. Reynolds-Averaged Navier-Stokes Analysis of the Flow through a Model Rocket-Based Combined Cycle Engine with an Independently-Fueled Ramjet Stream. (Under the direction of Dr. Jack R. Edwards and Dr. D. Scott McRae.)

A new concept for the low speed propulsion mode in rocket based combined cycle (RBCC) engines has been developed as part of the NASA GTX program. This concept, called the independent ramjet stream (IRS) cycle, is a variation of the traditional ejector ramjet (ER) design and involves the injection of hydrogen fuel directly into the air stream, where it is ignited by the rocket plume. Experiments and computational fluid dynamics (CFD) are currently being used to evaluate the feasibility of the new design. In this work, a Navier-Stokes code valid for general reactive flows is applied to the model engine under cold flow, ejector ramjet, and IRS cycle operation. Pressure distributions corresponding to cold-flow and ejector ramjet operation are compared with experimental data. The engine response under independent ramjet stream cycle operation is examined for different reaction models and grid sizes. The engine response to variations in fuel injection is also examined. Mode transition simulations are also analyzed both with and without a nitrogen purge of the rocket. The solutions exhibit a high sensitivity to both grid resolution and reaction mechanism, but they do indicate that thermal throat ramjet operation is possible through the injection and burning of additional fuel into the air stream. The solutions also indicate that variations in fuel injection location can affect the position of the thermal throat. The numerical simulations predicted successful mode transition both with and without a nitrogen purge of the rocket; however, the reliability of the mode transition results cannot be established without experimental data to validate the reaction mechanism.

Reynolds-Averaged Navier-Stokes Analysis of the Flow through a Model Rocket-Based Combined Cycle Engine with an Independently-Fueled Ramjet Stream

by

Ryan Bomar Bond

A dissertation submitted to the graduate faculty of
North Carolina State University
in partial fulfillment of the requirements for the degree of
Doctor of Philosophy

Department of Mechanical and Aerospace Engineering
Raleigh, North Carolina
August 13, 2003

Approved by:

Dr. Jack R. Edwards (co-chair)	Dr. D. Scott McRae (co-chair)
Dr. Hassan A. Hassan	Dr. C. Timothy Kelley

Biography

Ryan Bomar Bond was born on January 6, 1976, in Fredricksburg, Virginia, to David and Celia Bond. Ryan became a Christian in 1988 and graduated from Tullahoma High School in 1994. He later received Bachelor of Science degrees in Aerospace Engineering and Mathematics from Mississippi State University in 1998. On May 30, 1998, Ryan married Rucha Sandip Shukla. Ryan finished his Master of Science degree in Aerospace engineering at North Carolina State University in 2001. Following the completion of his Doctor of Philosophy in Aerospace Engineering, Ryan will begin work at Sandia National Laboratories in Albuquerque, New Mexico.

Acknowledgments

I would like to thank my loving wife, Rucha, who has been supportive of me and my work throughout my career as a student. I would also like to thank my parents who guided me in my first steps of education, faith, and life.

I would like to thank Dr. and Mrs. Donald C. Moreland for providing opportunities to me through the Frank C. Ziglar, Jr. Endowed Graduate Fellowship. Their generosity cannot be understated.

I would like to thank my advisors, Dr. Jack R. Edwards and Dr. D. Scott McRae, for training me in the ways of CFD and giving me the skills and knowledge to accomplish my goals. I would also like to thank my other committee members, Dr. Hassan A. Hassan and Dr. C. Timothy Kelley, for their service on my committee and for their time as instructors. I would like to thank the other faculty members of the MAE and Math departments for their classroom instruction and help with research. Last, but definitely not least, I would like to thank all of the students who spent time in Broughton 4216 during the 5+ years I was there.

I would like to thank the North Carolina Supercomputing Center, which provided computational resources for this work, and NASA Glenn Research Center, which provided funding under grant number NAG3-2658. Specifically, at Glenn, I would like to thank Dr. Hani Kamhawi and Christopher J. Steffen for all of their assistance.

I would like to thank the countless others who have had an influence on my career, especially Dr. Bharat K. Soni, Dr. Robert H. Nichols, and Brent L. Bates.

Table of Contents

List of Tables

List of Figures

List of Symbols

Roman Symbols

a	speed of sound, turbulence model coefficient
A	Arrhenius rate coefficient
c	molar density
C_p	specific heat at constant pressure
C,D,P	LDFSS coefficients
D	molecular diffusivity
Da	Damköhler number
e	internal energy
E,F,G	flux vectors
F	blending function
G	reaction progress variable
h	enthalpy
J	Jacobian of coordinate transformation
$J_{m,j}$	diffusion flux for species m
k	turbulence kinetic energy, reaction rate coefficient
l	integral length scale
l_F	laminar flame thickness
$\dot{m}$	mass flow rate, lbm/s
M	Mach number, molecular mass

MR	mass ratio
NS	number of species
p	pressure
q_j	heat flux vector
Q_i	turbulent heat flux vector
R	gas constant
RR	reaction rate
$\mathcal{R}$	universal gas constant
s	flame speed
S	source vector
Sc	Schmidt number
T	temperature, time interval
$\mathcal{T}_{i,j}$	turbulent stress tensor
t	time
(TB)	third body efficiency
u,v,w	Cartesian velocity components
U,V,W	diffusive velocity components
$\mathcal{U},\mathcal{V},\mathcal{W}$	contravariant velocity components
u_j	velocity vector
U	vector of conserved variables
$V_j^{(m)}$	diffusive velocity, species m
v'	turbulence intensity
$\dot{w}$	chemical source term

W	vector of primitive variables
x_j	position vector
x, y, z	Cartesian body axes
Y	mass fraction
$\Upsilon_{m,j}$	turbulent diffusive flux vector for species m

Greek Symbols

α	molecular heat transfer coefficient
α, β	LDFSS coefficients
$\beta, \kappa, \sigma, \gamma$	turbulence model coefficients
$\delta_{i,j}$	Kronecker delta
ϕ	equivalence ratio
ε	dissipation per unit mass
γ	thermal conductivity, ratio of specific heats
μ	viscosity
ν	stoichiometric coefficient, kinematic viscosity
ρ	density
$\tau_{i,j}$	stress tensor
ξ, η, ζ	curvilinear coordinates
ω	specific dissipation rate

Subscripts

0	reference value
½	interface value
c	chamber
e	exit state
i	inlet state
L,R	left/right cell values
mix	mixture value
ref	reference value
t	total value
T	turbulent quantity
v	viscous quantity

Introduction

The NASA GTX concept vehicle is a single-stage-to-orbit (SSTO) design which incorporates rocket-based combined cycle (RBCC) engines. The GTX is one of several designs intended to demonstrate SSTO capability and evaluate RBCC technology. An artist's concept of the GTX vehicle is given in Figure 1.

Figure 1: Conceptual drawing of GTX launch vehicle

The RBCC engines incorporated on the GTX are intended to operate in four modes. The first mode, used from liftoff to Mach 2.5, is the independent ramjet stream (IRS) cycle. In the IRS mode, hydrogen fuel is injected into the inlet diffuser section, where it mixes with the incoming air. This fuel-air stream then meets the rocket exhaust in the combustor section. The rocket motor provides thrust and acts as an ignition source for the fuel-air mixture. The rocket motor is typically run fuel rich, although not as rich as a conventional ejector ramjet (ER) design, in which no fuel injection occurs. In a

conventional ER design, all of the fuel for the ramjet stream is contained within the rocket exhaust. Figure 2 shows a schematic of the engine design operating in IRS mode. The rocket plume is referred to as the "primary" stream, and the fuel-air mixture entering the combustor section via the isolator is referred to as the "secondary" stream. At lower inlet mass flow rates, the majority of the engine mass flow is contained within the primary stream, but as the vehicle accelerates, the secondary stream eventually becomes more significant than the primary stream. A key requirement for the IRS concept is the ability to establish thermal-throat ramjet operation in the secondary stream within the allowable combustor length. It is also believed that the position of the thermal throat may be modulated by varying the location and rate of secondary fuel injection.

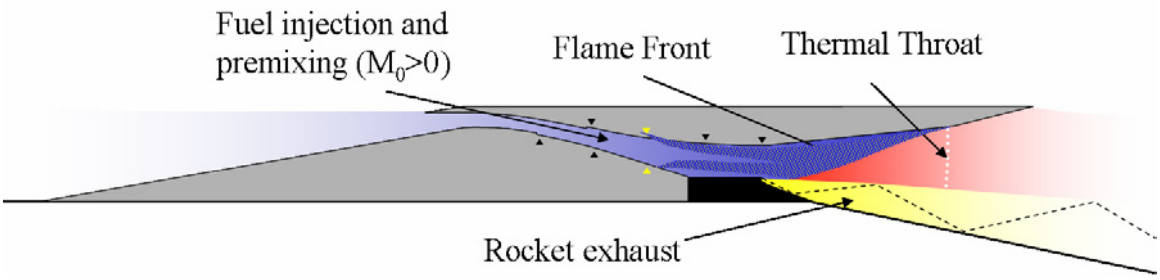

Figure 2: Engine operating in IRS mode

As the launch vehicle gains speed and altitude, the rocket motor produces a smaller percentage of thrust, and its flame holding capability becomes unnecessary. The rocket is gradually throttled back until, at around Mach 2.5, the rocket motor is shut off completely. This point is the transition from mode 1 to mode 2, which is a pure ramjet mode. This ramjet mode remains efficient until around Mach 5.5, when supersonic

combustion becomes more practical. The transition from ramjet to scramjet is induced by a centerbody translation. This change in the inlet geometry allows for fully supersonic flow throughout the combustor. At around Mach 11, it is necessary to turn the rocket motor back on to maintain thrust. The centerbody is then translated again to close the inlet completely. The rocket provides all of the thrust for the remainder of the ascent. More details about the GTX propulsion system's operation are given by Trefny.[1]

The IRS cycle is expected to have several advantages over the conventional ER cycle. ER designs typically require long combustor sections to allow for mixing of the fuel rich rocket exhaust with the incoming air, burning, and establishment of a thermal throat. The IRS cycle could potentially allow for a shorter combustor section, since much of the fuel would be premixed with the incoming air stream. Burning in premixed or partially-premixed mode can result in flame propagation across the extent of the combustor and more rapid heat release.[2] Most ER designs employ multiple small rockets to enhance mixing, but the IRS design is more structurally efficient because it allows for a single large rocket. The IRS cycle is also expected to allow better transition into pure ramjet mode since fewer changes in the engine flow path would be necessary for IRS-to-ramjet transition than for ER-to-ramjet transition.

A scaled down version of the GTX RBCC engine has been constructed and installed at the direct-connect facility at NASA Glenn Research Center. The model engine consists of a translating centerbody mounted on a flat plate and surrounded by a contoured cowl. Both the centerbody and cowl are semicircular in cross section. The forward section of the centerbody mimics the area ratio profile of the full-sized GTX engine design. A backward-facing step behind the centerbody's point of maximum

diameter provides an isolator region for fuel injection and mixing. A combustor section with a divergence half-angle of five degrees is connected to the cowl. The rocket motor is located within the centerbody, and the plume exhausts parallel to the flat plate. Two fuel injector banks are located in the isolator region. Each bank consists of 11 fuel injectors which are equally spaced around the circumference of the cowl. The injectors are all 0.2 inches in diameter. These fuel injectors allow for IRS operation of the engine. ER operation is accomplished by not injecting any fuel. More details of the test apparatus and experimental results obtained are given by Kamhawi, *et. al*.[3] Figure 3 shows the experimental setup. Note that the engine is inverted.

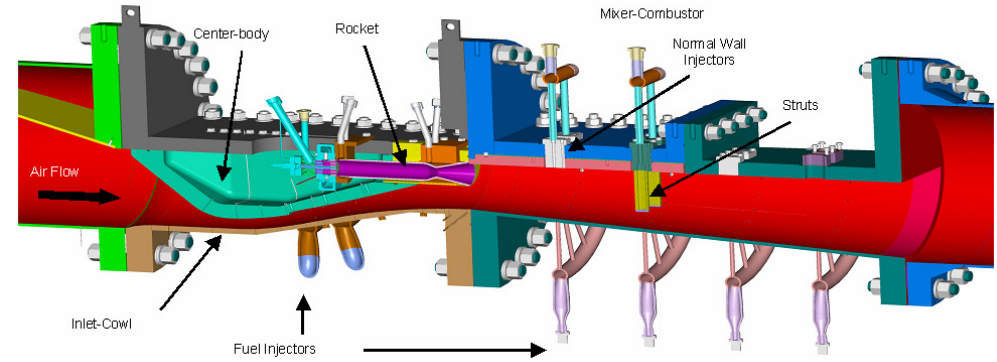

Figure 3: Experimental test apparatus

The present work focuses on simulating the flow within this model engine. The purpose of the CFD work is to understand the flow and combustion physics during IRS and ER operation and in transition to pure ramjet mode. The CFD work began with an attempt to match experimental cold-flow data.[4] The work then progressed into

simulation of ER and steady IRS operation.[5] All of these results and the results of unsteady IRS operation are discussed in this dissertation.

Numerical Methods

The Navier-Stokes Equations

The Navier-Stokes equations govern the dynamics of viscous fluids. If thermal equilibrium is assumed and body forces and radiative heat transfer are neglected, then the Navier-Stokes equations for a compressible, multi-species, reacting mixture can be expressed as follows[6]:

$$\frac{\partial \rho}{\partial t} + \frac{\partial (\rho u_j)}{\partial x_j} = 0$$

$$\frac{\partial (\rho Y_m)}{\partial t} + \frac{\partial (\rho Y_m u_j)}{\partial x_j} = \frac{\partial J_{m,j}}{\partial x_j} + \dot{w}_m$$

$$\frac{\partial (\rho u_i)}{\partial t} + \frac{\partial (\rho u_i u_j)}{\partial x_j} = -\frac{\partial (p\delta_{ij})}{\partial x_j} + \frac{\partial \tau_{ij}}{\partial x_j}$$

$$\frac{\partial (\rho e_t)}{\partial t} + \frac{\partial (\rho h_t u_j)}{\partial x_j} = \frac{\partial (q_j + \tau_{ji} u_i)}{\partial x_j}$$

The diffusive flux, $J_{m,j}$, diffusion velocity of species m, $V_j^{(m)}$, stress tensor, τ_{ij}, and heat flux vector, q_j, are given as follows:

$$J_{m,j} = -\rho_m V_j^{(m)}$$

$$V_j^{(m)} = -\left(\frac{D}{Y_m}\right)\left(\frac{\partial (Y_m)}{\partial x_j}\right)$$

$$\tau_{ij} = \mu\left(\frac{\partial u_i}{\partial x_j} + \frac{\partial u_j}{\partial x_i}\right) - \tfrac{2}{3}\delta_{ij}\mu\frac{\partial u_k}{\partial x_k}$$

$$q_j = \gamma\frac{\partial T}{\partial x_j} - \rho\sum_{m=1}^{NS} h_m Y_m V_j^{(m)}$$

In the preceding equations, μ is the molecular viscosity, γ is the coefficient of thermal conductivity, D is the molecular diffusivity, Y_m is the mass fraction for species *m*, and *NS* is the number of species. The total enthalpy and total energy are defined as follows:

$$h_t = h_{mix} + \tfrac{1}{2}u_i u_i$$

$$e_t = h_t - \frac{p}{\rho}$$

where h_{mix} is the static enthalpy of the mixture. The following thermodynamic relations are necessary to close this set of transport equations[7]:

$$\rho = \sum_{m=1}^{NS}\rho_m$$

$$Y_m = \frac{\rho_m}{\rho}$$

$$p = \rho R_{mix} T$$

$$R_{mix} = \mathcal{R}\sum_{m=1}^{NS}\frac{Y_m}{M_m}$$

$$h_{mix} = \sum_{m=1}^{NS} h_m Y_m$$

$$h_m = h_{f,m}^0 + \int_{T_{ref}}^{T} C_{p,m}(T')dT'$$

$$a = \sqrt{\frac{C_{p,mix} p}{(C_{p,mix} - R_{mix})\rho}}$$

$$D = \frac{\mu}{Sc\rho}$$

$$C_{p,mix} = \sum_{m=1}^{NS} Y_m C_{p,m}(T)$$

where $\mathcal{R}$ is the universal gas constant, M_m is the molecular mass of species m, S_c is the Schmidt number, $h^0_{f,m}$ is the heat of formation for species m, and $C_{p,m}$ is the specific heat at constant pressure for species m. $C_{p,m}$ is calculated as a function of temperature using the fifth-order polynomial of McBride, *et. al*.[8] The molecular viscosity and thermal conductivity for each species are determined as follows from Sutherland's law:

$$\frac{\mu}{\mu_0} \approx \left(\frac{T}{T_{0,\mu}}\right)^{\frac{3}{2}} \frac{T_{0,\mu} + S_\mu}{T + S_\mu}$$

$$\frac{\gamma}{\gamma_0} \approx \left(\frac{T}{T_{0,\gamma}}\right)^{\frac{3}{2}} \frac{T_{0,\gamma} + S_\gamma}{T + S_\gamma}$$

The constants μ_0, $T_{0,\mu}$, S_μ, γ_0, $T_{0,\gamma}$, and S_γ are given in White.[9] The mixture values are determined by Wilke's law:[10]

$$\mu_{mix} = \sum_{l=1}^{NS} \left(\frac{\mu_l}{1 + \frac{1}{c_l} \sum_{\substack{m=1 \\ m \neq l}}^{NS} c_m \phi_{lm}} \right)$$

$$\gamma_{mix} = \sum_{l=1}^{NS} \left(\frac{\gamma_l}{1 + \frac{1.065}{c_l} \sum_{\substack{m=1 \\ m \neq l}}^{NS} c_m \phi_{lm}} \right)$$

where c_s is the molar density of species s, ρ_s / M_s, and ϕ_{lm} is given by

$$\phi_{lm} = \frac{\left[1 + \left(\frac{\mu_l}{\mu_m} \frac{\rho_m}{\rho_l} \right)^{1/2} \left(\frac{M_l}{M_m} \right)^{1/4} \right]^2}{\left[8 \left(1 + \frac{M_l}{M_m} \right) \right]^{1/2}}$$

The five transport equations can be written in vector form as follows:

$$\frac{\partial U}{\partial t} + \frac{\partial \mathbf{E}}{\partial x} + \frac{\partial \mathbf{F}}{\partial y} + \frac{\partial \mathbf{G}}{\partial z} = S$$

where

$$U = \begin{pmatrix} \rho_1 \\ \vdots \\ \rho_{NS} \\ \rho u \\ \rho v \\ \rho w \\ \rho e_t \end{pmatrix}$$

$$\mathbf{E} = E - E_v = \begin{pmatrix} \rho_1 u \\ \vdots \\ \rho_{NS} u \\ \rho u^2 + p \\ \rho uv \\ \rho wu \\ \rho h_t u \end{pmatrix} - \begin{pmatrix} \rho_1 U^{(1)} \\ \vdots \\ \rho_{NS} U^{(NS)} \\ \tau_{xx} \\ \tau_{yx} \\ \tau_{zx} \\ u\tau_{xx} + v\tau_{xy} + w\tau_{xz} + q_x \end{pmatrix}$$

$$\mathbf{F} = F - F_v = \begin{pmatrix} \rho_1 v \\ \vdots \\ \rho_{NS} v \\ \rho uv \\ \rho v^2 + p \\ \rho vw \\ \rho h_t v \end{pmatrix} - \begin{pmatrix} \rho_1 V^{(1)} \\ \vdots \\ \rho_{NS} V^{(NS)} \\ \tau_{xy} \\ \tau_{yy} \\ \tau_{zy} \\ u\tau_{yx} + v\tau_{yy} + w\tau_{yz} + q_y \end{pmatrix}$$

$$\mathbf{G} = G - G_v = \begin{pmatrix} \rho_1 w \\ \vdots \\ \rho_{NS} w \\ \rho uw \\ \rho vw \\ \rho w^2 + p \\ \rho h_t w \end{pmatrix} - \begin{pmatrix} \rho_1 W^{(1)} \\ \vdots \\ \rho_{NS} W^{(NS)} \\ \tau_{xz} \\ \tau_{yz} \\ \tau_{zz} \\ u\tau_{zx} + v\tau_{zy} + w\tau_{zz} + q_z \end{pmatrix}$$

$$S = \begin{pmatrix} \dot{w}_1 \\ \vdots \\ \dot{w}_{NS} \\ 0 \\ 0 \\ 0 \\ 0 \end{pmatrix}$$

Reynolds and Favre Averaging of the Navier-Stokes Equations

Because the resolution of the numerical grid is not sufficient to accurately simulate turbulent fluctuations in the flow variables, the Reynolds-Averaged Navier-Stokes (RANS) approach averages certain flow variables to remove the fluctuating components from the set of five transport equations. The effect of these fluctuating components is then re-introduced using a turbulence model. Reynolds averaging is a

basic time average over the interval ($t,t+T$). The following relation averages the function $f(x_i,t)$ to produce the function $\bar{f}(x_i)$ [9,11]:

$$\bar{f}(x_i) = \frac{1}{\rho}\lim_{T\to\infty}\frac{1}{T}\int_{t}^{t+T}\rho f(x_i,t')dt'$$

The quantity f, can then be expressed in terms of its averaged component, $\bar{f}$, and its fluctuating component, f'.

$$f = \bar{f} + f'$$

Although the definition is given in terms of T tending toward infinity, such a formulation is only useful for steady flow problems. For unsteady problems, the interval T is assumed to be significantly larger than the time scales associated with turbulence but significantly smaller than the time scales associated with mean property variations.

Reynolds averaging the entire equation set results in a more complex formulation than if Reynolds averaging is used in conjunction with Favre averaging. Favre averaging is a density weighted average which can be expressed either as an integral or in terms of the Reynolds average[11]:

$$\tilde{f}(x_i) = \frac{1}{\rho}\lim_{T\to\infty}\frac{1}{\Delta t}\int_{t}^{t+T}\rho f(x_i,t')dt' = \frac{\overline{\rho f}}{\bar{\rho}}$$

The quantity, f, can then be expressed in terms of a Favre-averaged component, $\tilde{f}$, and a Favre-fluctuating component, f''.

$$f = \tilde{f} + f''$$

If Favre averaging is applied to the variables e_t, u_j, Y_m, h_t, T, and $u_j^{(m)}$, and Reynolds averaging is applied to the remaining terms in the transport equations, then the following form of the governing equations is obtained[7]:

$$\frac{\partial \overline{\rho}}{\partial t} + \frac{\partial (\overline{\rho}\widetilde{u}_j)}{\partial x_j} = 0$$

$$\frac{\partial (\overline{\rho}\widetilde{Y}_m)}{\partial t} + \frac{\partial (\overline{\rho}\widetilde{Y}_m\widetilde{u}_j)}{\partial x_j} = \frac{\partial (\overline{\rho}\widetilde{V}_j^{(m)} + \Upsilon_{m,j})}{\partial x_j} + \overline{\dot{w}}_m$$

$$\frac{\partial (\overline{\rho}\widetilde{u}_i)}{\partial t} + \frac{\partial (\overline{\rho}\widetilde{u}_i\widetilde{u}_j)}{\partial x_j} = -\frac{\partial (p\delta_{ij} + \overline{\tau}_{ij} + \Upsilon_{ij})}{\partial x_j}$$

$$\frac{\partial (\overline{\rho}\widetilde{e}_t)}{\partial t} + \frac{\partial (\overline{\rho}\widetilde{h}_t\widetilde{u}_j)}{\partial x_j} = \frac{\partial (\overline{q}_j + \widetilde{u}\,\overline{\tau}_{ji} + Q_j)}{\partial x_j}$$

with auxiliary relations

$$\Upsilon_{m,j} = \overline{\rho Y_m'' u_j''}$$

$$\Upsilon_{ij} = -\overline{\rho u_i'' u_j''}$$

$$Q_j = -\overline{\rho u_i'' u_j''} - \widetilde{u}_i \Upsilon_{ji} = q_{t,j} - \widetilde{u}_i \Upsilon_{ji}$$

$$\overline{\rho}\widetilde{E}_t = \overline{\rho}\sum_{m=1}^{NS} \widetilde{Y}_m \widetilde{h}_m(\widetilde{T}) - \overline{p} + \tfrac{1}{2}\overline{\rho}\sum_{j=1}^{NS} \widetilde{u}_j\widetilde{u}_j$$

$$\overline{\rho}\widetilde{h}_t = \overline{\rho}\widetilde{e}_t + \overline{p}$$

The mean laminar stress tensor, heat flux, and diffusion velocities are given as follows:

$$\overline{\tau}_{ij} = \mu\left(\frac{\partial \widetilde{u}_i}{\partial x_j} + \frac{\partial \widetilde{u}_j}{\partial x_i}\right) - \tfrac{1}{2}\delta_{ij}\mu\frac{\partial \widetilde{u}_k}{\partial x_k}$$

$$\overline{q}_j = \gamma\frac{\partial \widetilde{T}}{\partial x_j} - \sum_{m=1}^{NS} \overline{\rho}\widetilde{h}_m\widetilde{Y}_m\widetilde{V}_j^{(m)}$$

$$\widetilde{V}_j^{(m)} = \frac{1}{\widetilde{Y}_m} D \frac{\partial \widetilde{Y}_m}{\partial x_j}$$

Coordinate Transformation of the Governing Equations

The equation set is then transformed into curvilinear coordinates to allow for numerical solutions to be obtained on non-cartesian grids. The mapping $(x, y, z) \rightarrow (\xi, \eta, \zeta)$ is applied to the equation set to obtain the following set of equations[7]:

$$\frac{\partial U}{\partial t} + \frac{\partial (\hat{E} - \hat{E}_v)}{\partial \xi} + \frac{\partial (\hat{F} - \hat{F}_v)}{\partial \eta} + \frac{\partial (\hat{G} - \hat{G}_v)}{\partial \zeta} = S$$

$$U = \frac{1}{J} \begin{pmatrix} \overline{\rho}_1 \\ \vdots \\ \overline{\rho}_{NS} \\ \overline{\rho}\widetilde{u} \\ \overline{\rho}\widetilde{v} \\ \overline{\rho}\widetilde{w} \\ \overline{\rho}\widetilde{e}_t \end{pmatrix} \qquad S = \begin{pmatrix} \overline{\dot{w}}_1 \\ \vdots \\ \overline{\dot{w}}_{NS} \\ 0 \\ 0 \\ 0 \\ 0 \end{pmatrix}$$

$$\hat{E} = \frac{1}{J} \begin{pmatrix} \overline{\rho}_1 \mathcal{U} \\ \vdots \\ \overline{\rho}_{NS} \mathcal{U} \\ \overline{\rho}\widetilde{u}\mathcal{U} + \xi_x \overline{p} \\ \overline{\rho}\widetilde{v}\mathcal{U} + \xi_y \overline{p} \\ \overline{\rho}\widetilde{w}\mathcal{U} + \xi_z \overline{p} \\ \overline{\rho}\widetilde{h}_t \mathcal{U} \end{pmatrix} \qquad \hat{F} = \frac{1}{J} \begin{pmatrix} \overline{\rho}_1 \mathcal{V} \\ \vdots \\ \overline{\rho}_{NS} \mathcal{V} \\ \overline{\rho}\widetilde{u}\mathcal{V} + \eta_x \overline{p} \\ \overline{\rho}\widetilde{v}\mathcal{V} + \eta_y \overline{p} \\ \overline{\rho}\widetilde{w}\mathcal{V} + \eta_z \overline{p} \\ \overline{\rho}\widetilde{h}_t \mathcal{V} \end{pmatrix} \qquad \hat{G} = \frac{1}{J} \begin{pmatrix} \overline{\rho}_1 \mathcal{W} \\ \vdots \\ \overline{\rho}_{NS} \mathcal{W} \\ \overline{\rho}\widetilde{u}\mathcal{W} + \zeta_x \overline{p} \\ \overline{\rho}\widetilde{v}\mathcal{W} + \zeta_y \overline{p} \\ \overline{\rho}\widetilde{w}\mathcal{W} + \zeta_z \overline{p} \\ \overline{\rho}\widetilde{h}_t \mathcal{W} \end{pmatrix}$$

$$\hat{E}_v = -\frac{1}{J}\begin{pmatrix} \overline{\rho}_1 \mathcal{U}^{(1)} \\ \vdots \\ \overline{\rho}_{NS} \mathcal{U}^{(NS)} \\ \xi_x(\overline{\tau}_{xx} + \mathcal{T}_{xx}) + \xi_y(\overline{\tau}_{xy} + \mathcal{T}_{xy}) + \xi_z(\overline{\tau}_{xz} + \mathcal{T}_{xz}) \\ \xi_x(\overline{\tau}_{yx} + \mathcal{T}_{yx}) + \xi_y(\overline{\tau}_{yy} + \mathcal{T}_{yy}) + \xi_z(\overline{\tau}_{yz} + \mathcal{T}_{yz}) \\ \xi_x(\overline{\tau}_{zx} + \mathcal{T}_{zx}) + \xi_y(\overline{\tau}_{zy} + \mathcal{T}_{zy}) + \xi_z(\overline{\tau}_{zz} + \mathcal{T}_{zz}) \\ \xi_x(\widetilde{u}\,\overline{\tau}_{xx} + \widetilde{v}\,\overline{\tau}_{xy} + \widetilde{w}\,\overline{\tau}_{xz} + \overline{q}_x + \mathcal{Q}_x) \\ + \xi_y(\widetilde{u}\,\overline{\tau}_{yx} + \widetilde{v}\,\overline{\tau}_{yy} + \widetilde{w}\,\overline{\tau}_{yz} + \overline{q}_y + \mathcal{Q}_y) \\ + \xi_z(\widetilde{u}\,\overline{\tau}_{zx} + \widetilde{v}\,\overline{\tau}_{zy} + \widetilde{w}\,\overline{\tau}_{zz} + \overline{q}_z + \mathcal{Q}_z) \end{pmatrix}$$

$$\hat{F}_v = -\frac{1}{J}\begin{pmatrix} \overline{\rho}_1 \mathcal{V}^{(1)} \\ \vdots \\ \overline{\rho}_{NS} \mathcal{V}^{(NS)} \\ \eta_x(\overline{\tau}_{xx} + \mathcal{T}_{xx}) + \eta_y(\overline{\tau}_{xy} + \mathcal{T}_{xy}) + \eta_z(\overline{\tau}_{xz} + \mathcal{T}_{xz}) \\ \eta_x(\overline{\tau}_{yx} + \mathcal{T}_{yx}) + \eta_y(\overline{\tau}_{yy} + \mathcal{T}_{yy}) + \eta_z(\overline{\tau}_{yz} + \mathcal{T}_{yz}) \\ \eta_x(\overline{\tau}_{zx} + \mathcal{T}_{zx}) + \eta_y(\overline{\tau}_{zy} + \mathcal{T}_{zy}) + \eta_z(\overline{\tau}_{zz} + \mathcal{T}_{zz}) \\ \eta_x(\widetilde{u}\,\overline{\tau}_{xx} + \widetilde{v}\,\overline{\tau}_{xy} + \widetilde{w}\,\overline{\tau}_{xz} + \overline{q}_x + \mathcal{Q}_x) \\ + \eta_y(\widetilde{u}\,\overline{\tau}_{yx} + \widetilde{v}\,\overline{\tau}_{yy} + \widetilde{w}\,\overline{\tau}_{yz} + \overline{q}_y + \mathcal{Q}_y) \\ + \eta_z(\widetilde{u}\,\overline{\tau}_{zx} + \widetilde{v}\,\overline{\tau}_{zy} + \widetilde{w}\,\overline{\tau}_{zz} + \overline{q}_z + \mathcal{Q}_z) \end{pmatrix}$$

$$\hat{G}_v = -\frac{1}{J}\begin{pmatrix} \overline{\rho}_1 \mathcal{W}^{(1)} \\ \vdots \\ \overline{\rho}_{NS} \mathcal{W}^{(NS)} \\ \zeta_x(\overline{\tau}_{xx} + \mathcal{T}_{xx}) + \zeta_y(\overline{\tau}_{xy} + \mathcal{T}_{xy}) + \zeta_z(\overline{\tau}_{xz} + \mathcal{T}_{xz}) \\ \zeta_x(\overline{\tau}_{yx} + \mathcal{T}_{yx}) + \zeta_y(\overline{\tau}_{yy} + \mathcal{T}_{yy}) + \zeta_z(\overline{\tau}_{yz} + \mathcal{T}_{yz}) \\ \zeta_x(\overline{\tau}_{zx} + \mathcal{T}_{zx}) + \zeta_y(\overline{\tau}_{zy} + \mathcal{T}_{zy}) + \zeta_z(\overline{\tau}_{zz} + \mathcal{T}_{zz}) \\ \zeta_x(\widetilde{u}\,\overline{\tau}_{xx} + \widetilde{v}\,\overline{\tau}_{xy} + \widetilde{w}\,\overline{\tau}_{xz} + \overline{q}_x + \mathcal{Q}_x) \\ + \zeta_y(\widetilde{u}\,\overline{\tau}_{yx} + \widetilde{v}\,\overline{\tau}_{yy} + \widetilde{w}\,\overline{\tau}_{yz} + \overline{q}_y + \mathcal{Q}_y) \\ + \zeta_z(\widetilde{u}\,\overline{\tau}_{zx} + \widetilde{v}\,\overline{\tau}_{zy} + \widetilde{w}\,\overline{\tau}_{zz} + \overline{q}_z + \mathcal{Q}_z) \end{pmatrix}$$

where the contravariant velocity components are given as:

$$\mathcal{U} \equiv \xi_x \widetilde{u} + \xi_y \widetilde{v} + \xi_z \widetilde{w}$$

$$\mathcal{V} \equiv \eta_x \widetilde{u} + \eta_y \widetilde{v} + \eta_z \widetilde{w}$$

$$\mathcal{W} \equiv \zeta_x \tilde{u} + \zeta_y \tilde{v} + \zeta_z \tilde{w}$$

and the contravariant components of the diffusive velocities are given as:

$$\mathcal{U}^{(m)} \equiv \xi_x V_1^{(m)} + \xi_y V_2^{(m)} + \xi_z V_1^{(m)}$$

$$\mathcal{V}^{(m)} \equiv \eta_x V_1^{(m)} + \eta_y V_2^{(m)} + \eta_z V_3^{(m)}$$

$$\mathcal{W}^{(m)} \equiv \zeta_x V_1^{(m)} + \zeta_y V_2^{(m)} + \zeta_z V_3^{(m)}$$

Chemical Source Terms and the Law of Mass Action

The source vector *S* contains the chemical source terms. These terms are obtained from the law of mass action[27]:

$$\begin{aligned}\overline{\dot{w}}_m &= \sum_{n=1}^{NR} ([\nu''_{mn} - \nu''_{mn}][RR_{f,n} - RR_{b,n}]) \\ &= \sum_{n=1}^{NR} \left([\nu''_{mn} - \nu''_{mn}] \left[k_{f,n} \prod_{j=1}^{NS} (\tilde{c}_j)^{\nu'_j} - k_{b,n} \prod_{j=1}^{NS} (\tilde{c}_j)^{\nu''_j} \right] \right)\end{aligned}$$

The molar density, *c*, and reaction rate constant, *k*, are given as:

$$\tilde{c}_j = \frac{\overline{\rho}_j}{M_j}$$

$$k(T) = AT^b e^{-T_a/T}$$

For the reaction mechanisms considered, exchange reactions of up to four species (two products and two reactants) and dissociation reactions involving a third body are needed. Exchange reactions are expressed as:

$$\mathrm{A} + \mathrm{B} \leftrightarrows \mathrm{C} + \mathrm{D}$$

For such a reaction, the forward and backward reaction rates can be expressed as:

$$RR_f = k_f(T)\tilde{c}_A^{\nu'_A}\tilde{c}_B^{\nu'_B}$$

$$RR_b = k_b(T)\tilde{c}_C^{\nu''_C}\tilde{c}_D^{\nu''_D}$$

The source term for species *m* involved in a third body dissociation reaction can be expressed as:

$$\overline{\dot{w}}_m = \sum_{n=1}^{NR}\left([\nu''_{mn} - \nu''_{mn}]\sum_{i=1}^{NS}[RR_{f,n,i} - RR_{b,n,i}]\right)$$

where the index *i* loops over all of the possible chemical species acting as a third body, and the reaction rates depend not only upon species *m*, and reaction *n*, but also on the third body, species *i*. If the reaction is written as:

$$AB + M \leftrightarrows A + B + M$$

then the reaction rate for reaction *n* is given by:

$$RR_n = \sum_{i=1}^{NS}(RR_{f,n,i} - RR_{f,n,i})$$

where the forward and backward rates corresponding to third body *i* are given as:

$$RR_{f,n,i} = k_{f,n,i}\tilde{c}_{AB}^{\nu'_{AB}}\tilde{c}_{M_i}^{\nu'_{M_i}}$$

$$RR_{b,n,i} = k_{b,n,i}\tilde{c}_A^{\nu''_A}\tilde{c}_B^{\nu''_B}\tilde{c}_{M_i}^{\nu''_{M_i}}$$

To simplify the effect of third bodies on reaction rates, the rate constant corresponding to one of the species can be chosen as a reference value, and then the effect of each of the other species can be stated in terms of a third body efficiency, (*TB*). If $A'_{f,n}$ is chosen as the reference rate coefficient, then the third body efficiency of species *i* can be stated as:

$$(TB)_i = \frac{A_{f,n,i}}{A'_{f,n}}$$

Then, the forward and backward reaction rates corresponding to third body *i* can be stated as:

$$k_{f,n,i} = k'_{f,n}(TB)_i$$

$$k_{b,n,i} = k'_{b,n}(TB)_i$$

Using this notation, the reaction rate for reaction *n* can be expressed as:

$$R_n = [k_{f,n}\tilde{c}_{AB}^{\nu'_{AB}} - k_{b,n}\tilde{c}_{A}^{\nu''_{A}}\tilde{c}_{B}^{\nu''_{B}}]\sum_{i=1}^{NS}(TB)_i\tilde{c}_{M_i}^{\nu'_{M_i}}$$

The 7-species / 7-reaction and 9-species / 18-reaction mechanisms of Jachimowski were used in this work.[12,13,14] The coefficients for the 7-species / 7-reaction mechanism are given in Table 1.

Reaction number	Equation	A	b	T_a
1	H+OH+M⇆H_2O+M	0.221E+23	-2.00	0.00
2	H+H+M⇆H_2+M	0.730E+18	-1.00	0.00
3	H_2+O_2⇆OH+OH	0.170E+14	0.00	24157.0
4	H+O_2⇆OH+O	0.120E+18	-0.91	8310.5
5	OH+H_2⇆H_2O+H	0.220E+14	0.00	2591.8
6	O+H_2⇆OH+H	0.506E+05	2.67	3165.6
7	OH+OH⇆H_2O+O	0.630E+13	0.00	548.6

Table 1: Coefficients for 7-species Jachimowski mechanism

The reactions and rate constants for the 9-species / 18-reaction mechanism are given in Table 2.

Reaction number	Equation	A	b	T_a
1	$H+OH+M \leftrightarrows H_2O+M$	0.221E+23	-2.0	0.0
2	$H+H+M \leftrightarrows H_2+M$	0.653E+18	-1.0	0.0
3	$H+O_2+M \leftrightarrows HO_2+M$	0.320E+19	-1.0	0.0
4	$H_2O_2+M \leftrightarrows 2OH+M$	0.121E+18	0.0	22912.3
5	$H_2+O_2 \leftrightarrows OH+OH$	0.170E+14	0.0	24246.7
6	$H+O_2 \leftrightarrows OH+O$	0.142E+15	0.0	8258.5
7	$OH+H_2 \leftrightarrows H_2O+H$	0.316E+08	1.8	1525.8
8	$O+H_2 \leftrightarrows OH+H$	0.207E+15	0.0	6924.0
9	$OH+OH \leftrightarrows H_2O+O$	0.550E+14	0.0	3525.0
10	$HO_2+OH \leftrightarrows H_2O+O_2$	0.500E+14	0.0	503.6
11	$HO_2+H \leftrightarrows H_2+O_2$	0.253E+14	0.0	352.5
12	$HO_2+H \leftrightarrows OH+OH$	0.199E+15	0.0	906.4
13	$HO_2+O \leftrightarrows OH+O_2$	0.500E+14	0.0	503.6
14	$HO_2+HO_2 \leftrightarrows H_2O_2+O_2$	0.199E+13	0.0	0.0
15	$HO_2+H_2 \leftrightarrows H_2O_2+H$	0.301E+12	0.0	9416.7
16	$H_2O_2+OH \leftrightarrows HO_2+H_2O$	0.102E+14	0.0	956.8
17	$H_2O_2+H \leftrightarrows OH+H_2O$	0.500E+15	0.0	5035.7
18	$H_2O_2+O \leftrightarrows OH+HO_2$	0.199E+14	0.0	2971.0

Table 2: Coefficients for 9-species Jachimowski mechanism

For both mechanisms, the third body efficiencies are 16 for H_2O, 2.5 for H_2, and 1 for all other species. All of the activation temperatures (T_a) are given in Kelvin, and the

Arrhenius rate constants (A) are given in $\mathrm{mol \cdot cm \cdot s \cdot K}$. This is in contrast to the results section where the English customary system of units is used in order to be consistent with the experimental data.

Turbulence-Chemistry Closure Problem

One weakness of the current formulation is that the reaction rates are assumed only to be functions of the mean temperature and molar density. In reality, the reaction rates are also functions of the fluctuating components of temperature and molar density. However, accurately estimating and storing fluctuating quantities for these two variables is very expensive, and computational resources prevented such a formulation for this work. An approximate temperature probability density function (PDF) approach was investigated during the course of this research[5]. The intent of the approximate temperature PDF was to estimate the effect of temperature fluctuations without adding another transport equation. The mean chemical source term was estimated by averaging the chemical reaction rates at one RMS value above and below the mean temperature:

$$\overline{\dot{\omega}}_s = \tfrac{1}{2}\left[\dot{\omega}_s(T+\delta T) + \dot{\omega}_s(T-\delta T)\right]$$

An accurate estimation of the RMS of the temperature fluctuation, δT, can be obtained using the enthalpy variance transport equation:

$$\frac{\partial\left(\overline{\rho}\widetilde{h}''^2\right)}{\partial t} + \frac{\partial\left(\overline{\rho}\widetilde{h}''^2\widetilde{u}_j\right)}{\partial x_j} = \frac{\partial\left[\left(\frac{\mu}{\mathrm{Pr}} + \frac{\mu_T}{\mathrm{Pr}_T}\right)\frac{\partial \widetilde{h}''^2}{\partial x_j}\right]}{\partial x_j} + 2\frac{\mu_T}{\mathrm{Pr}_T}\frac{\partial \widetilde{h}}{\partial x_j}\frac{\partial \widetilde{h}}{\partial x_j} - C_h\frac{\overline{\rho}\widetilde{h}''^2}{\tau}$$

Since memory limits prevented the addition of an additional transport equation, the production and destruction terms in the transport equation were assumed to be equal.

This produced an algebraic expression for $\widetilde{h}''^2$, which is the mean square of the enthalpy variance:

$$\widetilde{h}''^2 = \frac{2\dfrac{\mu_T}{\mathrm{Pr}_T}\dfrac{\partial\widetilde{h}}{\partial x_j}\dfrac{\partial\widetilde{h}}{\partial x_j}}{C_h\dfrac{\overline{\rho}}{\tau}}$$

The RMS of the temperature fluctuation was then calculated using

$$\delta T = \frac{\sqrt{\widetilde{h}''^2}}{C_p}$$

However, this approach has not been validated, and in this work, it was coupled with an incorrect version of one of the reaction mechanisms, so no approximate temperature PDF results are presented in this dissertation.

Closure of the Averaged Equation Set via Menter's Two-Equation Turbulence Model

The averaging performed on the governing equation set resulted in the introduction of three additional terms: the Reynolds shear stress tensor, $\mathcal{T}_{ij}$, the Reynolds heat flux vector, Q_j, and the turbulent molecular diffusion tensor, $\mathcal{Y}_{ij}$. An expression for the Reynolds shear stress tensor can be derived from the Boussinesq approximation, which assumes that it has a form similar to that of the laminar shear stress tensor, $\overline{\tau}_{ij}$. When such an assumption is made, a new term, μ_T, is introduced representing the turbulent viscosity. The resulting expression for the Reynolds shear stress tensor is[7]:

$$\mathcal{T}_{ij} = \mu_T \left(\left(\frac{\partial \widetilde{u}_i}{\partial x_j} + \frac{\partial \widetilde{u}_j}{\partial x_i} \right) - \tfrac{2}{3} \delta_{ij} \frac{\partial \widetilde{u}_k}{\partial x_k} \right)$$

A similar assumption can be made for the Reynolds heat flux vector. The resulting equation follows the form of the laminar heat flux vector. In this case, two new terms, γ_T and $V_{T,j}^{(m)}$ are introduced representing the turbulent thermal conductivity and turbulent (*i.e.* fluctuating) diffusion velocity for species *m*. The equation for the Reynolds heat flux vector is:

$$\mathcal{Q}_j = \gamma_T \frac{\partial \widetilde{T}}{\partial x_j} - \sum_{m=1}^{NS} \overline{\rho} \widetilde{h}_m \widetilde{Y}_m \widetilde{V}_{T,j}^{(m)}$$

The turbulent thermal conductivity and turbulent diffusion velocity are given as:

$$\gamma_T = \frac{\mu_T C_p}{\mathrm{Pr}_T}$$

$$\widetilde{V}_{T,j}^{(m)} = -\frac{1}{\widetilde{Y}_m} D_T \frac{\partial Y_m}{\partial x_j}$$

where D_T is the turbulent diffusivity given by:

$$D_T = \frac{\mu_T}{Sc_T \overline{\rho}}$$

Pr_T is the turbulent Prandtl number, and Sc_T is the turbulent Schmidt number. The turbulent molecular diffusion is obtained using a similar assumption. The resulting expression is:

$$\mathcal{Y}_{m,j} = \overline{\rho Y_m'' u_m''} = -\frac{\mu_T}{Sc_T} \frac{\partial \widetilde{Y}_m}{\partial x_j}$$

In order to close the averaged equation set, the turbulent quantities μ_T, Pr_T, and Sc_T must be calculated. This work assumes a constant turbulent Prandtl number of 0.9

and a constant turbulent Schmidt number of 0.9. (The laminar Prandtl number is 0.72, and the laminar Schmidt number is 0.5). This leaves only the turbulent viscosity (also known as the eddy viscosity) to be modeled.

The kinematic eddy viscosity, $\upsilon_T = \mu_T / \rho$, is more convenient to work with than the turbulent viscosity, so the turbulence model is expressed in terms of υ_T. In Menter's hybrid $k-\omega/k-\varepsilon$ model with shear stress transport (SST)[15], the kinematic eddy viscosity is calculated as:

$$\upsilon_T = \frac{a_1 k}{\max(a_1\omega; F_2\zeta)}$$

where

$$\begin{aligned}\zeta &= \left[\frac{\partial u_i}{\partial x_j}\frac{\partial u_j}{\partial x_i} + \frac{\partial u_i}{\partial x_j}\frac{\partial u_i}{\partial x_j} - \frac{2}{3}\left(\frac{\partial u_i}{\partial x_i}\right)^2\right]^{\frac{1}{2}} \\ &= \left[2\left(\frac{\partial u}{\partial x}\frac{\partial u}{\partial x} + \frac{\partial v}{\partial y}\frac{\partial v}{\partial y} + \frac{\partial w}{\partial z}\frac{\partial w}{\partial z} + \frac{\partial u}{\partial y}\frac{\partial v}{\partial x} + \frac{\partial v}{\partial z}\frac{\partial w}{\partial y} + \frac{\partial w}{\partial x}\frac{\partial u}{\partial z}\right)\right. \\ &\quad + \frac{\partial u}{\partial y}\frac{\partial u}{\partial y} + \frac{\partial v}{\partial z}\frac{\partial v}{\partial z} + \frac{\partial w}{\partial x}\frac{\partial w}{\partial x} + \frac{\partial u}{\partial z}\frac{\partial u}{\partial z} + \frac{\partial v}{\partial x}\frac{\partial v}{\partial x} + \frac{\partial w}{\partial y}\frac{\partial w}{\partial y} \\ &\quad \left. - \frac{2}{3}\left(\frac{\partial u}{\partial x} + \frac{\partial v}{\partial y} + \frac{\partial w}{\partial z}\right)^2\right]^{\frac{1}{2}}\end{aligned}$$

The turbulence kinetic energy, *k*, and the specific dissipation rate, ω, are calculated using the following two transport equations:

$$\frac{\partial(\rho k)}{\partial t} + \frac{\partial(\rho k u_j)}{\partial x_j} = \mu_T\zeta^2 - \beta^*\rho\omega k + \frac{\partial}{\partial x_j}\left([\mu + \sigma_k\mu_T]\frac{\partial k}{\partial x_j}\right)$$

$$\frac{\partial(\rho\omega)}{\partial t} + \frac{\partial(\rho\omega u_j)}{\partial x_j} = \gamma\rho\zeta^2 - \beta\rho\omega^2 + \frac{\partial}{\partial x_j}\left([\mu + \sigma_\omega\mu_T]\frac{\partial\omega}{\partial x_j}\right) + 2\rho(1-F_1)\sigma_2\frac{1}{\omega}\frac{\partial k}{\partial x_j}\frac{\partial\omega}{\partial x_j}$$

The introduction of these two equations raises the number of transport equations from $NS+4$ to $NS+6$. The ω-equation is the hybrid equation which switches from $k-\omega$ to $k-\varepsilon$ using a blending function F_1. F_1 is a continuous function with a value of 1 at the wall (pure $k-\omega$) and 0 in the wake region and free shear layer (pure $k-\varepsilon$). F_1 is calculated as:

$$F_1 = \tanh(\Pi_1^4)$$

where

$$\Pi_1 = \min[\max(\alpha_1, \alpha_3), \alpha_2]$$

$$\alpha_1 = \frac{\sqrt{k}}{0.09\omega y}$$

$$\alpha_2 = \frac{4\rho\sigma_{\omega,2}k}{CD_{k-\omega}y^2}$$

$$\alpha_3 = \frac{500\upsilon}{y^2\omega}$$

$$CD_{k-\omega} = \max\left(2\rho\sigma_{\omega,2}\frac{1}{\omega}\frac{\partial k}{\partial x_j}\frac{\partial \omega}{\partial x_j}, 1\times10^{-20}\right)$$

The parameter F_2 is another blending function which is used to weight the SST term in the expression for υ_t. F_2 is calculated as follows:

$$F_2 = A_{SST}\tanh(\Pi_2^2) + (1 - A_{SST})\tanh(\alpha_3^2)$$

where

$$\Pi_2 = \max(2\alpha_1, \alpha_3)$$

The term A_{SST} varies between 1 and 0 to activate or deactivate the portion of the SST model which can become active away from the wall. In a traditional formulation of the

SST terms, $F_2 = A_{SST} \tanh(\Pi_2^2)$, so the constant A_{SST} scales all of the SST terms. The advantage for only scaling the SST term which can become active away from the wall is that when the traditional formulation was used, better agreement with experimental data was obtained for low values of A_{SST}, whereas increased stability in the near wall region was observed for higher values of A_{SST}. The new formulation allows for the SST terms to remain active in the wall even for low A_{SST}. Setting $A_{SST} = 0$ provided the best agreement with experimental data. Although this particular formulation has not been widely investigated, it might be useful in other high speed problems where the SST terms away from the wall tend to overpredict distance to reattachment after flow separation.

Each of the constants in Menter's model must be scaled between their $k-\omega$ values and their $k-\varepsilon$ values by the blending function F_1. If ϕ_1 is a constant in the $k-\omega$ model, and ϕ_2 is a constant in the $k-\varepsilon$ model, then the blended constant, ϕ, is given by:

$$\phi = F_1\phi_1 + (1-F_1)\phi_2$$

The constants are given as follows:

$$\sigma_{k,1} = 0.5 + 0.35A_{SST} \quad \sigma_{\omega,1} = 0.5 \quad \beta_1 = 0.075 \quad \kappa_1 = 0.41$$

$$\sigma_{k,2} = 1 \quad \sigma_{\omega,2} = 0.856 \quad \beta_2 = 0.0828 \quad \kappa_2 = 0.41$$

$$\beta^* = 0.09 \quad a_1 = 0.31$$

and γ is given by the expression:

$$\gamma = \frac{\beta}{\beta^*} - \sigma_\omega \frac{\kappa^2}{\sqrt{\beta^*}}$$

Because of the high velocities present in the combustor section, the compressibility correction of Wilcox was added to the turbulence model.[16] The compressibility correction scales the destruction term in both the *k* and ω transport equations. The destruction term in the *k* equation, $\beta^* \rho \omega k$, is multiplied by F_k, and the destruction term in the ω equation, $\beta \rho \omega^2$, is multiplied by F_ω.

$$F_k = 1 + (0.5 + F_1) Z_3$$

$$F_\omega = 1 - 1.2(0.5 + F_1) Z_3$$

where

$$Z_3 = Z_2 \frac{\max(Z_1 + 1 \times 10^{-12}, 0)}{|Z_1| + 1 \times 10^{-12}}$$

$$Z_2 = M_T^2 - 0.0625$$

$$Z_1 = \sqrt{M_T^2} - 0.25$$

$$M_T^2 = \frac{2k}{a^2}$$

M_T is the turbulent Mach number and *a* is the local speed of sound.

Upwind Differencing of the Inviscid Fluxes

Because of the hyperbolic nature of the Euler equations, the calculation of the inviscid (*i.e.* Euler) portion of the flux vector must use upwind differences to properly treat the propagation of information through the grid. In this work, the Low Diffusion

Flux Splitting Scheme (LDFSS) of Edwards was used[17]. LDFSS is well suited for reacting flow problems because it is a flux vector splitting scheme, so the calculation of the flux vector requires $O(N)$ operations for N equations, whereas flux difference schemes require $O(N^2)$ operations. Thus, the more species are included, the bigger the cost discrepancy between a flux vector splitting scheme and a flux difference scheme. However, flux difference schemes typically are more diffusive, so they do not capture sharp solution features as well as flux difference schemes. LDFSS attempts to mimic the low diffusion of the flux difference methods while maintaining the cost advantage of the flux vector splitting methods. The splitting for the ξ-direction flux follows, and the other two directional fluxes are split using the same method. The flux vector $\hat{E}$ is split into convective and pressure components, $\hat{E}^{(c)}$ and $\hat{E}^{(p)}$.

$$\hat{E} = \hat{E}^{(c)} + \hat{E}^{(p)} = \frac{|\nabla \xi|}{J}\left(\rho \overline{\mathcal{U}E}^{(c)} + p\overline{E}^{(p)}\right)$$

$\overline{\mathcal{U}}$ is the normalized contravariant component of the velocity in the ξ-direction. It is defined as:

$$\overline{\mathcal{U}} = \frac{1}{|\nabla \xi|}(\xi_x u + \xi_y v + \xi_z w)$$

The vectors $\overline{E}^{(c)}$ and $\overline{E}^{(p)}$ are given as:

$$\overline{E}^{(c)} = \begin{bmatrix} Y_1 \\ \vdots \\ Y_{NS} \\ u \\ v \\ w \\ h_t \\ k \\ w \end{bmatrix} \text{ and } \overline{E}^{(p)} = \begin{bmatrix} 0 \\ \vdots \\ 0 \\ \overline{\xi}_x \\ \overline{\xi}_y \\ \overline{\xi}_z \\ 0 \\ 0 \\ 0 \end{bmatrix}$$

where

$$\overline{\xi}_i = \frac{\xi_i}{|\nabla \xi|}; \quad i = x, y, z$$

$$\hat{E}^{(c)}_{i+\frac{1}{2}} = \frac{|\nabla \xi|}{J}\left(\rho_L a_{\frac{1}{2}} C^+ \widetilde{E}^{(c)}_L + \rho_R a_{\frac{1}{2}} C^- \widetilde{E}^{(c)}_R\right)$$

$$\hat{E}^{(p)}_{i+\frac{1}{2}} = \frac{|\nabla \xi|}{J} \widetilde{E}^{(p)}_{\frac{1}{2}}\left(D^+_L p_L + D^-_R p_R\right)$$

$$a_{\frac{1}{2}} = \frac{a_L + a_R}{2}$$

$$C^+ = \alpha^+_L(1+\beta_L)M_L - \beta_L M^+_L - \beta_L\beta_R \widetilde{M}^+$$

$$C^- = \alpha^-_R(1+\beta_R)M_R - \beta_R M^-_R + \beta_L\beta_R \widetilde{M}^-$$

$$D^+ = \alpha^+_L(1+\beta_L) - \beta_L \overline{P}^+_L$$

$$D^- = \alpha^-_R(1+\beta_R) - \beta_R \overline{P}^-_R$$

$$\alpha^+_L = \tfrac{1}{2}[1 + sign(1, M_L)]$$

$$\alpha^-_R = \tfrac{1}{2}[1 - sign(1, M_R)]$$

$$\beta_L = -\max\left[0, 1 - \text{int}\left(|M_L|\right)\right]$$

$$\beta_R = -\max\left[0, 1 - \text{int}\left(|M_R|\right)\right]$$

$$M_L^+ = \tfrac{1}{4}(M_L + 1)^2$$

$$M_R^- = -\tfrac{1}{4}(M_R - 1)^2$$

$$\overline{P}_L^+ = \tfrac{1}{4}(M_L + 1)^2(2 - M_L)$$

$$\overline{P}_R^- = \tfrac{1}{4}(M_R - 1)^2(2 - M_R)$$

$$\widetilde{M}^+ = \left[1 - \left(\frac{p_L - p_R}{p_L + p_R} + 2\frac{|p_L - p_R|}{p_L}\right)\right]\mathcal{M}_{\frac{1}{2}}$$

$$\widetilde{M}^- = \left[1 + \left(\frac{p_L - p_R}{p_L + p_R} - 2\frac{|p_L - p_R|}{p_L}\right)\right]\mathcal{M}_{\frac{1}{2}}$$

$$\mathcal{M}_{\frac{1}{2}} = \tfrac{1}{4}\left(\sqrt{\tfrac{1}{2}(M_L^2 + M_R^2)} - 1\right)^2 \beta_L \beta_R$$

$$M_i = \frac{1}{a_{\frac{1}{2}}}(\xi_x u + \xi_y v + \xi_z w)_i; \quad i = L, R$$

Building and Solving the Linear System

In order to advance the solution forward in time, a linear system must be built that closely approximates the discretized governing equations. For this work, the following backward Euler linear system was constructed:

$$\begin{aligned}
&\left(\frac{a_{time}}{\Delta t}\frac{\partial \vec{U}}{\partial \vec{W}}\bigg|_{i,j,k}^{n+1,m} + \widetilde{A}_{i,j,k}^{n+1.m} - \frac{\partial \vec{S}}{\partial \vec{W}}\bigg|_{i,j,k}^{n+1.m}\right)\Delta \vec{W}_{i,j,k}^{n+1,m+1} \\
&+ \widetilde{B}_{i,j,k}\Delta \vec{W}_{i,j-1,k}^{n+1,m+1} + \widetilde{C}_{i,j,k}\Delta \vec{W}_{i,j+1,k}^{n+1,m+1} \\
&+ \widetilde{D}_{i,j,k}\Delta \vec{W}_{i,j,k-1}^{n+1,m+1} + \widetilde{E}_{i,j,k}\Delta \vec{W}_{i,j,k+1}^{n+1,m+1} \\
&+ \widetilde{F}_{i,j,k}\Delta \vec{W}_{i-1,j,k}^{n+1,m+1} + \widetilde{G}_{i,j,k}\Delta \vec{W}_{i+1,j,k}^{n+1,m+1} \\
&= -\vec{\mathcal{R}}_{i,j,k}^{n+1,m}
\end{aligned}$$

where $\vec{U}$ is the vector of conserved variables, $\vec{W}$ is the vector of primitive variables, and $\vec{S}$ is the source vector. The coefficient a_{time} is set to 1 for an unsteady calculation and 0 for a steady calculation. $\vec{\mathcal{R}}$ is the unsteady residual vector. For backward-euler at the n+1 time level and m subiteration level, $\vec{\mathcal{R}}$ is given by:

$$\vec{\mathcal{R}}_{i,j,k}^{n+1,m} = \left(\frac{a_{time}}{\Delta t} + \frac{1}{\Delta \tau} \right) \left(\vec{U}_{i,j,k}^{n+1,m} - \vec{U}_{i,j,k}^{n} \right) + \vec{R}(\vec{U}_{i,j,k}^{n+1,m})$$

$\vec{R}$ is the steady residual vector calculated via LDFSS. $\Delta\tau$ is the local time step defined by the global CFL number and local eigenvalues $\left(|\mathcal{U}| + a, |\mathcal{V}| + a, \text{and } |\mathcal{W}| + a\right)$. $\widetilde{A}$ through $\widetilde{G}$ are the flux Jacobians given by Edwards.[17]

For steady-state calculations, once the solution has evolved enough from the initial conditions that it is no longer changing rapidly, the Jacobians no longer need to be calculated at every iteration, so the frequency of Jacobian evaluations can be lowered to increase computational efficiency. This procedure is referred to as Jacobian freezing. Jacobian freezing is far more effective for cold flow calculations, so the Jacobian only needs to be calculated every 5-10 iterations for cold flow simulations. However, for reactive cases, the Jacobian is more likely to change quickly, so it needs to be calculated more often. For ER operation of the engine, where combustion takes place in a diffusion flame, the Jacobians need to be calculated every 3-5 iterations. For IRS operation of the engine, where much of the combustion takes place in a propagating premixed flame, the Jacobians need to be calculated every 1-2 iterations. Premixed flame structures are particularly problematic for Jacobian freezing because the Jacobian of the source term ($\partial\vec{S}/\partial\vec{W}$) can change dramatically when the flame front moves.

The linear system must be factored to allow approximate solutions to be obtained efficiently. For convenience, let

$$\widetilde{H} = \left(\frac{1}{\Delta t} \frac{\partial \vec{U}}{\partial \vec{W}} \bigg|_{i,j,k}^{n+1,m} + \widetilde{A}_{i,j,k}^{n+1,m} - \frac{\partial \vec{S}}{\partial \vec{W}} \bigg|_{i,j,k}^{n+1,m} \right)$$

This system can be solved via global symmetric Gauss-Seidel, but for the present application it is more efficient to use planar symmetric Gauss-Seidel on *i*-constant planes. This is because the tightest grid spacing is usually in the *j*- and *k*-directions, and some of the *i*-directional flow is supersonic. Thus, a matrix partitioning of the Jacobian is first defined as

$$L = \widetilde{F}$$

$$D = \widetilde{H} + \widetilde{B} + \widetilde{C} + \widetilde{D} + \widetilde{E}$$

$$U = \widetilde{G}$$

The linear system can then be approximated by the following system which is more convenient to solve:

$$(D^n + L^n)(D^n)^{-1}(D^n + U^n)\Delta \vec{W}^{n+1} = -\vec{R}_{i,j,k} + \frac{a_{time}}{(\Delta t)_{global}} \left(\vec{U}_{i,j,k}^{\,n} - \vec{U}_{i,j,k}^{\,n-1} \right)$$

This system can be solved via a forward sweep followed by a backward sweep:

$$\Delta \vec{W}_i^{\,n+\frac{1}{2}} = (D_i^n)^{-1} \left(-\vec{R}_{i,j,k} + \frac{a_{time}}{(\Delta t)_{global}} \left(\vec{U}_{i,j,k}^{\,n} - \vec{U}_{i,j,k}^{\,n-1} \right) - L_{i-1}^n \Delta \vec{W}_{i-1}^{\,n+\frac{1}{2}} \right)$$

$$\Delta \vec{W}_i^{\,n+1} = \Delta \vec{W}_i^{\,n+\frac{1}{2}} - (D_i^n)^{-1} U_{i+1}^n \Delta \vec{W}_{i+1}^{\,n+1}$$

For increased computational efficiency, the block pentadiagonal matrix D_i is approximately inverted using a block incomplete LU decomposition method.

Past Validation of Flow Solver

The numerical solutions were produced using a validated Navier-Stokes flow solver for unsteady, reactive flow calculations on massively parallel architectures.[18,19,20] The solver has been validated for steady-state shock / hydrogen flame configurations as well as other cases.[18] The code has been validated for both 2-D and 3-D dynamic simulations of time-dependent hydrogen fuel injection in a scramjet inlet-combustor configuration.[19,20]

Numerical Grid

For the computational grid, half-plane symmetry with respect to the y-axis is assumed. The physical domain for the $y > 0$ half of the engine is discretized using a mesh of 3.3 million points divided into 98 load-balanced subdomains. Resolution of the fuel injectors is enhanced by tighter mesh spacing in the diffuser section. The diffuser section is connected to its upstream and downstream sections via a patched-grid interface. A picture of the grid is shown in Figure 4. For one of the IRS cases, a coarse grid was used for each reaction mechanism to evaluate the effect of grid resolution on the results. The coarse grid was generated by removing every other point from the fine grid in the axial and radial directions.

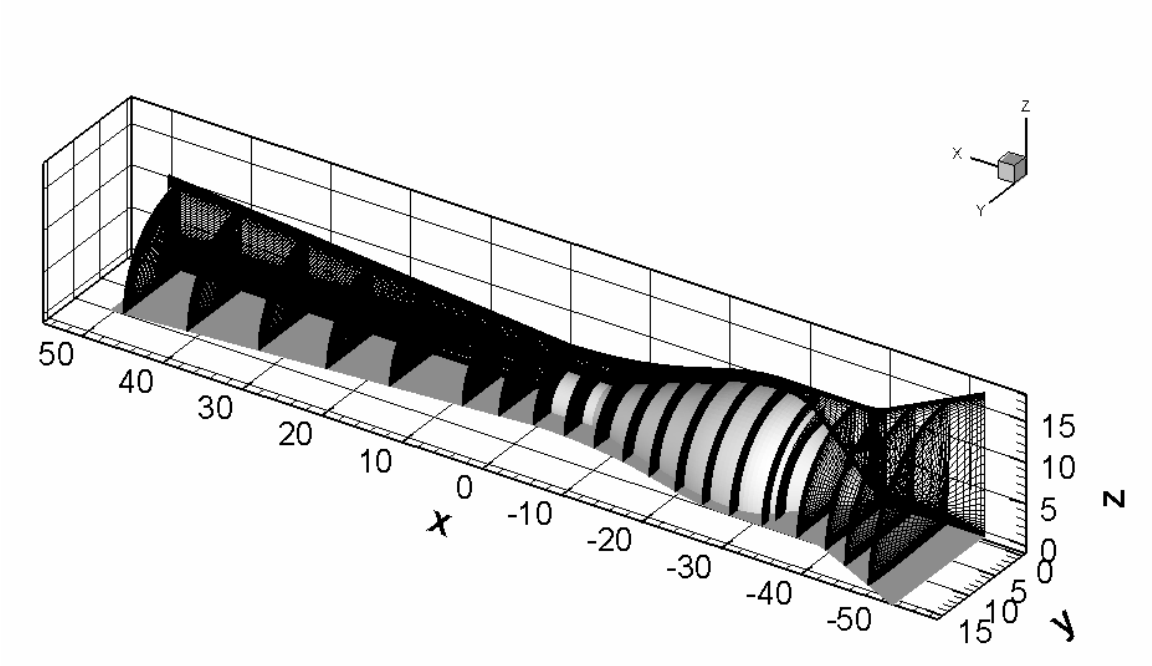

Figure 4: Computational Mesh Used for ER and IRS Simulations

Boundary Conditions and Convergence Monitoring

Two different inlet boundary conditions were tried for the cold flow and ER solutions: a constant mass flow boundary condition and a constant total pressure boundary condition. The constant mass flow boundary condition, which more closely represents the experimental setup, fixes $\dot{m}_i$, $T_{0,i}$, $Y_{s,i}$, and velocity direction (*i.e.* $\vec{v}/\|\vec{v}\|$) while extrapolating p from the interior. The constant total pressure boundary condition, which more closely represents future flight conditions, fixes $p_{0,i}$ $T_{0,i}$, $Y_{s,i}$, and $\vec{v}/\|\vec{v}\|$ while extrapolating u from the interior. Both of these boundary conditions yielded identical results for the cold flow and ER solutions. However, for IRS solutions, the constant mass flow boundary condition could not be used because of the presence of the

thermal throat. This is because the location of the thermal throat dictates the mass flow rate through the combustor. For IRS cases, the constant total pressure boundary condition and a characteristic boundary condition were both used, and they both produced identical results. The characteristic boundary condition differed from the constant total pressure boundary condition in that the Riemann invariant $w_3 = u - 2a/\gamma$ was extrapolated rather than u.

The exit boundary condition was a mixed subsonic/supersonic boundary condition where all variables were extrapolated wherever $M > 0$. Where $M < 0$, p_e was fixed while u, v, w, T, and Y_s were extrapolated from the interior. At the solid walls, the adiabatic, no-slip boundary condition was applied: $u = v = w = \frac{\partial T}{\partial n} = \frac{\partial \rho_s}{\partial n} = 0$.

The rocket exit was modeled as a supersonic inflow plane to the combustor (*i.e.* Dirichlet boundary condition). The rocket exit conditions for each mass ratio and chamber pressure were calculated using the NASA-Glenn Chemical Equilibrium Program CEA.[21] The rocket was assumed to operate at 95% combustion efficiency. This was modeled in the CEA code by assuming that 5% of the hydrogen injected into the rocket plenum was inert, while the other 95% was fully reactive.

Because of the tighter mesh spacing in the blocks surrounding the fuel injectors, special interblock transfer boundary conditions were needed to pass information across these interfaces. Two such boundary conditions were used, a conservative communication algorithm and a non-conservative communication algorithm. Neither appeared to have any significant advantage over the other for this flow. The conservative communication algorithm was a simplified version of one developed as part of prior work.[22,23,24] The conservative communication algorithm in its general form allows

moving discontinuities which vary in both of the coordinate directions in the interface surface. However, for this case, since the blocks containing the injectors were refined in only the axial and circumferential direction, the communication algorithm only needed to account for the circumferential direction. (Since the axial direction was normal to the block interface, the metric terms automatically take care of the jump in grid spacing in that direction.) Also, since the injector blocks had exactly twice as many cells in the circumferential direction as the non-injector blocks, the communication algorithm was further simplified. Thus, two boundary conditions, a coarse-to-fine transfer and a fine-to-coarse transfer, allow the blocks to communicate. For this description, *i* is in the axial direction, *j* is in the radial direction, and *k* is in the circumferential direction. The coarse-to-fine transfer is given by:

$$U^{(f)}_{j,2k} = U^{(f)}_{j,2k-1} = U^{(c)}_{j,k}$$

where *U* is the vector of conserved variables. The fine-to-coarse transfer is given by:

$$U^{(c)}_{j,k} = \frac{A^{(f)}_{j,2k-1} U^{(f)}_{j,2k-1} + A^{(f)}_{j,2k} U^{(f)}_{j,2k}}{A^{(f)}_{j,2k-1} + A^{(f)}_{j,2k}}$$

where *A* is the area of the side of the cell on the interface. Note that $A^{(c)}_{j,k} = A^{(f)}_{j,2k-1} + A^{(f)}_{j,2k}$. Although these transfers are conservative, equally simple non-conservative transfers can be used to achieve higher spatial accuracy. The non-conservative coarse-to-fine transfer is given by:

$$U^{(f)}_{j,2k-1} = \tfrac{1}{4}(U^{(c)}_{j,k-1} + 3U^{(c)}_{j,k})$$

$$U^{(f)}_{j,2k} = \tfrac{1}{4}(3U^{(c)}_{j,k} + U^{(c)}_{j,k-1})$$

while the non-conservative fine-to-coarse transfer is given by:

$$U_{j,k}^{(c)} = \tfrac{1}{8}(U_{j,2k-2}^{(f)} + 3U_{j,2k-1}^{(f)} + 3U_{j,2k}^{(f)} + U_{j,2k+1}^{(f)})$$

Since the circumferential resolution was high, and the local Mach number at the interface was low (less than or equal to 0.38), no significant difference was observed for solutions using the two different communication algorithms. The order of accuracy of the transfer might have made a difference if the circumferential resolution on the coarser interface grid was lower, and the conservation error might have been significant if the Mach number local to the interface had been higher.

Convergence of the numerical solutions was monitored by calculating the mass flow rate through five planes in the engine. When the relative difference between the maximum and minimum of these five values was less than 0.1%, calculations were stopped. In addition to mass flow rate monitoring, the pressure profiles at the final iteration were compared with previous pressure profiles to ensure that the solution was no longer changing.

Test Cases

Two cold flow test cases, two ER test cases, five steady IRS test cases, and two unsteady IRS cases are presented in this work. The cold flow and ER cases both correspond to tests completed in the direct-connect facility at NASA Glenn Research Center. The conditions for each of the steady cases are given in the following table.

Test Case	$p_{t,i}$	p_c	MR	ϕ	p_e
ESP 39	13.1	N/A	N/A	0.0	3.1

Test Case	$p_{t,i}$	p_c	MR	ϕ	p_e
ESP 41	13.1	N/A	N/A	0.0	8.2
ER 8081	6.7	750	4	0.0	2.2
ER 8687	13.4	750	4	0.0	2.6
IRS NCSU 1500	32.0	1500	6	1.0	2.2
IRS NCSU 1000	32.0	1000	6	1.0	2.2
IRS NCSU 750	32.0	750	6	1.0	2.2
IRS NCSU 500	32.0	500	6	1.0	2.2
IRS NCSU 400	32.0	400	6	1.0	2.2

Table 3: Conditions for steady-state test cases

The symbols $p_{t,i}$, p_c, MR, ϕ, and p_e stand for the inlet total pressure, rocket chamber pressure, rocket mass ratio, equivalence ratio in the fuel-air stream, and rig exit pressure, respectively. All pressures are given in psia. The mass ratio is defined as the ratio of oxygen to hydrogen by mass (*e.g.* stoichiometric conditions would correspond to $MR = 8$).

The steady IRS cases constitute a five stage throttle down process for the rocket. This purpose of this sequence of runs is to arrive at a chamber pressure of 400 psia while maintaining the thermal throat. The engines on the vehicle are expected to thermally choke while the rocket is running at a high chamber pressure (between 2000 and 1500 psia). Initializing the rocket to a chamber pressure at less than 1500 psia does not allow a thermal throat to form, but a solution with an existing thermal throat can be throttled

down gradually so that the thermal throat is maintained. In a typical thermally choked ramjet, the existence and location of a thermal throat is dependent upon the heat release and geometry of the combustor section. However, for the GTX combustor, the relevant geometry for thermal choking is the effective geometry of the secondary flow (*i.e.* airbreathing part). Because the primary flow (*i.e.* the rocket plume) displaces the secondary flow in the combustor, the effective geometry of the secondary flow is dependent upon the rocket conditions. Thus, a thermally choked solution was generated at a chamber pressure of 1500 psia, and then throttled down in a set of successive steady-state solutions until the chamber pressure of 400 psia was reached. The chamber pressure of 400 psia corresponds to flight conditions at Mach 2.5, just prior to mode transition (*i.e.* rocket cutoff).

Using case IRS NCSU 400 as a starting point, two unsteady mode transition simulations were performed. Each of these unsteady cases required the addition of another 9 grid blocks for the interior of the rocket. (For the steady cases, the rocket exit was incorporated as an inlet plane to the combustor section.) The inlet boundary conditions for the rocket were initialized to the plenum conditions for case IRS NCSU 400. Because the rocket exit flow was supersonic for all of the steady solutions, it was modeled as a supersonic inlet flow plane (*i.e.* Dirichlet) boundary condition. However, in the unsteady calculations, subsonic flow was present in the rocket, so it was necessary to couple the simulation of the rocket with the rest of the engine.

The first mode transition study involved linearly ramping the rocket mass flow rate down from 1.307 lbm/s to 0 over a period of 0.5 ms while holding the plenum inflow

temperature constant at 7554 °R.[†] The second mode transition study consisted of a nitrogen purge. The rocket composition was linearly changed from $MR = 6$ to pure nitrogen, and the inflow temperature was linearly changed from 7554 °R to 872.7 °R over a period of 0.5 ms while the mass flow was held constant at 1.307 lbm/s. These conditions were held steady for another 6.25 ms, and then the nitrogen mass flow rate was linearly ramped down to zero over 0.5 ms. The nitrogen purge is similar to the procedure that will be performed in the experimental tests for safety purposes, whereas the cutoff without the purge more closely matches the conditions of flight. The times, however, are much shorter than the procedures for either flight or ground testing. This is because the real time will be approximately 0.5 s, rather than 0.5 ms, so temporally correct unsteady simulations would have been prohibitively expensive.

Results

Results for Cold Flow Cases

The cold flow results presented correspond to tests ESP 39 and ESP 41. Calculations for these cases were presented in a previous paper, but a geometry error led to significant discrepancies between the CFD predictions and the experimental data.[4]

[†] Note that this value for the static temperature is larger than the true peak static temperature within the plenum. The reason for this is that the plenum inflow plane in the CFD calculation is composed only of H_2O and H_2 based upon the assumption that all of the combustion has take place upstream of the inlet plane. In the real rocket, H_2 and O_2 are injected into the plenum. The mixing, burning, and acceleration of the flow are simultaneous, so the true peak static temperature within the plenum is smaller than the inlet static temperature boundary condition set for the CFD calculations.

The geometry error was corrected, and then the calculations were repeated for the two cases.

Figure 5 and Figure 6 compare the pressure predicted by the CFD calculations to the experimental results for case ESP 39 along the centerline and cowl 0° line, respectively. The term "centerline" refers to the intersection of the symmetry plane with the flat plate in the combustor section and the intersection of the symmetry plane with the centerbody in the inlet and isolator sections. The term "cowl 0° line" refers to the intersection of the symmetry plane with the cowl. For this case, there is good agreement between the predicted and measured cowl pressures along the entire length of the engine. However, there is a discrepancy in the centerline pressures between $x = 0$ and $x = 20$ inches. This is the region just aft of the rocket exit. Since the rocket was covered with a plate for all of the cold flow cases, it was modeled as a solid surface in the CFD calculations. The CFD calculations did not capture the pressure waves in this region as well as was desired; however, this region was filled by the rocket plume for hot flow tests, so this particular problem was unique to this case.

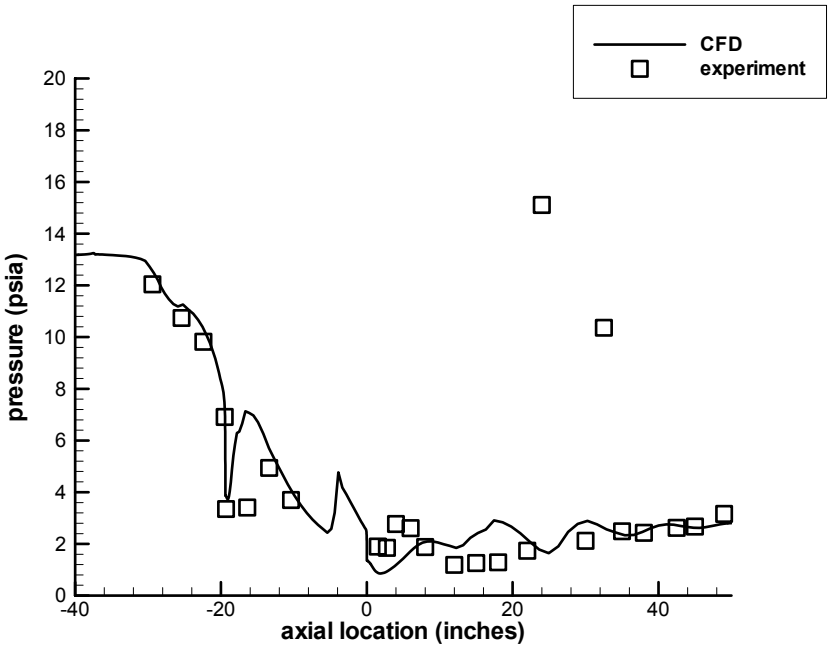

Figure 5: Centerline pressure comparison for ESP 39

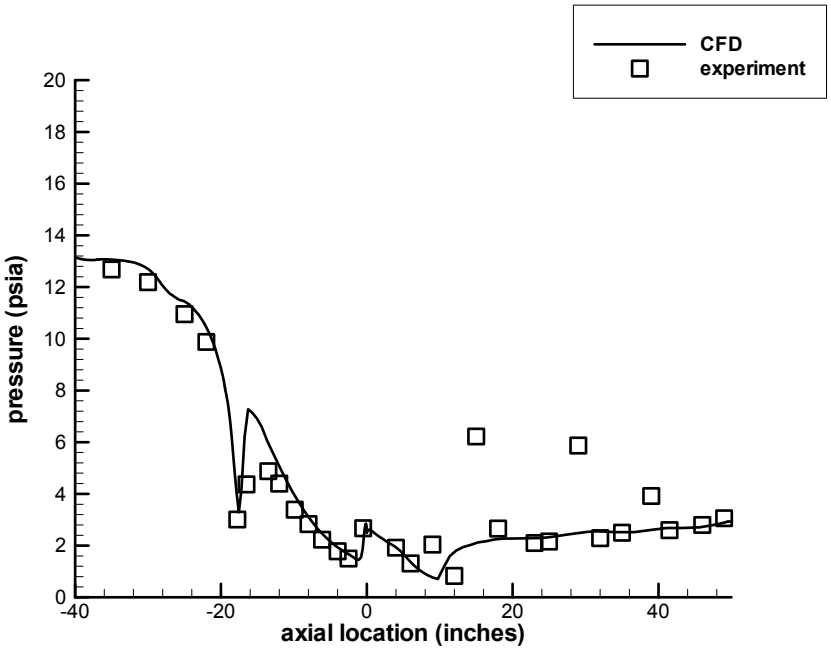

Figure 6: Cowl pressure comparison for ESP 39

Figure 7 and Figure 8 compare the pressure from the CFD prediction to the experimental data for case ESP 41 along the centerline and cowl 0˚ line, respectively. For this case, there is good agreement between the predicted and measured pressures along both surfaces along the entire length of the engine. Since this case had a higher back pressure than case ESP 39, the flow at the exit was subsonic, and a large region of flow separation was present along the flat plate behind the rocket exit. Because the flow was separated at the combustor exit, an additional 50 inches of the facility were added to the grid so that a well-posed outflow boundary condition could be enforced.

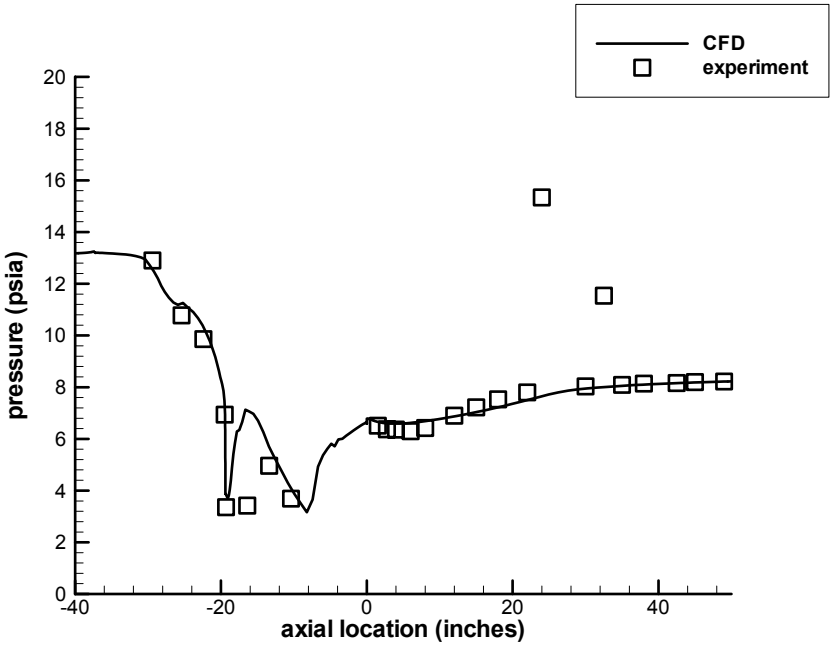

Figure 7: Centerline pressure comparison for ESP 41

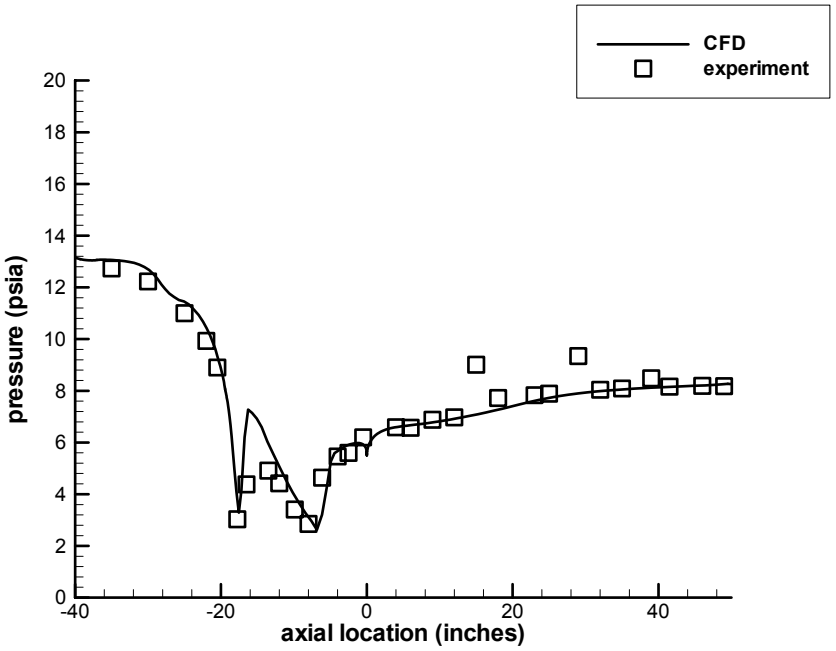

Figure 8: Cowl pressure comparison for ESP 41

Results for ER Cases

The ER results presented correspond to tests ER 8081 and ER 8687, two of the ER experiments completed to date. Figure 9 shows the centerline pressure predicted by two CFD calculations compared to the experimental data for ER 8081. Figure 10 shows the cowl pressures for the same case. One of the CFD calculations was performed with the compressibility correction, while the other was performed without the compressibility correction. Along the centerline and along the portion of the cowl upstream of the flame influence, the solution without the compressibility correction agrees better with the experimental data. However, along the portion of the cowl downstream of the flame influence, the solution with the compressibility correction agrees better with the experimental data. This is because the solution without the compressibility correction

overpredicts the mixing. Since diffusion flames are mixing driven, the overprediction in mixing leads to higher heat release and thus higher wall pressures. Both of these solutions have an additional constraint of $u \geq 0$ imposed at the exit of the combustor section. This is because there is axial separation along the cowl, and the outflow boundary condition is ill-posed wherever $u < 0$. The constraint was added in lieu of a domain extension because of the extreme cost of extending the domain for a reacting solution. Also, the axial separation region for these cases was limited to the last few inches of the cowl surface, just before the diverging combustor section is connected to the straight exhaust duct. Figure 11 and Figure 12 compare the 7- and 9-species reaction mechanisms along the centerline and cowl, respectively. Both of these solutions and those that follow use the Wilcox compressibility correction.[16] The 9-species mechanism provides marginally better agreement with the experimental data throughout the engine. The lower wall pressures for the 7-species case show that it is slightly underpredicting the heat release.

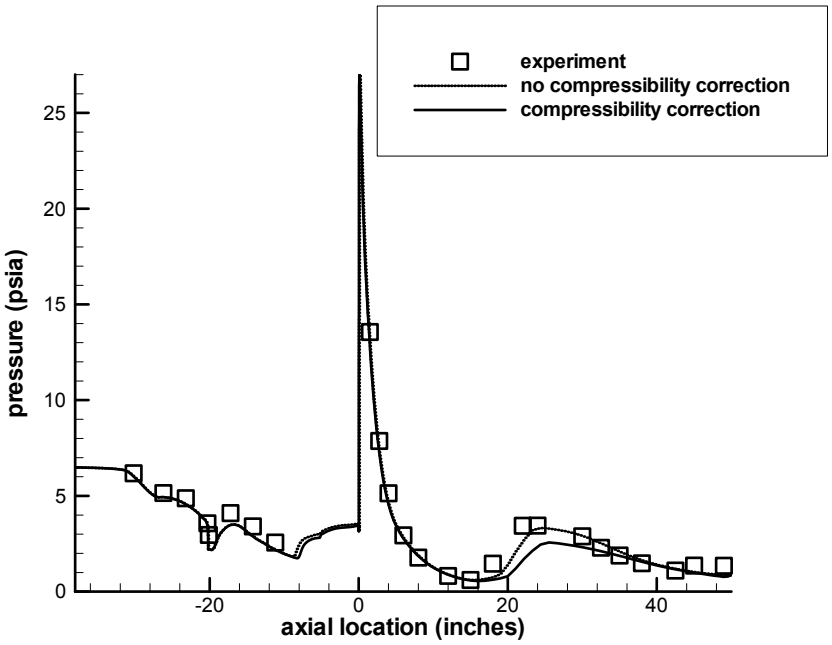

Figure 9: ER 8081 centerline pressure with and without compressibility correction

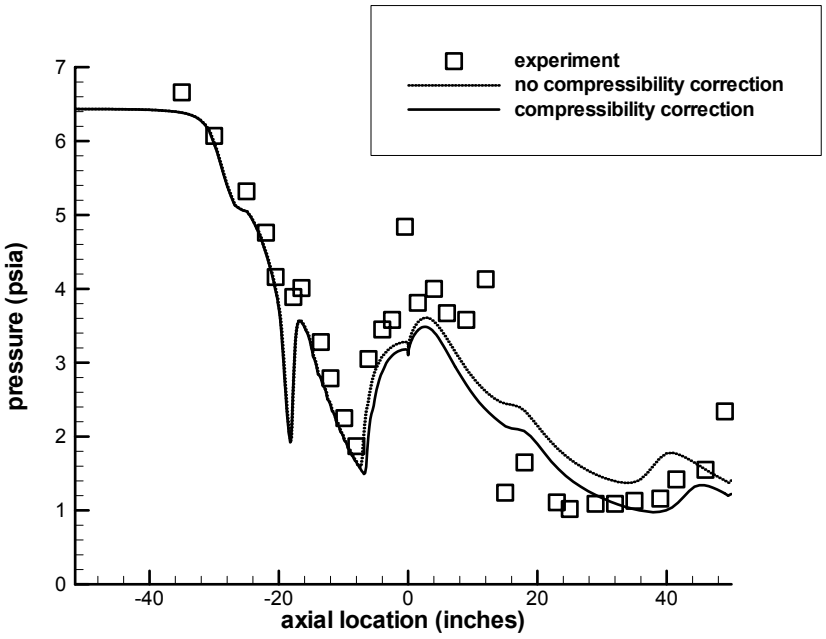

Figure 10: ER 8081 cowl pressure with and without compressibility correction

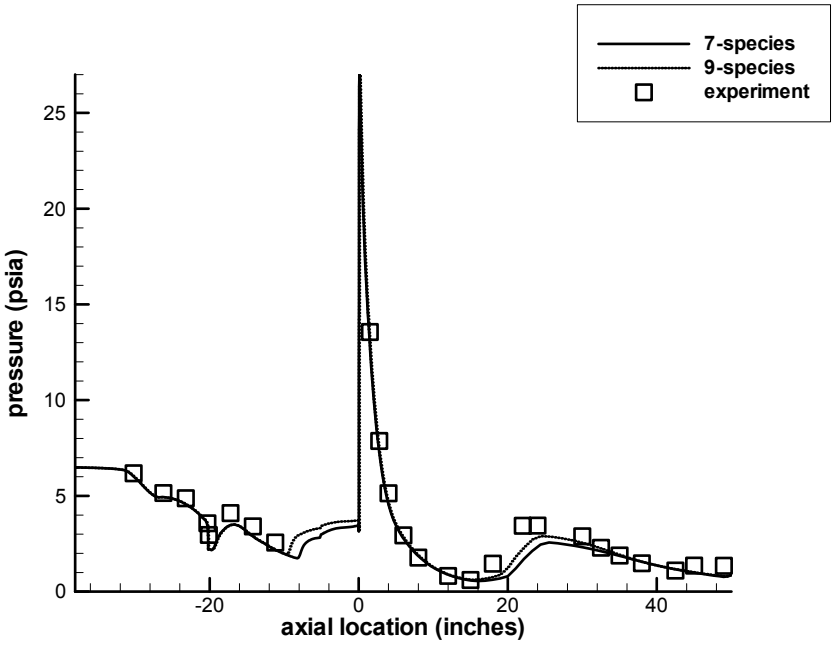

Figure 11: ER 8081 centerline pressure with 7- and 9-species models

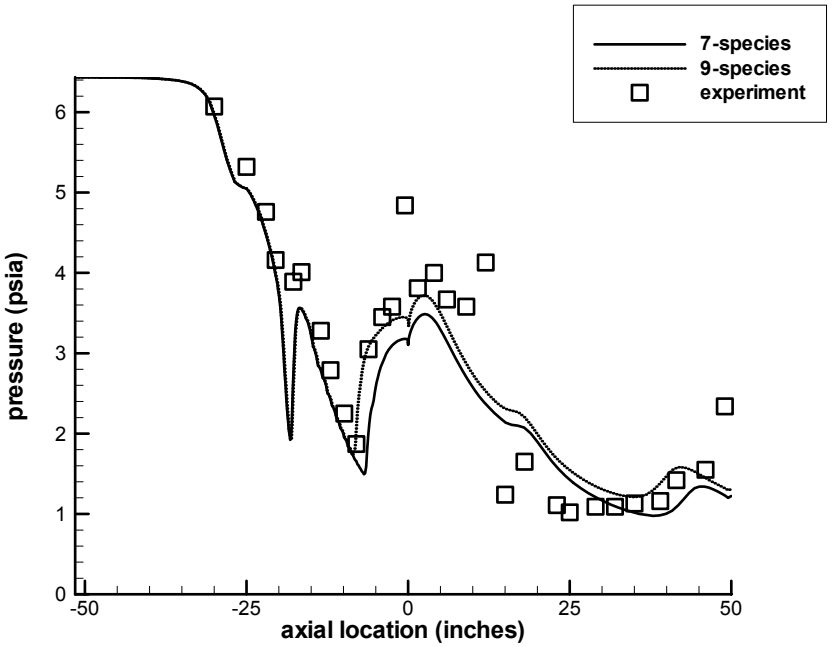

Figure 12: ER 8081 cowl pressure from 7- and 9-species mechanisms

Figure 13 shows the centerline pressure predicted by the CFD calculations compared to the experimental data for ER 8687. Figure 14 shows the cowl pressure for the same case. As expected for ER operation in a relatively short combustor (50 inches), the heat release is not enough to form a thermal throat. The results are in good agreement with the experiment except for discrepancies along the cowl in the latter half of the combustor section where the influence of the combustion is most evident. The strong shock wave aft of the rocket exit is caused by the impingement of the rocket plume upon the flat plate. A separation region follows this shock. The shock, separation, and reattachment are all predicted by the CFD solution; however, the shock-induced separation is much larger in the experimental data. It was again necessary to enforce $u \geq 0$ in order to keep the exit boundary condition well-posed. As was the case for ER 8081, the 9-species mechanism gives higher heat release and marginally better agreement with the experimental data than the 7-species mechanism.

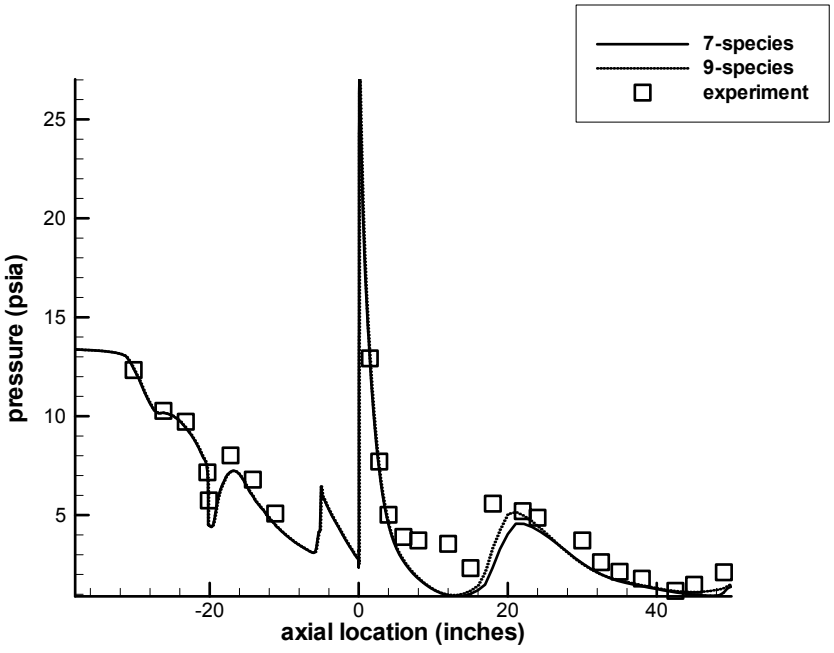

Figure 13: Centerline pressures for case ER 8687

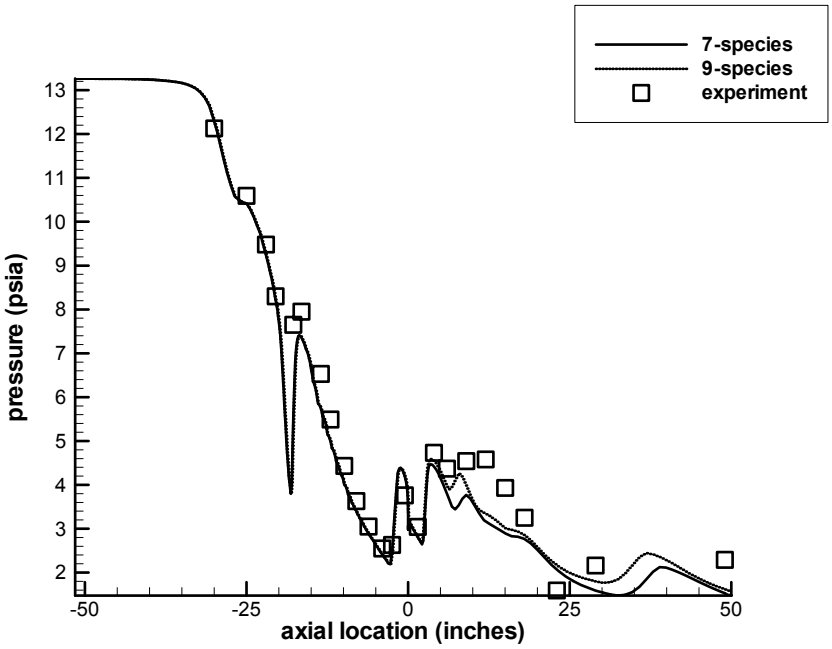

Figure 14: Cowl pressures for case ER 8687

Figure 15 shows the temperature contours for case ER 8687. Temperatures of around 4500˚R are found in the flame front, while temperatures of around 5800˚R are found where the rocket plume impinges on the flat plate. The rocket exhaust enters the combustion chamber at approximately 2630˚R, and the additional fuel in the exhaust ignites almost immediately, forming a diffusion flame which is anchored at the rocket base plate and stretches the full length of the combustor. The flame front can be better seen in the contours of Y_{OH} in Figure 16. Since significant amounts of OH are still present at the combustor exit, the combustion is incomplete.

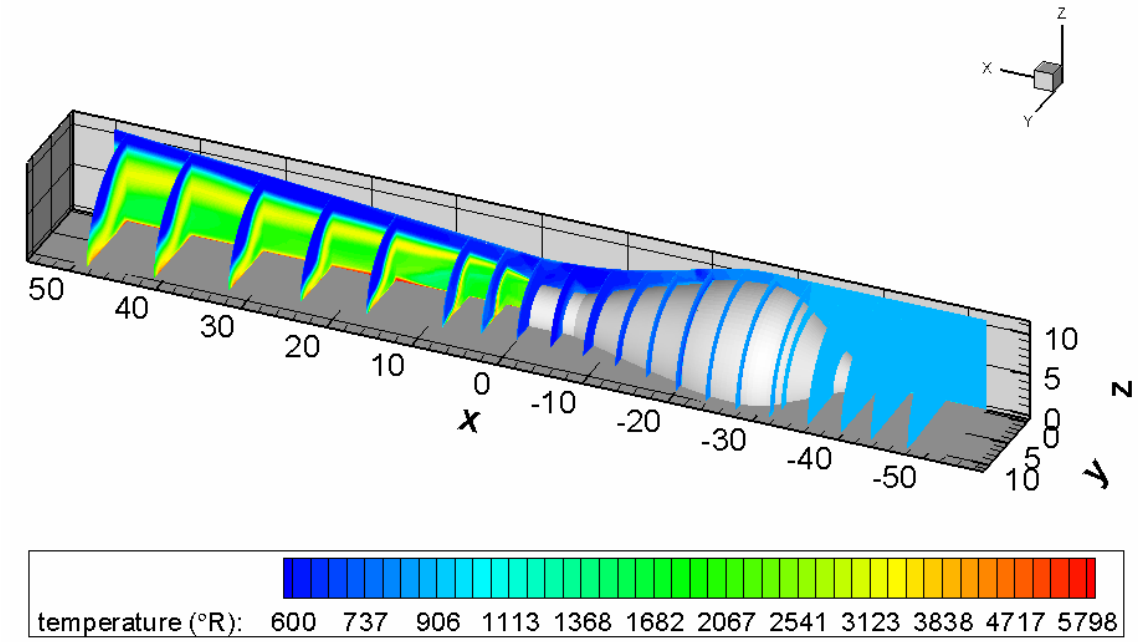

Figure 15: Temperature contours for case ER 8687

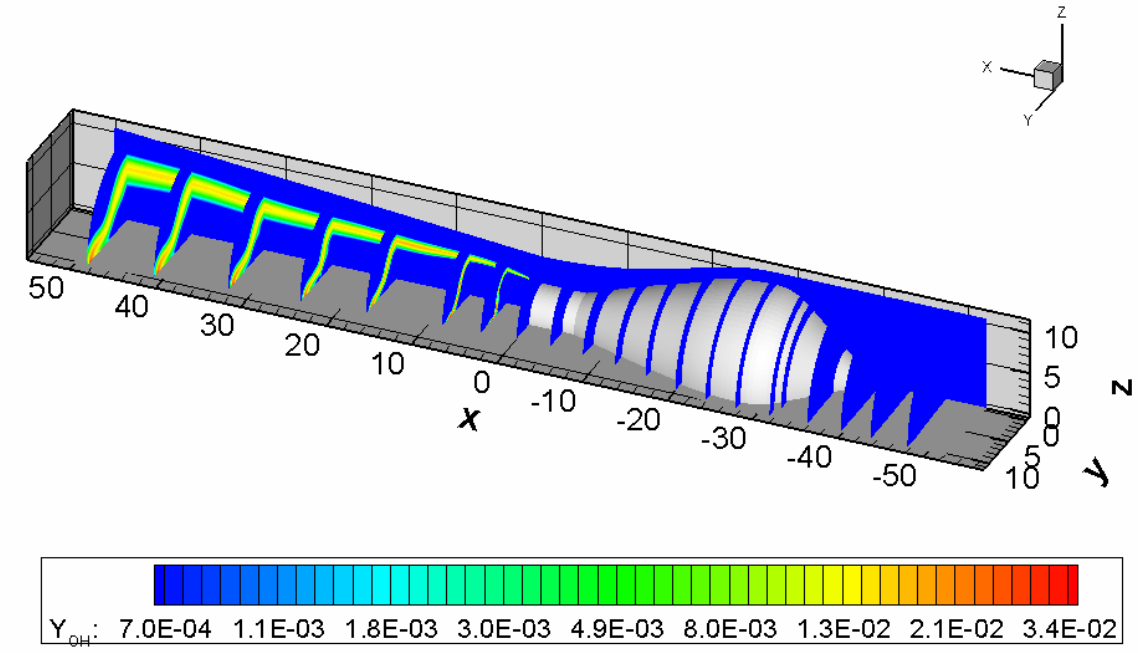

Figure 16: OH mass fraction contours for case ER 8687

Reaction Mechanism Comparison for IRS

Solutions for case IRS NCSU 750 were produced using both the 7- and 9-species reaction mechanisms. All of the fuel was injected through the upstream bank for this comparison. These solutions with $p_c = 750$ psia were produced using the $p_c = 1000$ psia solution for an initial condition, which was produced using the $p_c = 1500$ psia case for an initial condition. The reason for this is that the calculation could not establish a thermal throat unless $p_c / p_{t,i}$ is high enough. The highest chamber pressure that can be replicated with the experimental apparatus is 750 psia, so that case was chosen for the reaction mechanism comparison. This will allow CFD results to be compared with experimental IRS data once it becomes available.

Figure 17 and Figure 18 show the centerline and cowl pressures, respectively, for both reaction mechanisms. The huge discrepancies in the pressure profiles are present because the 7-species solution is thermally choked, whereas the 9-species solution is not. Although the 9-species reaction mechanism resulted in slightly higher heat release for the ER test cases, it shows a much higher ignition delay than the 7-species mechanism. This delay is insignificant for the mixing driven, diffusion flame present in ER operation (which is stabilized by the hot rocket exhaust), but it is very significant for the partially premixed flame structure present in IRS operation. The slower ignition and chain-branching kinetics predicted by the 9-species solution result in poor flame propagation and incomplete combustion in the secondary stream. Since less of the fuel-air mixture burns in the 9-species solution, the heat release is not enough to thermally choke the flow. Figure 19 shows the temperature contours for both the 7- and 9-species solutions. In addition to the difference in flame structure, the difference in isolator flow features can

be seen in this plot. Since there is no thermal throat in the 9-species solution, the flow physically chokes just aft of the injectors, and a series of oblique shocks is induced by the sharp corner where the centerbody and rocket cowl meet. These features are not present in the 7-species solution because the flame and thermal throat structure provide a high enough back pressure to keep the isolator flow subsonic. Figure 20 shows the detail of the flame structures using mass fraction contours for monatomic hydrogen. For the 9-species solution, there is a diffusion flame oriented along the mixing layer between the primary and secondary streams, but there is no premixed flame propagating out toward the cowl. For the 7-species solution, the premixed flame propagation is fast enough to result in the formation of a lifted, triple-flame structure in the partially-premixed secondary stream. The triple point of the lifted flame is in the vicinity of the stoichiometric line. Two premixed branches, one rich and one lean, propagate from this point. Behind the lean premixed branch, there is a surplus of oxidizer, and there is a surplus of fuel behind the lean branch. A diffusion-flame branch forms where these two regions meet.

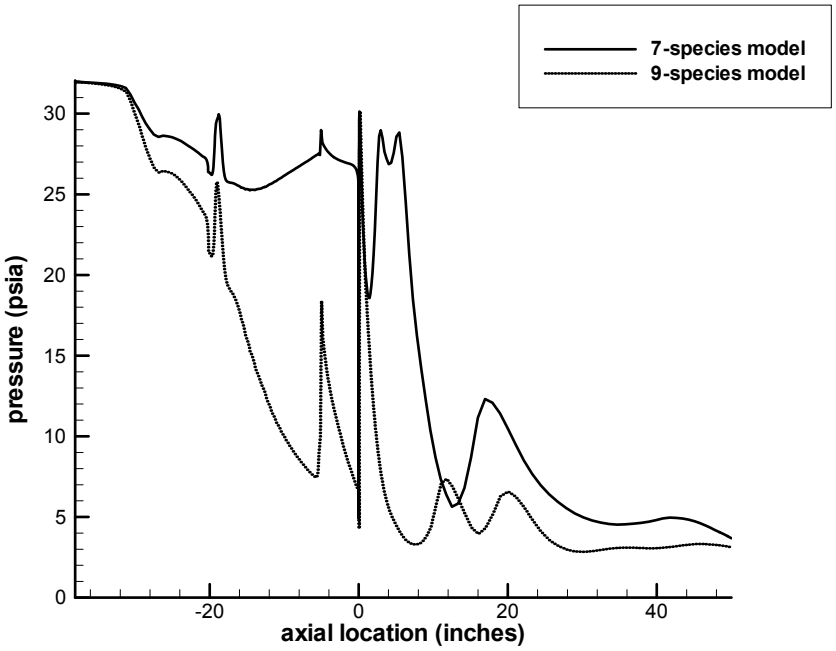

Figure 17: Centerline pressure comparison for case IRS NCSU 750

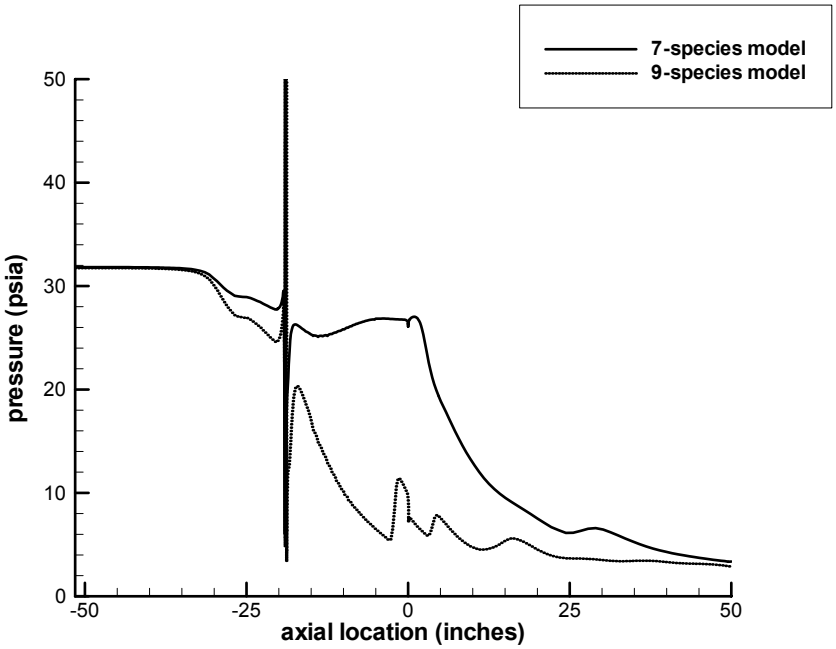

Figure 18: Cowl pressure comparison for case IRS NCSU 750

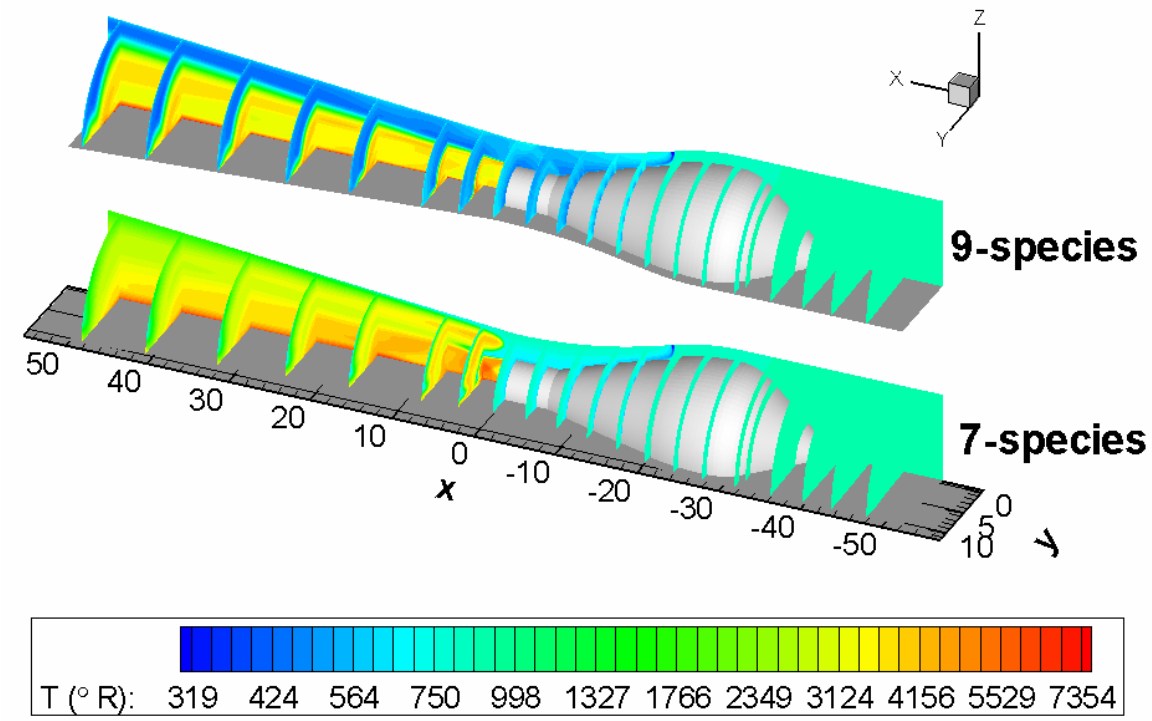

Figure 19: Temperature contours for case IRS NCSU 750

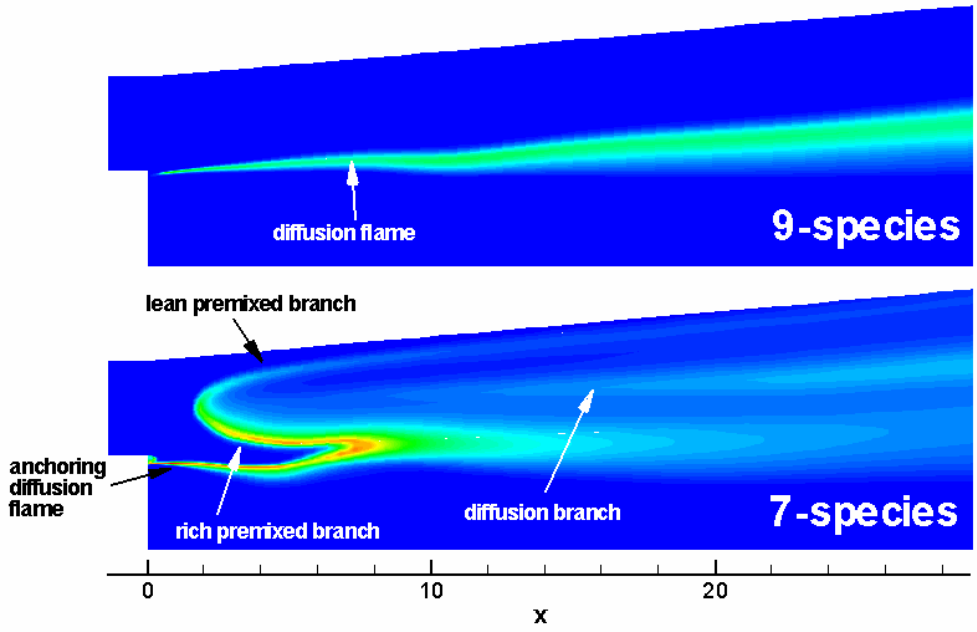

Figure 20: Comparison of H mass fraction contours

Grid Resolution Study for IRS

Obtaining a solution on a coarsened mesh provides an indication for how far the fine grid is from adequately resolving the flow features. The $p_c = 750\,\text{psi}$ case was simulated on both the fine and coarse grids for both reaction mechanisms. Figure 21 and Figure 22 show the centerline and cowl pressure profiles, respectively. For the 7-species mechanism, the centerline pressure distributions show a difference in the amount of resolution in the shock / expansion system behind the rocket exit. These features are better resolved on the fine grid. The cowl pressure profile shows a large pressure increase followed by a large pressure decrease at around $x = -19$ inches. This is because the cowl 0˚ line passes through one of the fuel injectors at this point. Both the centerline and cowl pressure distributions show that the coarse grid solution predicts a higher isolator pressure. This is because the thermal throat is farther forward in the coarse grid solution. The pressure drop corresponding to the expansion in the thermal throat region can be seen in the cowl pressure distribution. For the 9-species model, the discrepancies in resolution in the region of the rocket plume are similar to those of the 7-species case. Since decreasing the grid resolution to that of the coarse grid decreases the resolution of flow features, it is reasonable to assume that grid convergence has not been achieved and that further grid refinement would increase the resolution of the existing flow features. However, current computational resources will not allow for a larger grid.

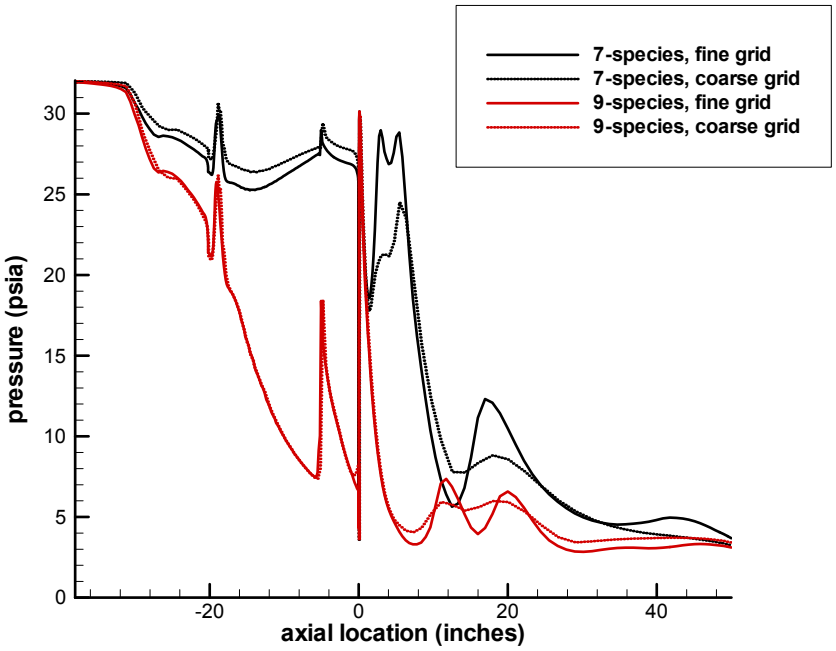

Figure 21: Centerline pressure profiles for grid refinement study

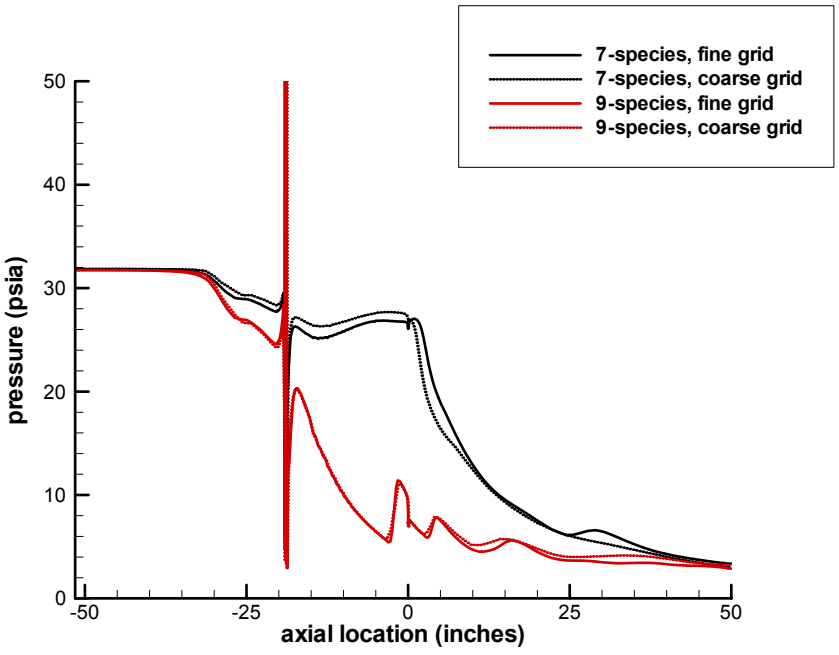

Figure 22: Cowl pressure profiles for grid refinement study

It is clear that the uncertainties evidenced in Figure 17 through Figure 20 are not a result of insufficient grid refinement, but, rather, a consequence of the chemical kinetics models. Such problems in using more complex reaction models are relatively common in high-speed propulsion applications. For example, in simulations of non-vitiated, supersonic, hydrogen-air combustion downstream of a ramped injector, Goyne, *et. al.* found the ignition kinetics of the 7-species model to be too slow for proper flame stabilization, so they reverted to a 4-species / 1-step model.[25,26] More complex chemistry models are more sensitive to Schmidt number effects, and advanced models that account for the effects of turbulent fluctuations on reaction rates have not yet been extensively validated for combustion at high Mach numbers. Preliminary results using a simplified temperature PDF approach (see the section entitled "Turbulence-Chemistry Closure Problem" on page 18) did indicate that accounting for the effects of temperature fluctuations on reaction rates could reduce the ignition delay for the 9-species model,[5] but in the absence of experimental data for IRS operation, it is impossible to determine which approach (if any) best represents the physics. The remaining predictive calculations therefore adopt the 7-step model to assess the effects of fuel injection modulations during thermal-throat ramjet operation.

Fuel Injection Study

The engine contains two injector banks, each containing 11 flush wall injectors. The secondary stream of the engine is intended to be operated at $\phi = 1$, even though the rocket provides some additional fuel, causing the complete engine to operate at $\phi > 1$. The portion of the fuel which is injected through each injector bank can be modified, and

this provides a method of engine control. Because the thermal throat location determines the mass flow rate of the engine, modulations in fuel injection are intended to control the location of the thermal throat. The ratio of the fuel mass flow rate of the upstream bank to the fuel mass flow rate of the downstream bank affects the extent of fuel penetration into and mixing with the incoming air. Distributing the fuel evenly between the two banks provides for minimum penetration and maximum mixing. Three different fuel injection scenarios were simulated at $p_c = 750\,\text{psi}$. The conditions and resulting inlet mass flow rates are given in the following table. Case A corresponds directly to IRS NCSU 750.

case	upstream fueling	downstream fueling	inlet mass flow rate
A	100 %	0 %	8.11 lbm/s
B	50 %	50 %	7.59 lbm/s
C	0 %	100 %	8.94 lbm/s

Table 4: Variations of IRS NCSU 750 used for fuel injection study

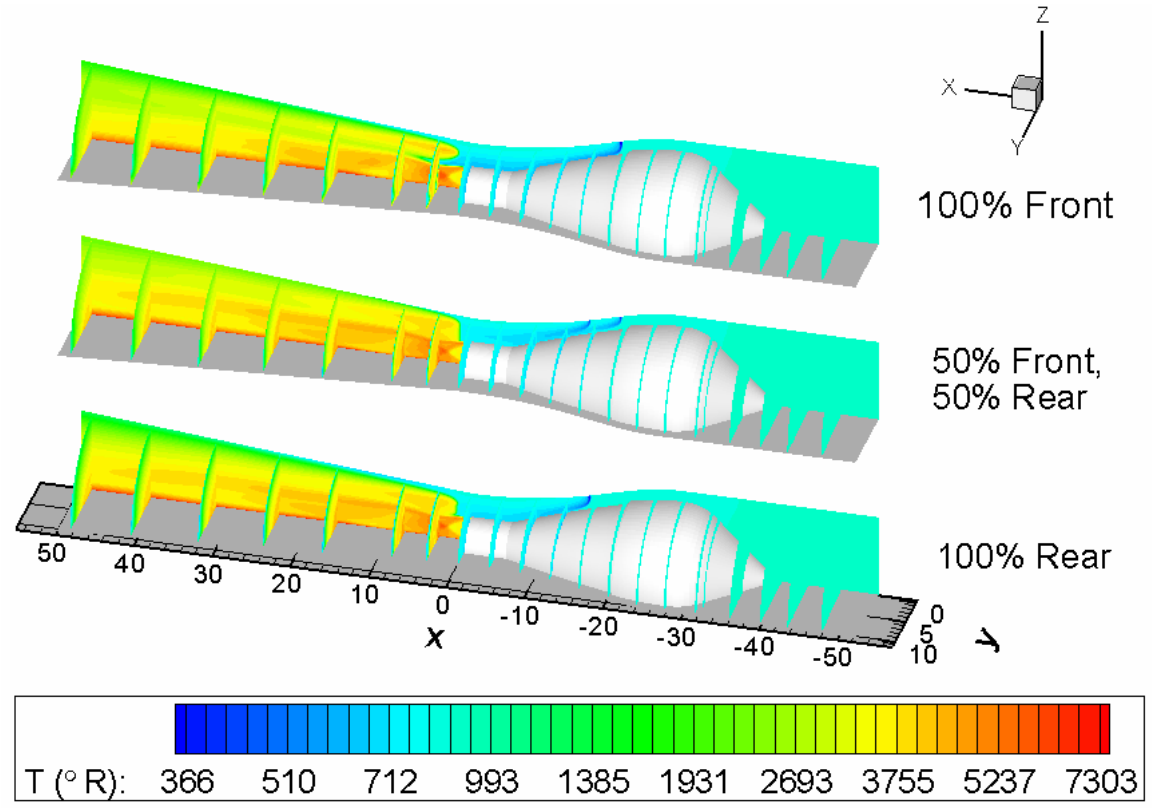

Figure 23: Temperature contours for fuel injection study

When the fuel is divided evenly between the two banks, the penetration is approximately halfway through the incoming air stream. This results in better mixing than the cases where all of the fuel is injected through one bank or the other. Better mixing results in higher heat release, which in turn pushes the thermal throat forward. However, heat release is not the only factor influencing thermal throat location; the flame speed is also a function of local equivalence ratio, and poor mixing can result in regions of lower equivalence ratio, which in turn allows for faster flame propagation.[27] Since case B had the most uniform mixing and highest heat release (see Figure 23 and Figure 25), its thermal throat is the farthest forward. However, even though the mixing is the worst for case A, the thermal throat for that case is farther forward than for case C. This

is caused by a combination of two factors which together are enough to overcome the tendency for the thermal throat to move back due to less mixing and heat release. The first factor is that the fuel rich area near the rocket plume retards the secondary combustion and allows for increased expansion of the primary flow which in turn constricts the secondary flow and accelerates the combustion closer to the cowl. Also, the fuel lean portion of the secondary flow farther away from the primary stream burns faster because of the lower equivalence ratio. Figure 23 shows the temperature contours for the three cases. The shocks and fuel injectors are visible in this plot as well, and the differences in flame structure can be seen.

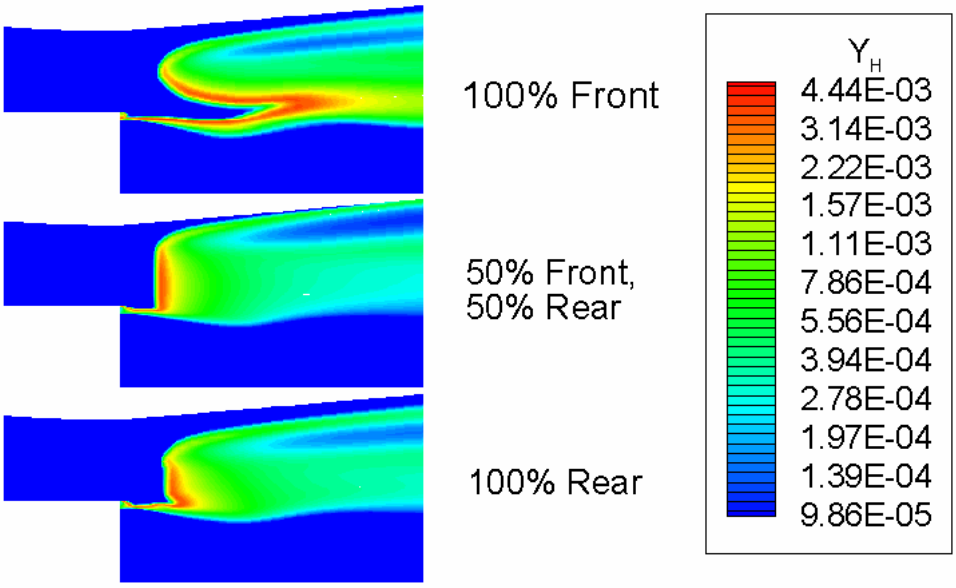

Figure 24: Close-up of flame structure for fuel injection comparison

The area of inhibited combustion for case A shows up as a cooler area between the premixed flame and the rocket plume in Figure 23. The differences in flame structure are more pronounced in Figure 24, which shows mass fraction contours for monatomic hydrogen. The more uniform the mixing (as in case B), the more normal the flame front is relative to the velocity. The higher the gradient in equivalence ratio (as in case A), the more curvature is present in the flame front. Figure 25 shows the equivalence ratio contours limited to $0.2 < \phi < 2$ (the flammability limits for hydrogen-air combustion at standard temperature and pressure). Areas of excess fuel and excess oxidizer are evident in this plot. For this plot, equivalence ratio is defined using the concentrations of oxygen and hydrogen atoms in all species, not just reactants:

$$\phi = \frac{1}{2}\frac{2c_{H_2} + 2c_{H_2O} + c_H}{2c_{O_2} + c_{H_2O} + c_O}$$

where c is the molar density, defined by the species density divided by the molecular mass, $c_j = \rho_j / M_j$.

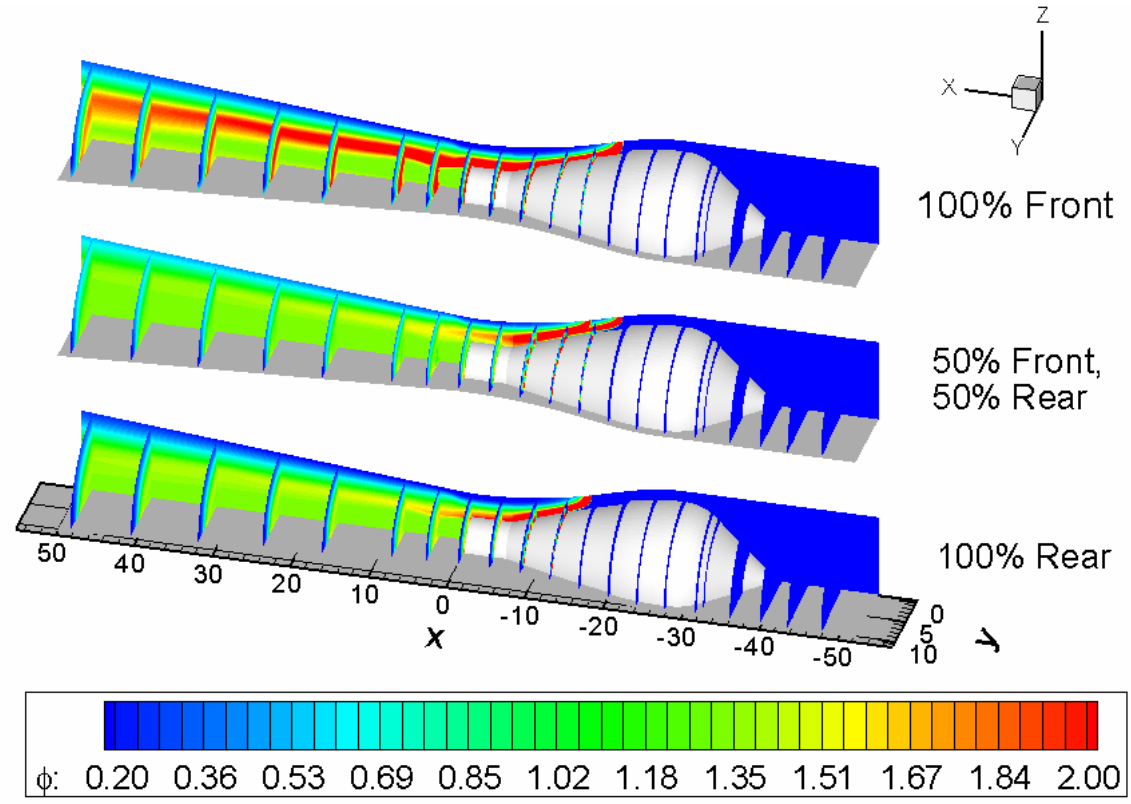

Figure 25: Equivalence ratio contours for fuel injection study

Throttle Down Process

The process of throttling down the rocket was modeled as a quasi-steady-state process by using the conditions for cases IRS NCSU 1500 through IRS NCSU 400 (see Table 3). In this sequence, case IRS NCSU 1500 was started from uniform initial conditions equal to the inlet conditions in the secondary flow and uniform initial conditions equal to the rocket exit conditions within the rocket plume. The next four cases in the sequence each used the preceding case for initial conditions while changing the boundary conditions to match the new rocket chamber pressure.

In the first three of these cases, the solutions were steady enough for the convergence criterion of 0.1% mass flow error to be met. However, for case IRS NCSU 500, fluctuations in mass flow rate only allowed the mass flow error to get within 1%. For case IRS NCSU 400, the fluctuations in mass flow rate only allowed a rate of 9% error to be achieved. This is because the rocket plume had a stabilizing effect on the flame structure and flow within the secondary stream. As the rocket mass flow rate decreased, and it became less significant compared to the secondary stream, the secondary flow became less steady. For a flow with such a large mass balance error, it would have been preferable to perform a time-accurate calculation so that a statistical steady state could be calculated. However, limitations on computer resources prevented such a simulation. Since future validation work will be more productive on steady cases, the initial IRS experimental test matrix should contain cases with conditions that the CFD analysis has predicted to be stable.

Figure 26 shows the Mach number contours for all five cases. The position of the thermal throat in the secondary stream can be seen for each case. In all of these cases, the

rocket is overexpanded, so a system of shocks is present in the rocket plume. For the 400 and 500 psia chamber pressure cases, the rocket is overexpanded enough for a Mach disk to form behind the rocket exit. A Mach disk forms whenever the deflection angle θ is higher than the maximum deflection angle θ_{max} as determined by the $\theta-\beta-M$ equation for M_2, which is the Mach number behind the first oblique shock but in front of the reflected shock. The $\theta-\beta-M$ equation for the shock wave dividing region 2 from region 3 is given by[28]

$$\tan\theta_{2-3} = 2\cot\beta_{2-3}\left[\frac{M_2^2\sin^2\beta_{2-3}-1}{M_2^2(\gamma+\cos 2\beta_{2-3})+2}\right]$$

where β is the shock angle and γ is the ratio of specific heats.

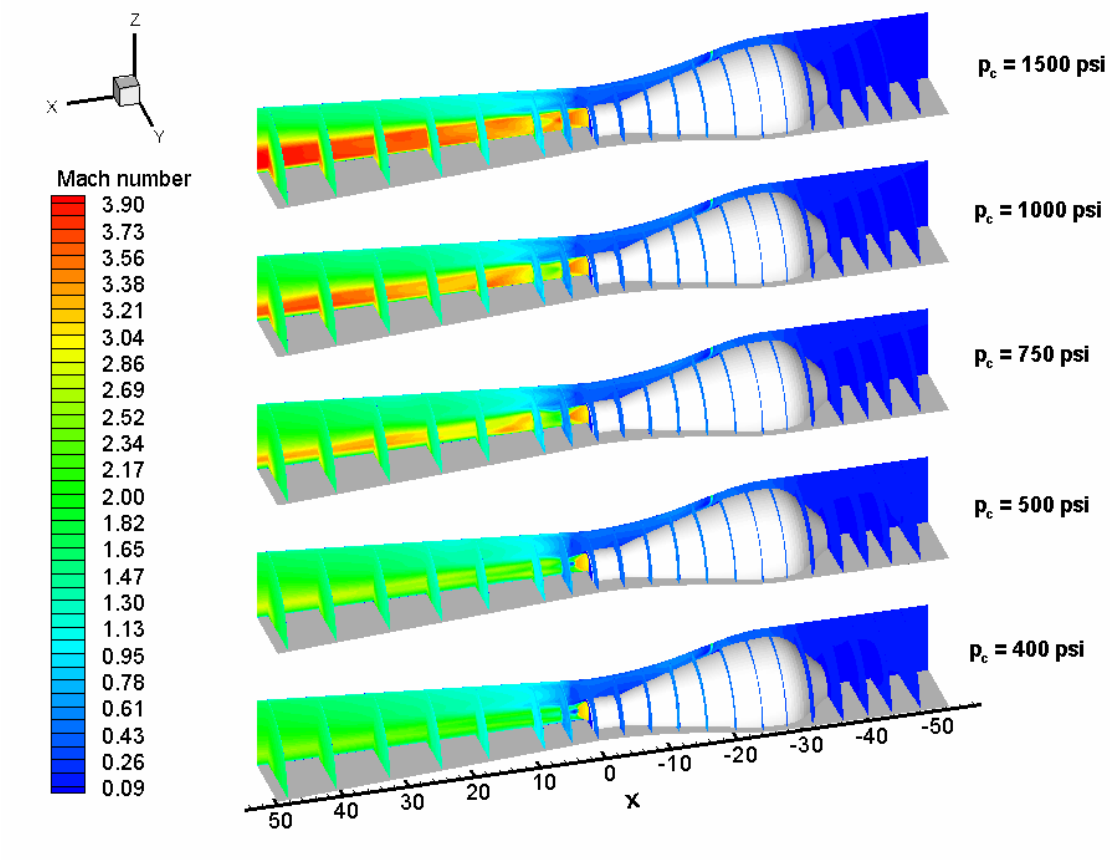

Figure 26: Mach number contours for all five steady IRS solutions

The extent to which the rocket plume displaces and mixes with the secondary stream can be seen more clearly in the nitrogen mass fraction contours shown in Figure 27. Because nitrogen is modeled as an inert species, and because the rocket contains no nitrogen, pure rocket exhaust shows up in blue; pure secondary flow shows up in red, and areas where the two are mixing show up in the range of colors in-between. This plot demonstrates why thermal choking must be initiated at a high chamber pressure. The effective combustor divergence angle for the secondary flow is much lower at high chamber pressures because the rocket plume fills a larger portion of the diverging duct. This lowers the heat release necessary to overcome the area change and allows the thermal throat to form. Note that the injectors show up as areas voided of nitrogen.

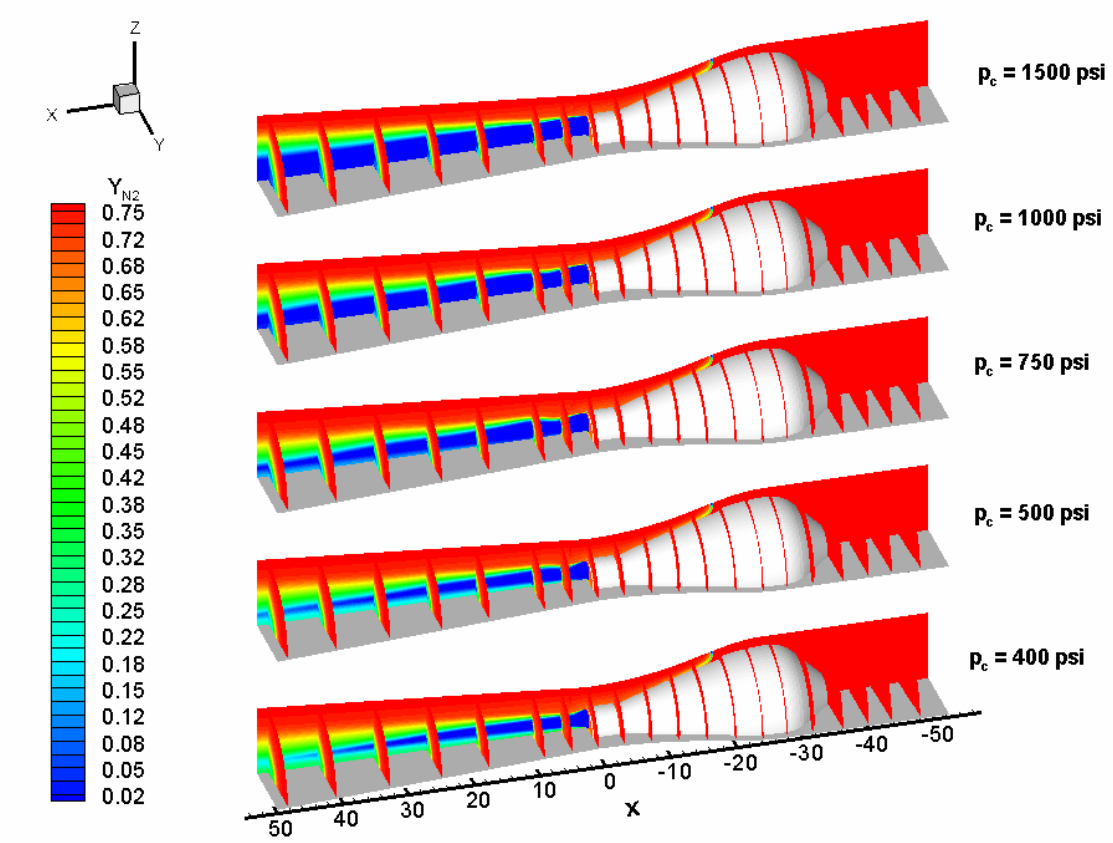

Figure 27: N_2 mass fraction contours for all five steady IRS cases

Rocket Cutoff

An unsteady rocket cutoff simulation starting at a chamber pressure of 400 psia is necessary for several reasons:

1. It tests whether or not the partially premixed flame structure established for the 7-species / 7-reaction mechanism is dependent on the rocket plume as either a source of ignition or flame stabilization at the specified conditions.

2. It simulates a worst-case scenario for flight conditions, since the time scale used for rocket shut down in the CFD simulation is much shorter than the time scale for flight.
3. It gives a time-accurate record of the unsteady flow within the combustor—something that was not possible for the steady calculations done with case IRS NCSU 400.

Figure 28 and Figure 29 show the temperature contours along the symmetry plane for 16 frames extracted from the time history. As time progresses, and the mass flow is lowered, the system of shocks in the overexpanded rocket exhaust moves forward into the rocket bell until it eventually reaches the throat and unchokes the nozzle. At this point, the flow within the rocket becomes asymmetric because the subsonic flow becomes susceptible to the influence of circulating secondary flow behind the centerbody. The temperature behind the rocket drops to around 3300 ˚R, which is slightly cooler than the secondary flow behind the flame front (3800 ˚R). The flow inside the plenum remains hotter because the hot combustion products are never purged. The flame remains lit throughout the cutoff process and afterwards, indicating that the flame is not dependent upon the rocket plume as an ignition source, but it is possible that the hot gases in the recirculation zone are still stabilizing the flame.

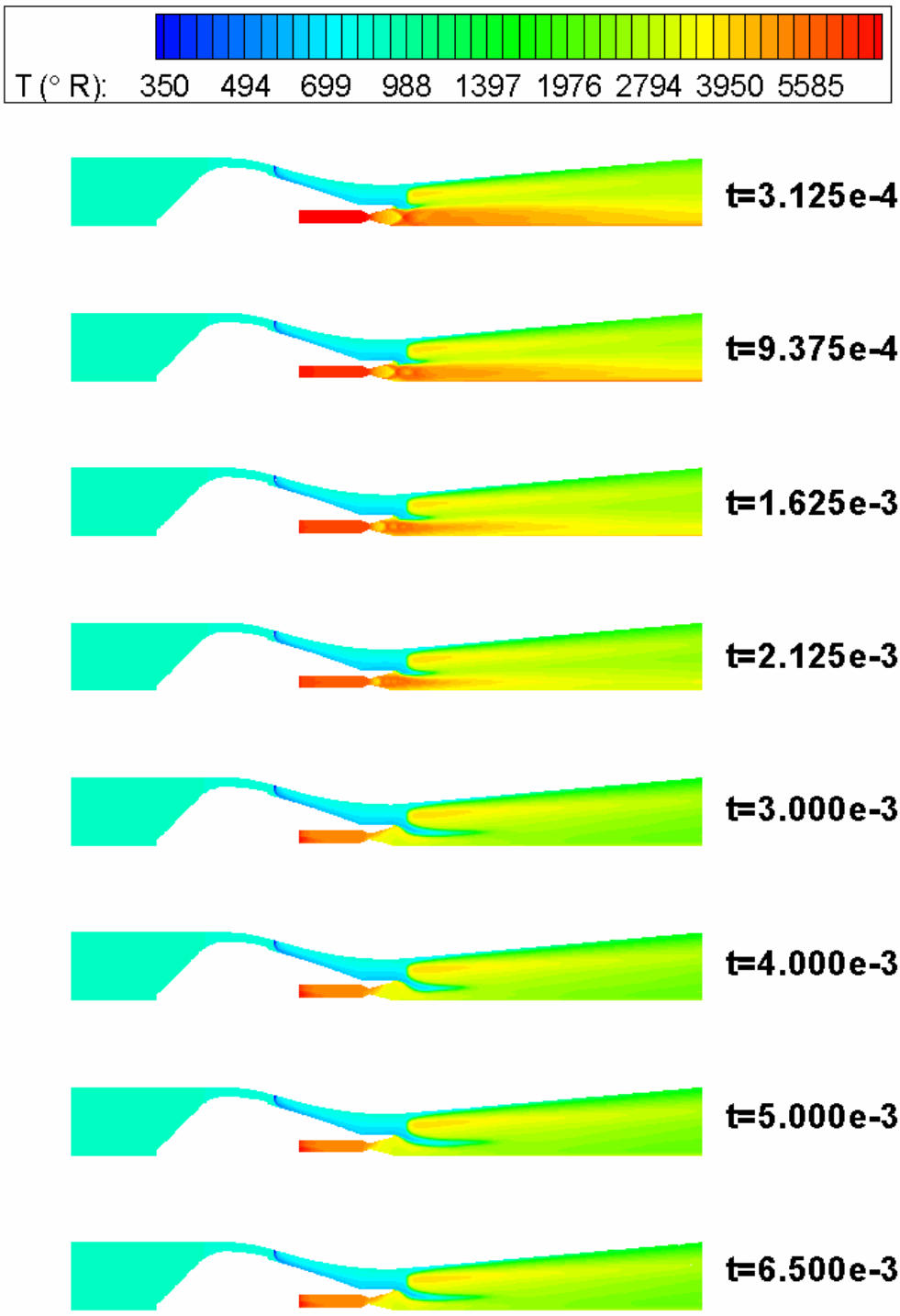

Figure 28: Temperature contours on frames 1-8 of rocket cutoff simulation

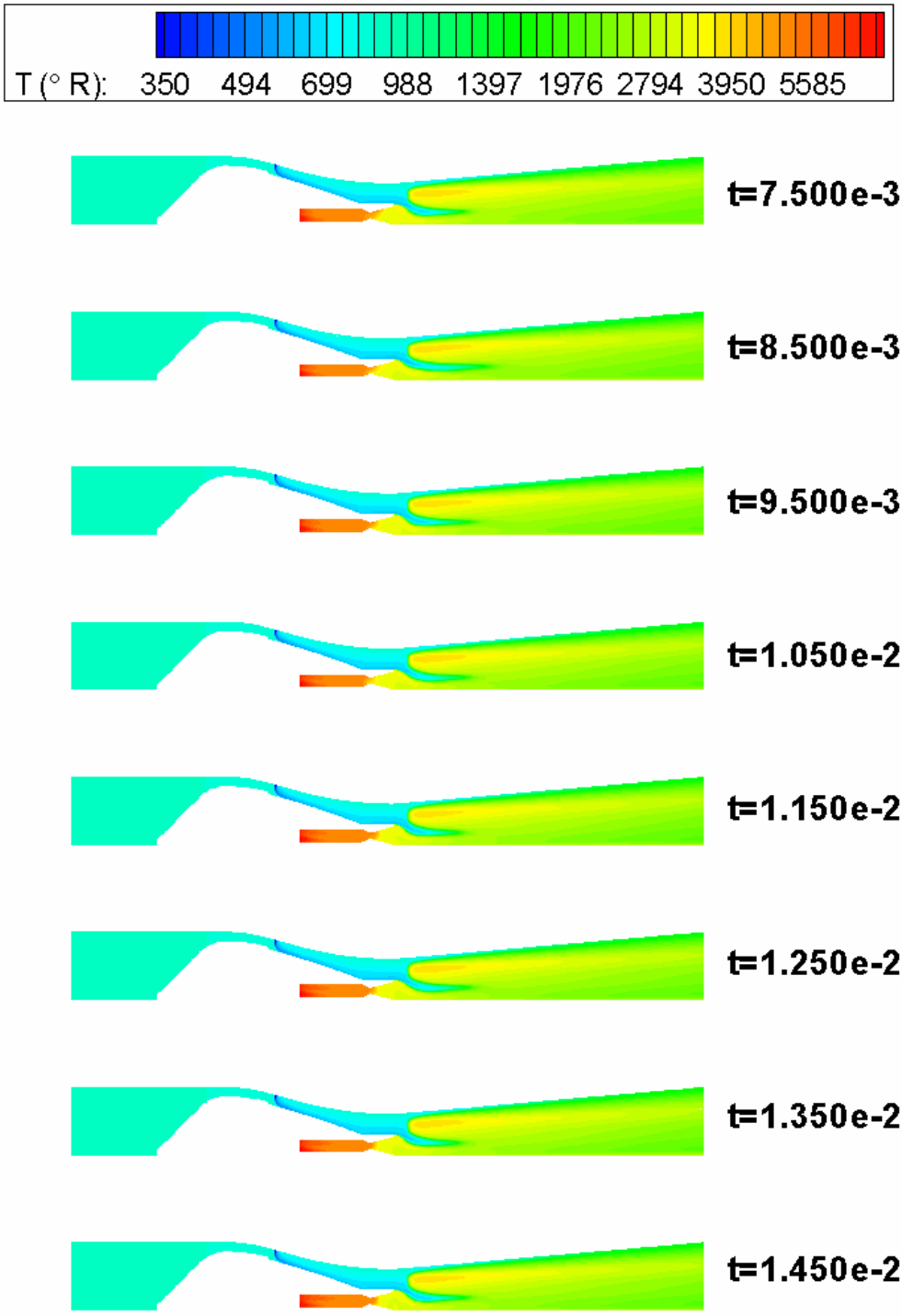

Figure 29: Temperature on frames 9-16 of rocket cutoff simulation

Figure 30 and Figure 31 show the monatomic hydrogen mass fraction contours for the 16 frames of the rocket cutoff simulation. The same basic structure seen for all of the steady IRS cases is present in the solution after cutoff (partially premixed triple flame with rich, lean, and diffusion branches—Figure 20 labels these structures). The lean premixed branch and the diffusion branch appear fairly stable following the rocket cutoff, but the rich premixed branch is highly oscillatory. This may be in part due to chemistry, but the most likely dominant source of the instability is the recirculating flow behind the centerbody. This could explain why the unsteadiness increases as the chamber pressure is dropped. Since the rocket plume fills less of the area behind the centerbody, more secondary flow recirculates in the region formerly filled by the rocket exhaust. The recirculation region can be seen more clearly in Figure 32, which shows the stream traces along the symmetry plane and an oil pattern along the flat plate for the last frame of the cutoff simulation.

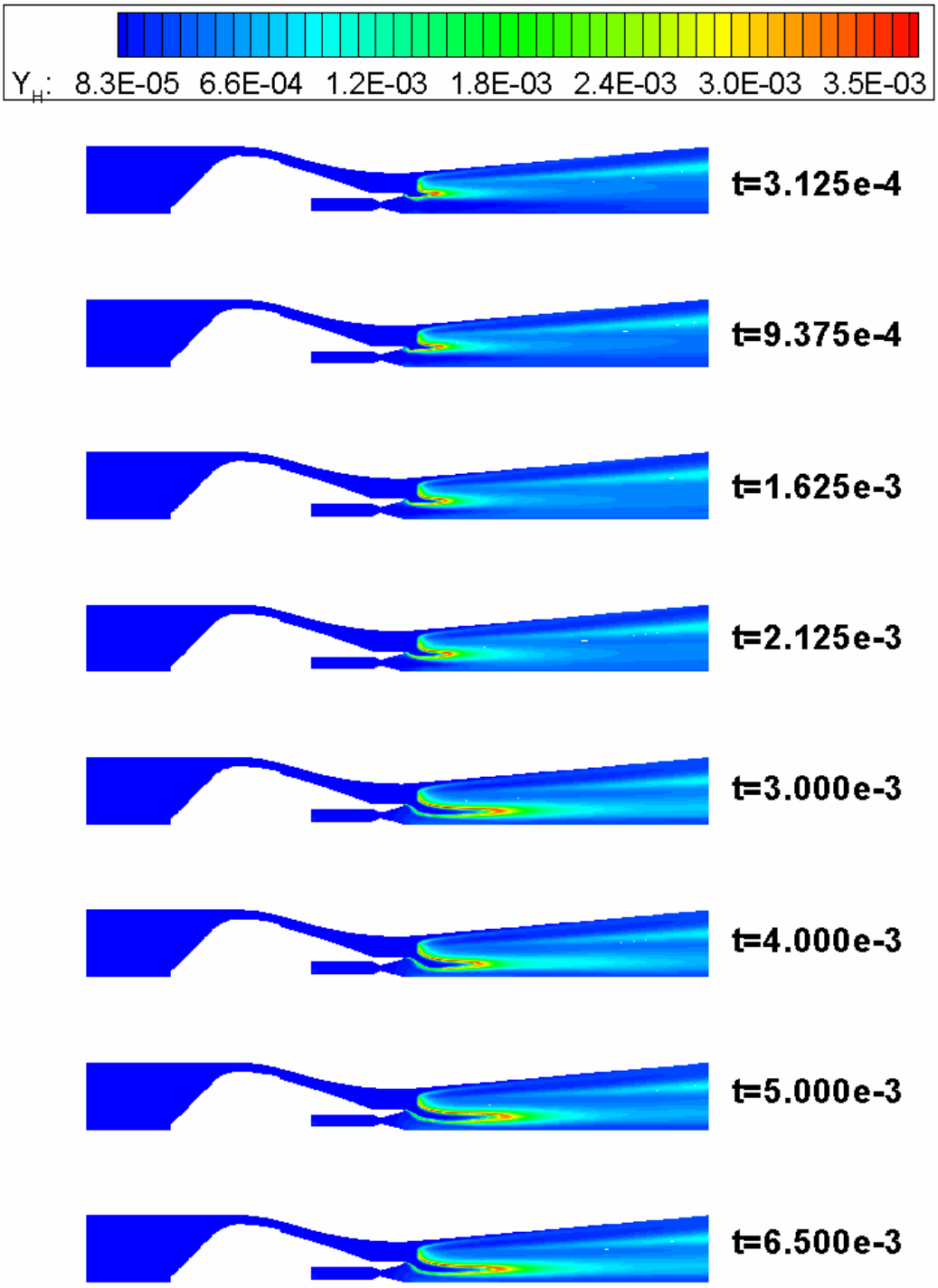

Figure 30: H mass fraction contours on frames 1-8 of rocket cutoff simulation

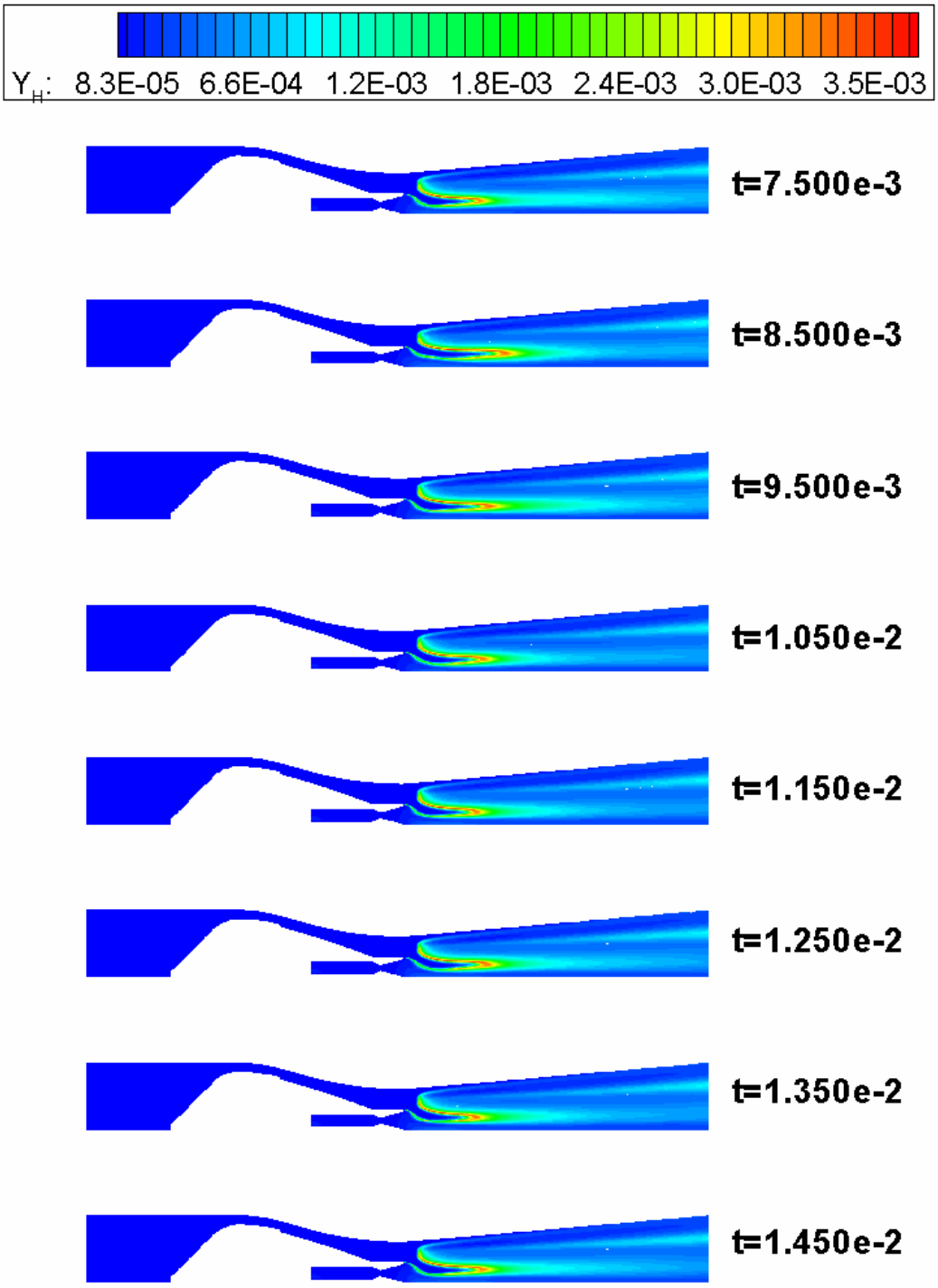

Figure 31: H mass fraction contours on frames 9-16 of rocket cutoff simulation

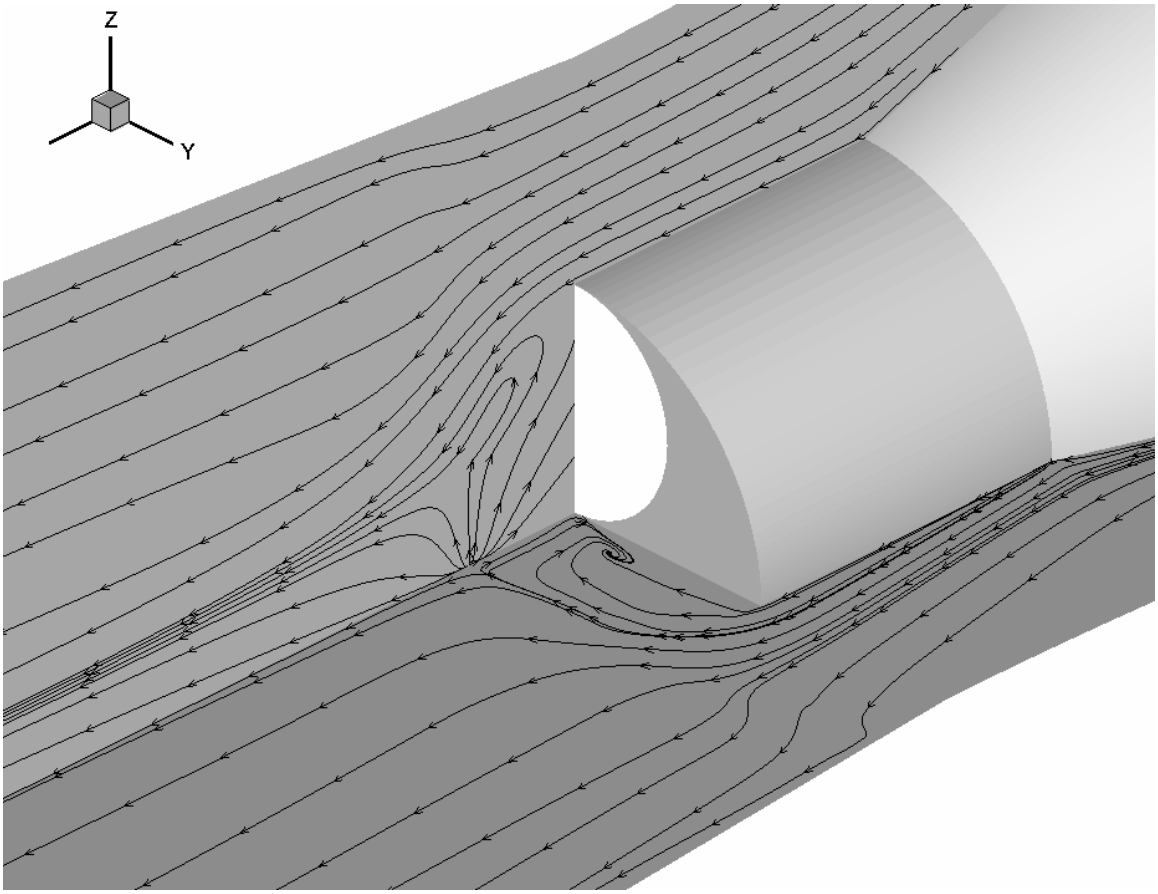

Figure 32: Stream traces and oil pattern on last frame of rocket cutoff simulation

Rocket Purge

Although the rocket cutoff simulation addressed several important issues, it left two questions unanswered:

1. Is the flame structure a true lifted flame, or does the region of recirculating hot gas behind the centerbody act as an anchor?
2. Will the nitrogen purge, which is necessary for safety in the experimental tests, extinguish the flame?

The first of these questions relates to the analysis of the reaction model. If the flame structure is truly unanchored, then it is either propagating or auto-igniting. Even though no experimental data exists for the model engine under these conditions, conclusions about the reliability of the reaction mechanism can be drawn from what is known about auto-ignition and flame propagation of hydrogen-air mixtures. The second question is relevant to the design of IRS experiments. If the nitrogen purge is likely to extinguish the flame, then an alternative safety procedure needs to be developed before reliable mode transition experiments can be conducted.

Figure 33 through Figure 35 show the temperature contours on the symmetry plane from 24 frames of the time history. Since the nitrogen used for the purge is far colder (872.7 $^{\circ}$R) than the plenum products (7554 $^{\circ}$R), the purge can be seen in this plot as a region of colder gas moving through the rocket and eventually into the combustor. Because the mass flow of nitrogen during the purge stays at the same level as that of the rocket while lit (1.307 lbm/s), and the density of diatomic nitrogen is much higher than the density of the rocket products at a mass ratio of 6, the rocket actually unchokes during the purge. The cold nitrogen exiting the rocket nozzle convects most of the hot gases behind the centerbody downstream. However, there are still some hot gases present which might be anchoring or stabilizing the flame. After the purge is completed, and the recirculation region establishes itself behind the centerbody, the solution enters the same oscillatory cycle of that seen in the rocket cutoff simulation without the purge.

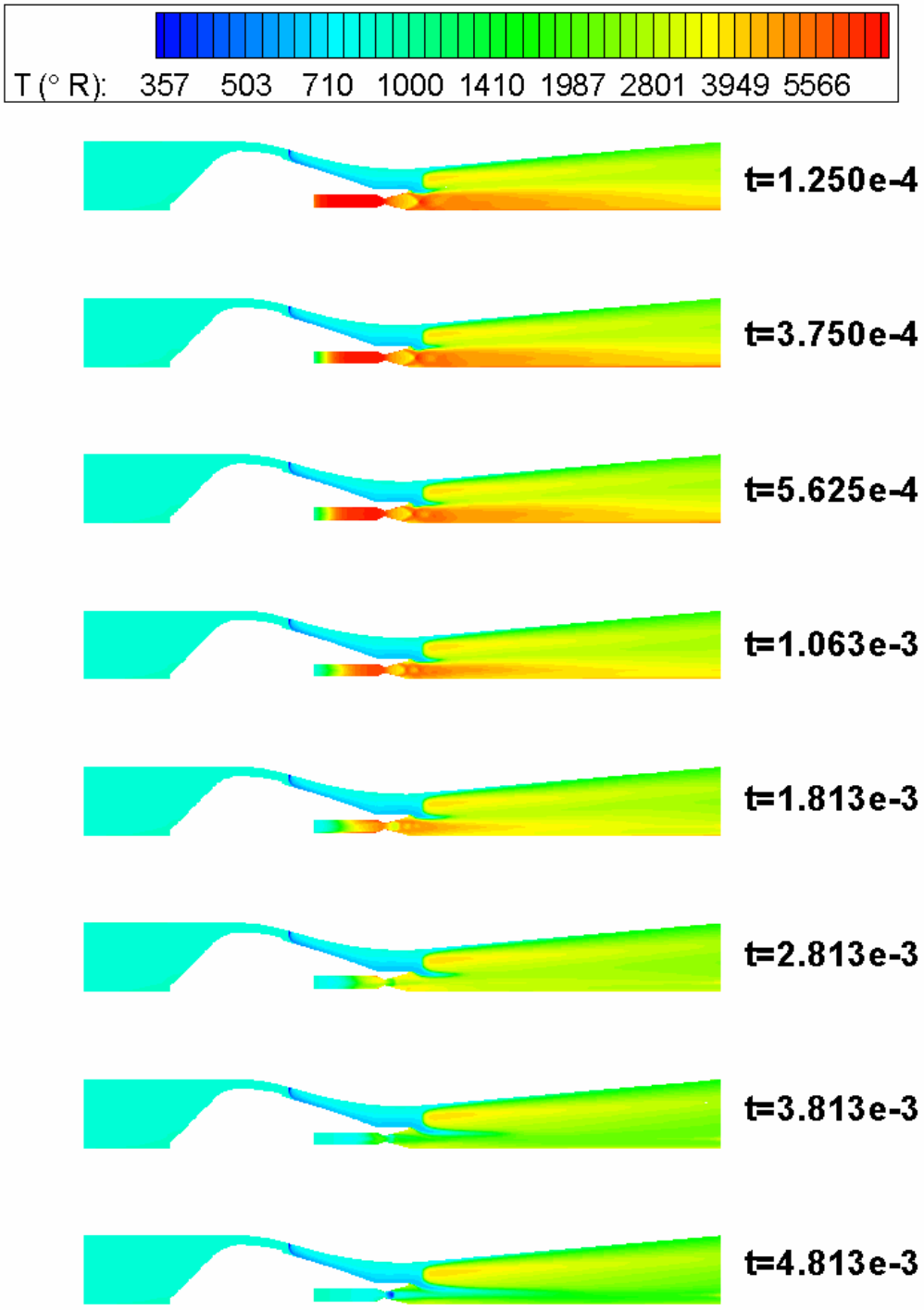

Figure 33: Temperature on frames 1-8 of rocket purge simulation

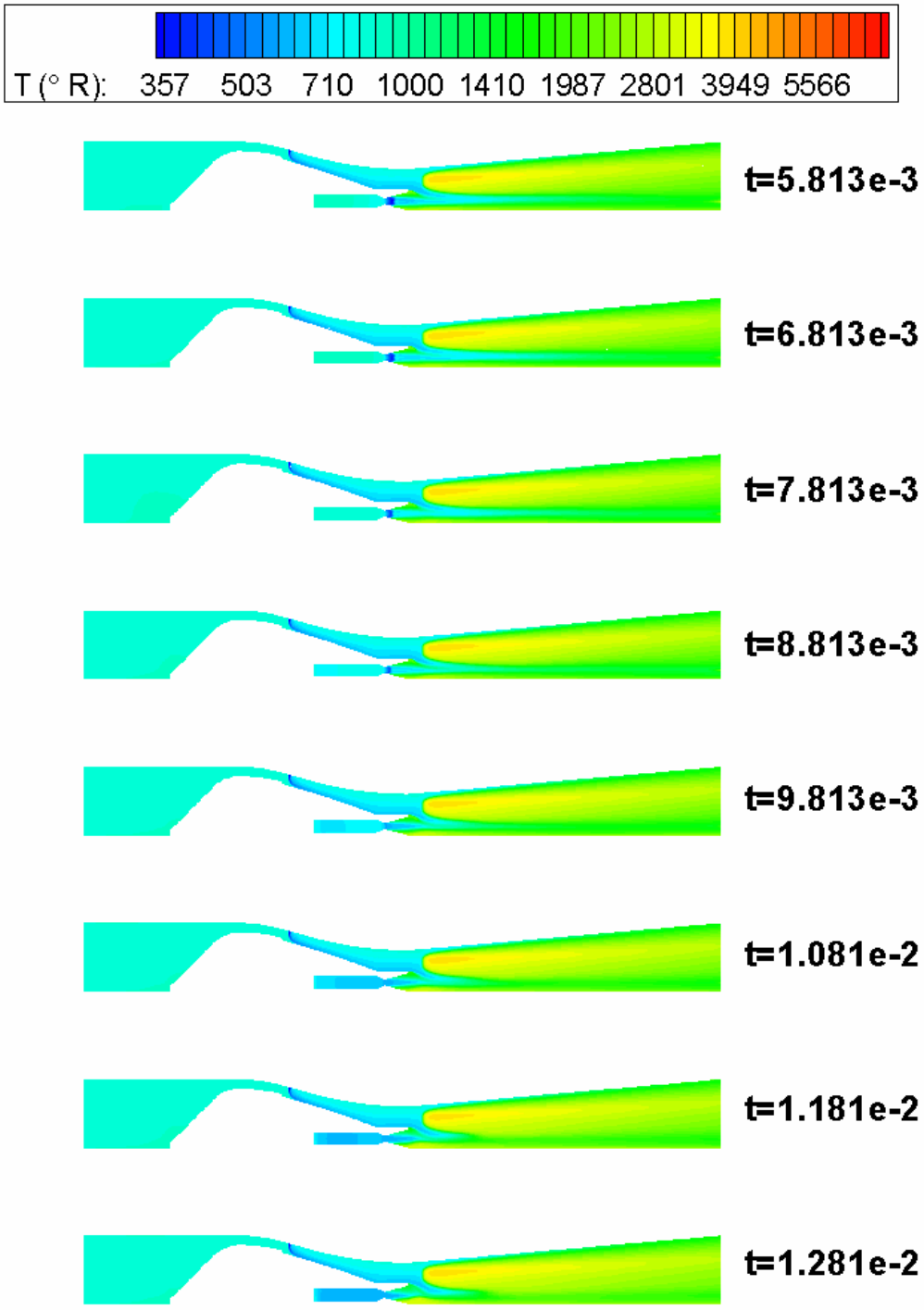

Figure 34: Temperature on frames 9-16 of rocket purge simulation

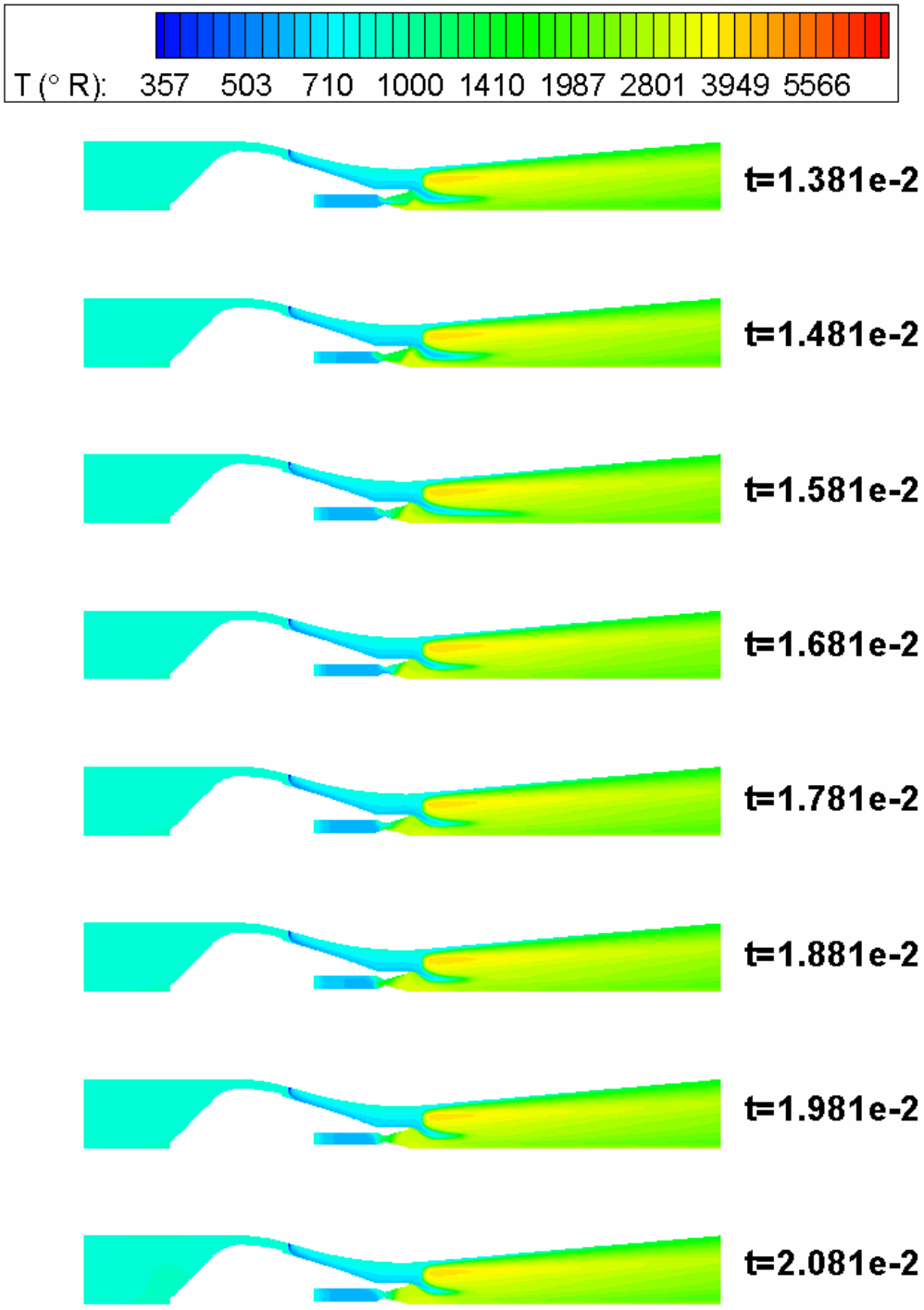

Figure 35: Temperature on frames 17-24 of rocket purge simulation

The purge can be seen in greater contrast in the nitrogen mass fraction contours. These contours on the 24 frames of the solution are given in Figure 36 through Figure 38. The nitrogen can be seen moving through the rocket plenum, then the nozzle, and finally into the combustor. Once the purge is completed, the nitrogen inside the rocket stagnates and remains, while the nitrogen in the combustor section is convected downstream and replaced by hot products. By the last frame, the only significant features still visible in the nitrogen contours are the fuel injectors and rocket plenum.

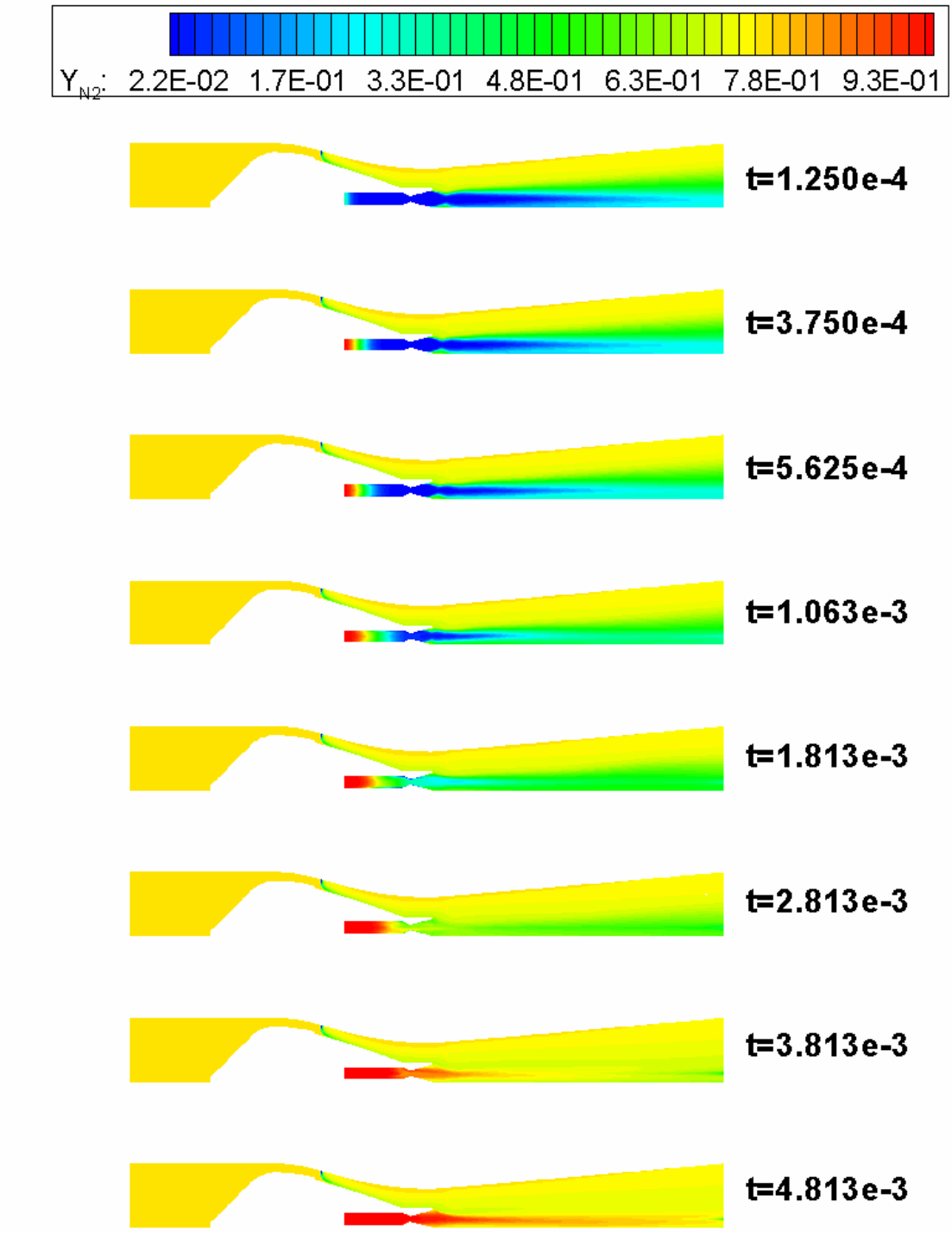

Figure 36: N_2 mass fraction contours on frames 1-8 of rocket purge simulation

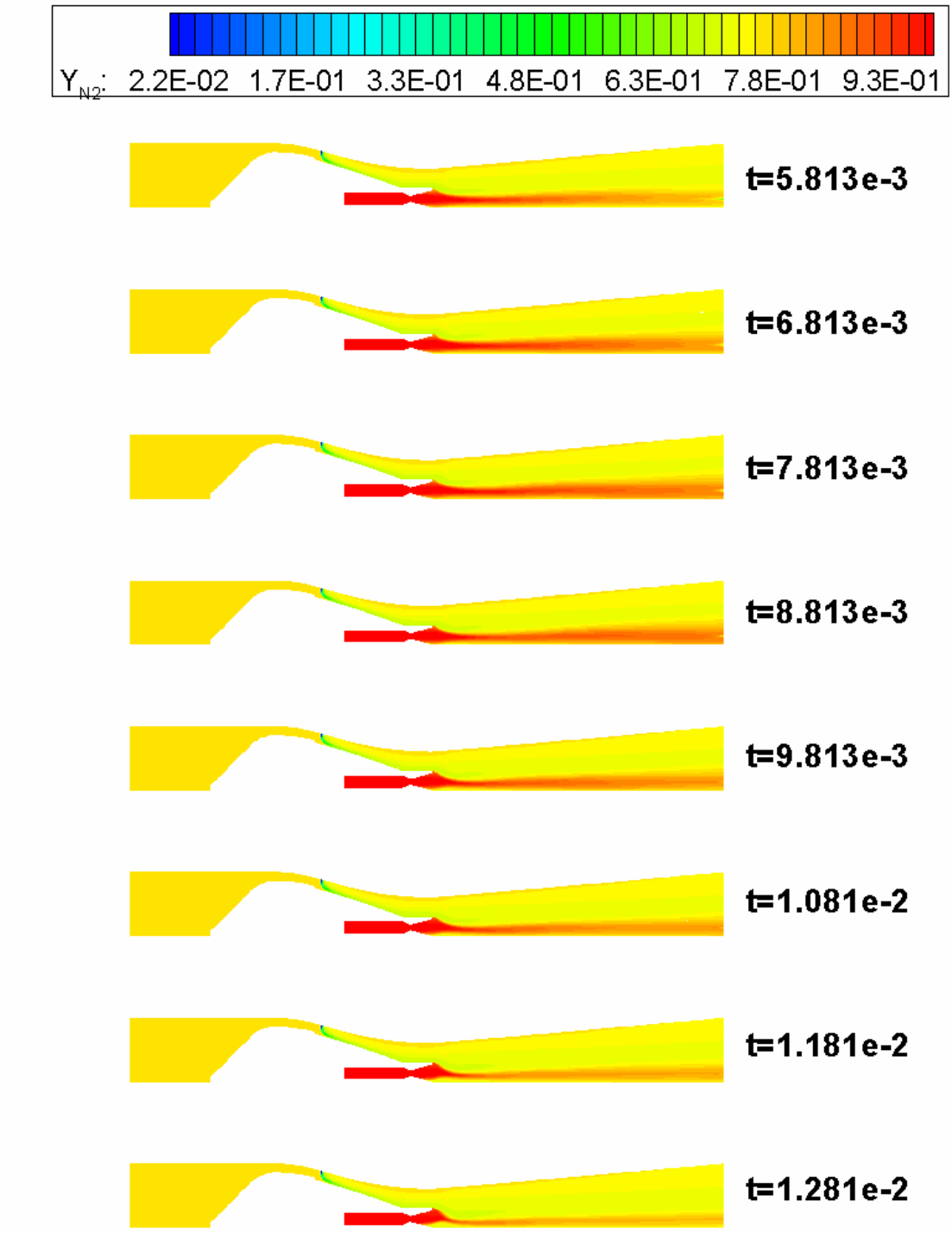

Figure 37: N_2 mass fraction contours on frames 9-16 of rocket purge simulation

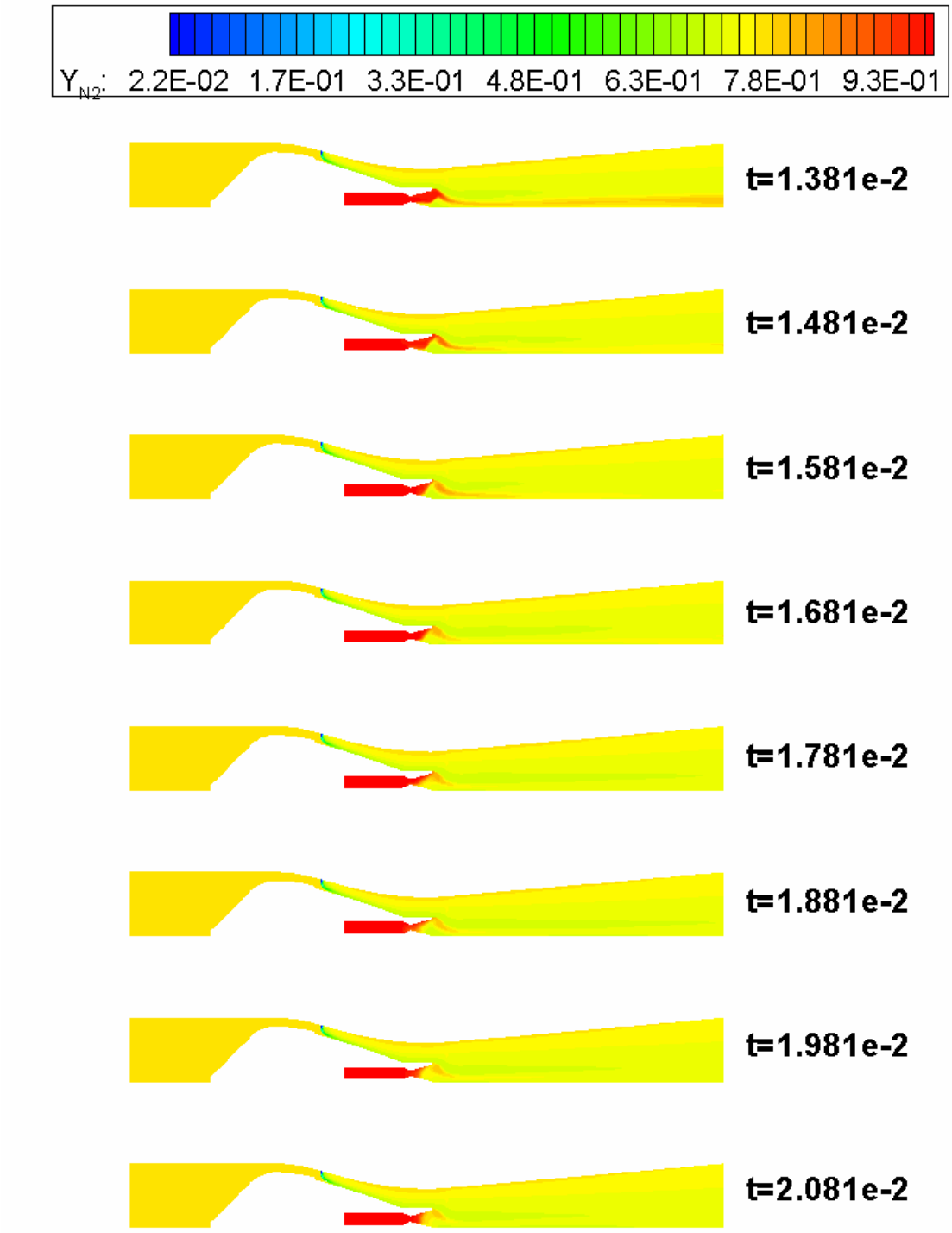

Figure 38: N_2 mass fraction contours on frames 17-24 of rocket purge simulation

The flame structure can be seen clearly in the contours of monatomic hydrogen. These contours are shown in Figure 39 through Figure 41. In the first 5 ms of the simulation, enough cold nitrogen has flowed through the rocket to completely detach the flame from any of the solid surfaces. This can clearly be seen in Figure 42, where the 3-D view at 12.3 ms is shown. Although it reattaches at around 15 ms, the flame remains stable in the interval between detachment and reattachment—confirming that the flame truly is a lifted flame burning in partially-premixed mode. Only two physical mechanisms, propagation and auto-ignition, can allow the flame to exist in this location. Unfortunately, because of the simplified nature of the 7-species mechanism, it is not possible to tell simply from the radical concentrations whether propagation or auto-ignition is being predicted. However, neither of these scenarios appears physically viable. The pressure and temperature (28.2 psia and 865 $^{\circ}$R, respectively) upstream of the flame are lower than accepted values for hydrogen-air auto-ignition, and the velocity upstream of the flame (492 ft/s) is higher than the estimated turbulent flame speed.

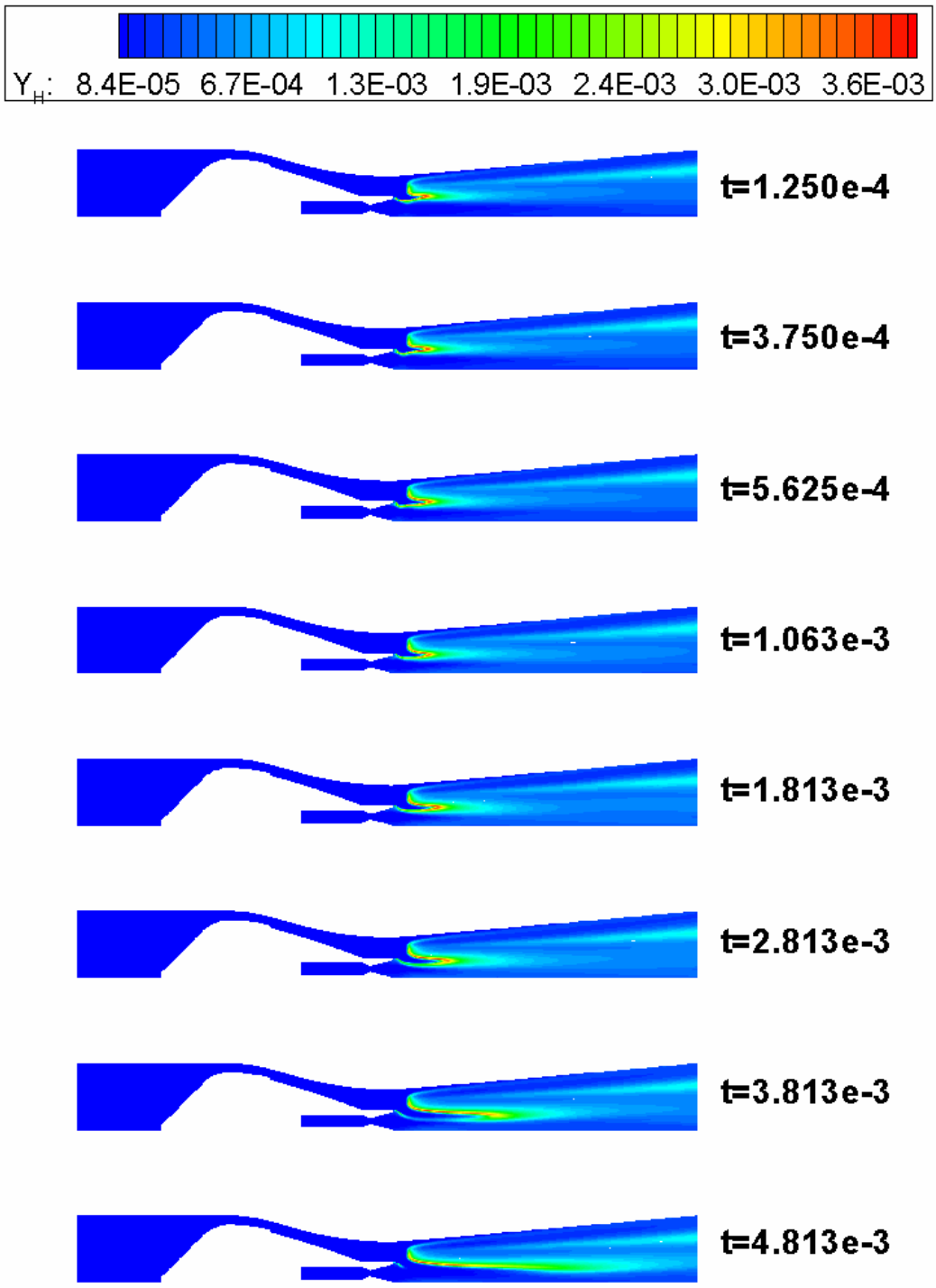

Figure 39: H mass fraction contours on frames 1-8 of rocket purge simulation

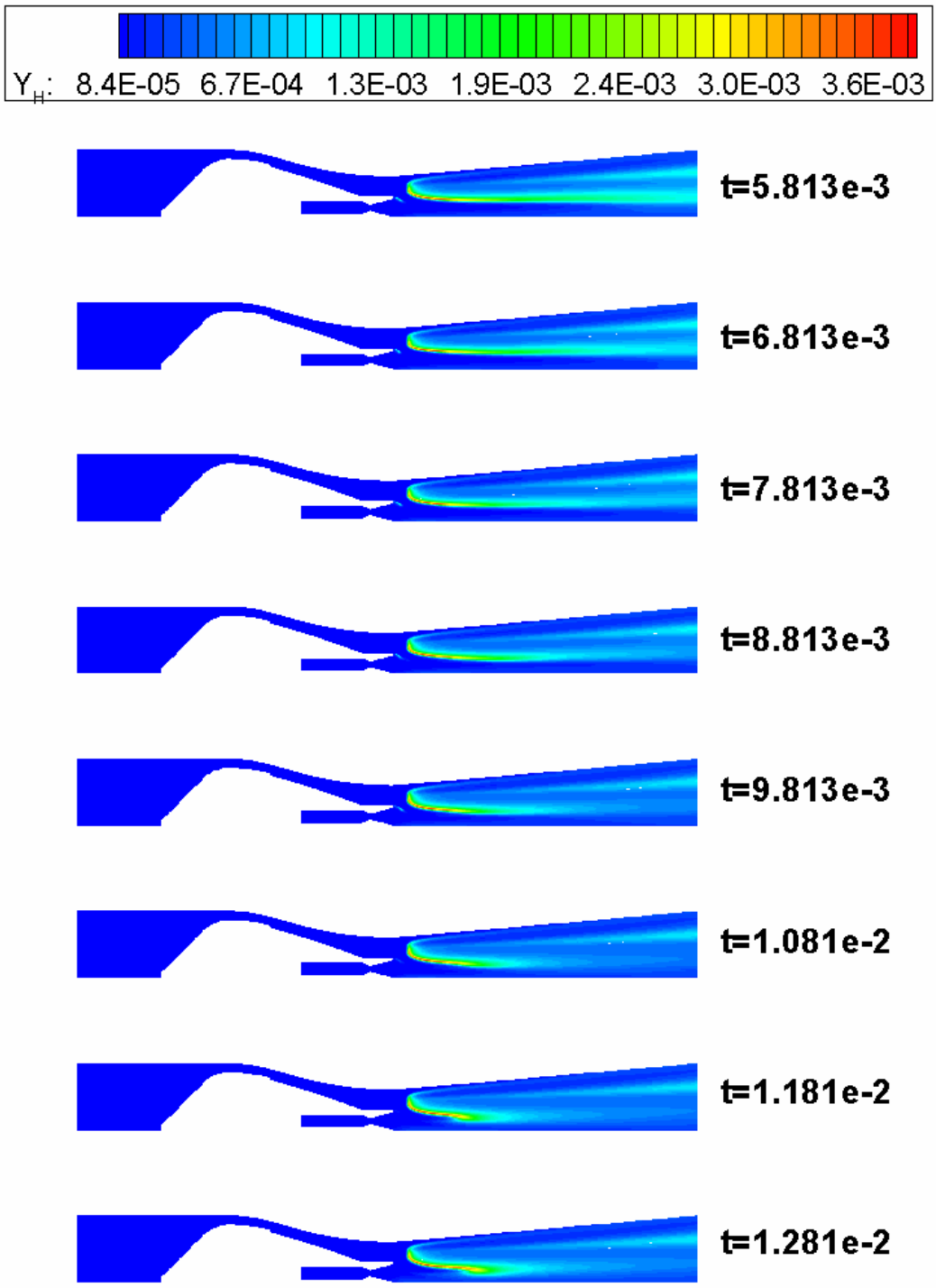

Figure 40: H mass fraction contours on frames 9-16 of rocket purge simulation

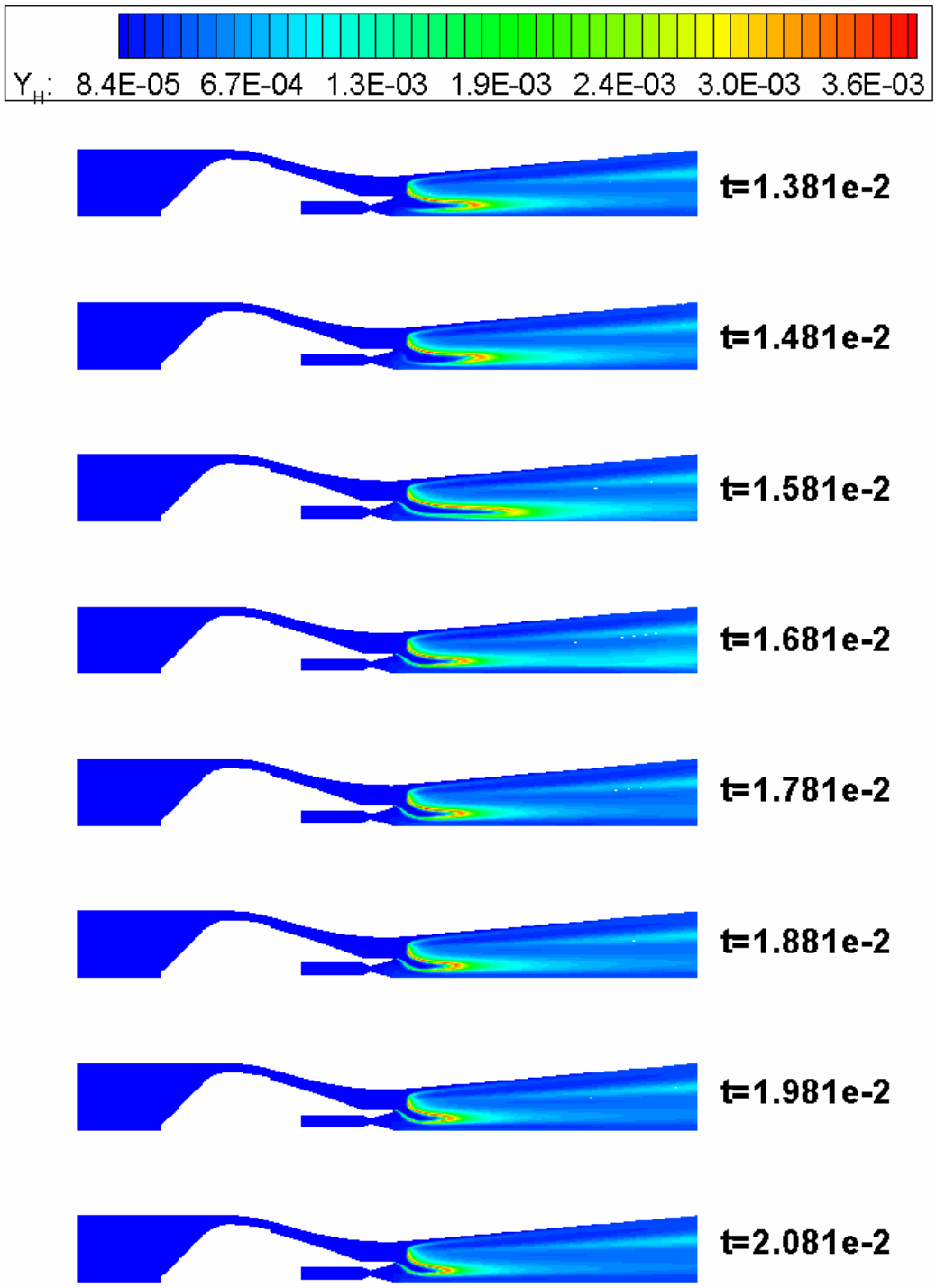

Figure 41: H mass fraction contours on frames 17-24 of rocket purge simulation

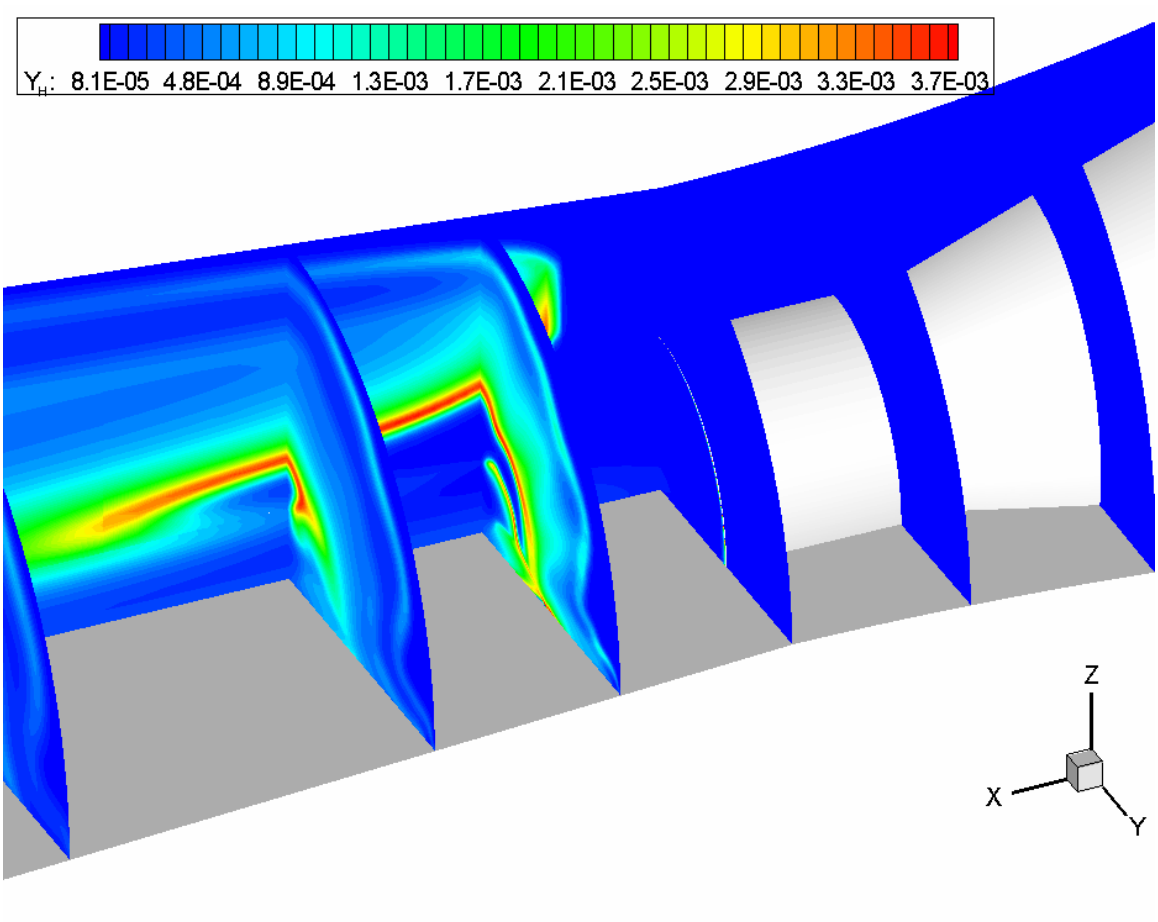

Figure 42: 3-D view of purge simulation at 12.3 ms

A rigorous examination of the flame propagation requires the extraction of the flame front surface. This surface can be extracted from the volumetric data set if a reaction progress variable, *G*, is introduced. For hydrogen-air combustion, *G* can be defined as:

$$G = \frac{c_{H_2O}}{c_{H_2O} + \min(c_{H_2}, 2c_{O_2})}$$

where c_s is the molar density of species s. $G = 0$ upstream of the onset of combustion and increases downstream. The maximum possible value for G is 1, although this only occurs for the theoretical case of 100% combustion efficiency.

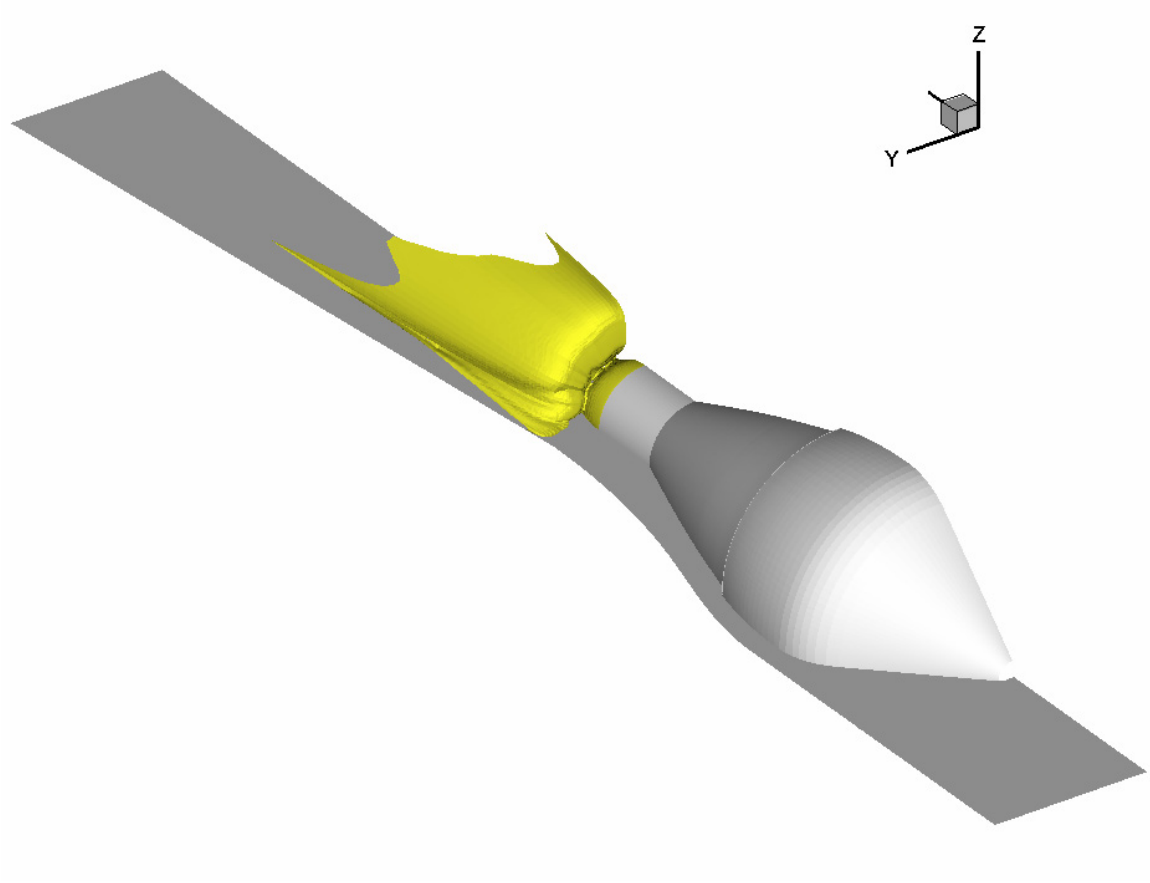

Figure 43: G=0.01 iso-surface showing flame front

The front of the flame is assumed to be the iso-surface where $G = 0.01$. This surface is shown yellow in Figure 43. The local turbulent flame speed, as predicted by the CFD code, is the velocity normal to this surface. This normal velocity can be compared to the turbulent flame speed equation of Zimont[29] and the partially-premixed turbulent flame speed equation of Peters[30]. The equation of Zimont is given by

$$s_T = A v_{RMS}^{3/4} s_L^{1/2} \alpha^{-1/4} l^{1/4}$$

and the equation of Peters is given by

$$\frac{s_T - s_L}{v'} = -\frac{a_4 b_3^2}{2b_1} Da + \sqrt{\left(\frac{a_4 b_3^2}{2b_1} Da\right)^2 + a_4 b_3^2 Da}$$

where s_T is the turbulent flame speed; v_{RMS} is the root mean squared of the fluctuating velocity magnitude; α is the molecular heat transfer coefficient; v' is the turbulence intensity; Da is the Damköhler number, and A, a_4, b_3, and b_1 are constants. These quantities are defined by

$$v_{RMS} = \sqrt{k}$$

$$\alpha = \frac{\mu}{\rho \,\mathrm{Pr}}$$

$$v' = \sqrt{\frac{2}{3}k}$$

$$Da = \frac{s_L l}{v' l_F}$$

$$l = \frac{\sqrt{k}}{\omega}$$

$$a_4 = 0.78 \quad b_1 = 2.0 \quad b_3 = 1.0$$

s_L and l_F are the laminar flame speed and thickness, respectively. Each of these can be calculated for a given reaction mechanism as a function of temperature, pressure, and equivalence ratio by the PREMIX code from the CHEMKIN library.[31,32] Calculating these values for the entire (ϕ, T, p) space would have been expensive, so these three variables were examined along the $G = 0.01$ iso-surface for correlation.

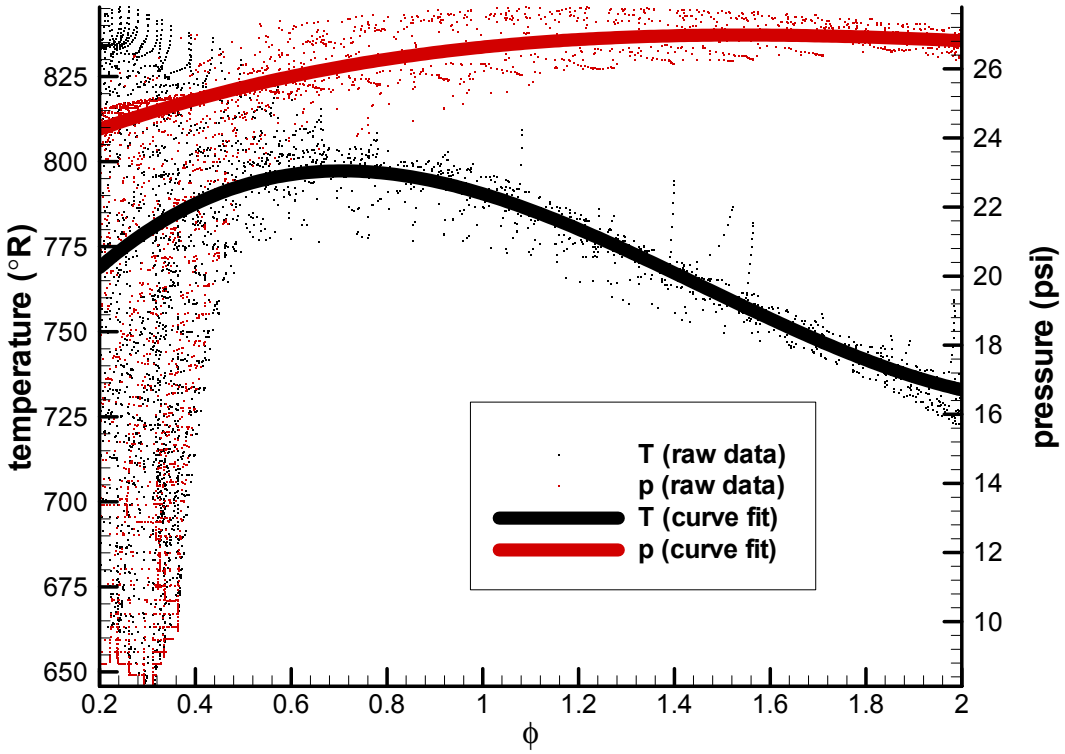

Figure 44: Temperature and pressure versus equivalence ratio at flame front

The curve fits for T and p are expressed as

$$T = 439.38 - 28.221Z - 43.262Z^2$$

$$p = 1.8161 + 0.080388Z - 0.098958Z^2$$

where

$$Z = \frac{\phi - \frac{1}{\phi}}{\phi + \frac{1}{\phi}}$$

These polynomials express T and p in Kelvins and atmospheres, respectively, since these units are required by the PREMIX code. Using these polynomials, s_L and l_F can be

reduced to functions of ϕ only. Thus, a series of values for s_L and l_F in the range $0.2 \le \phi \le 2$ can be interpolated and used to evaluate the Peters and Zimont expressions for s_T, at each point along the flame front. The PREMIX calculations were performed with the 7-species mechanism for consistency. Figure 45 shows the velocity normal to the flame as predicted by the CFD code and the turbulent flame speed estimates versus the local equivalence ratio. Although the trends are similar, the normal velocity is consistently an order of magnitude higher than the calculated estimates.

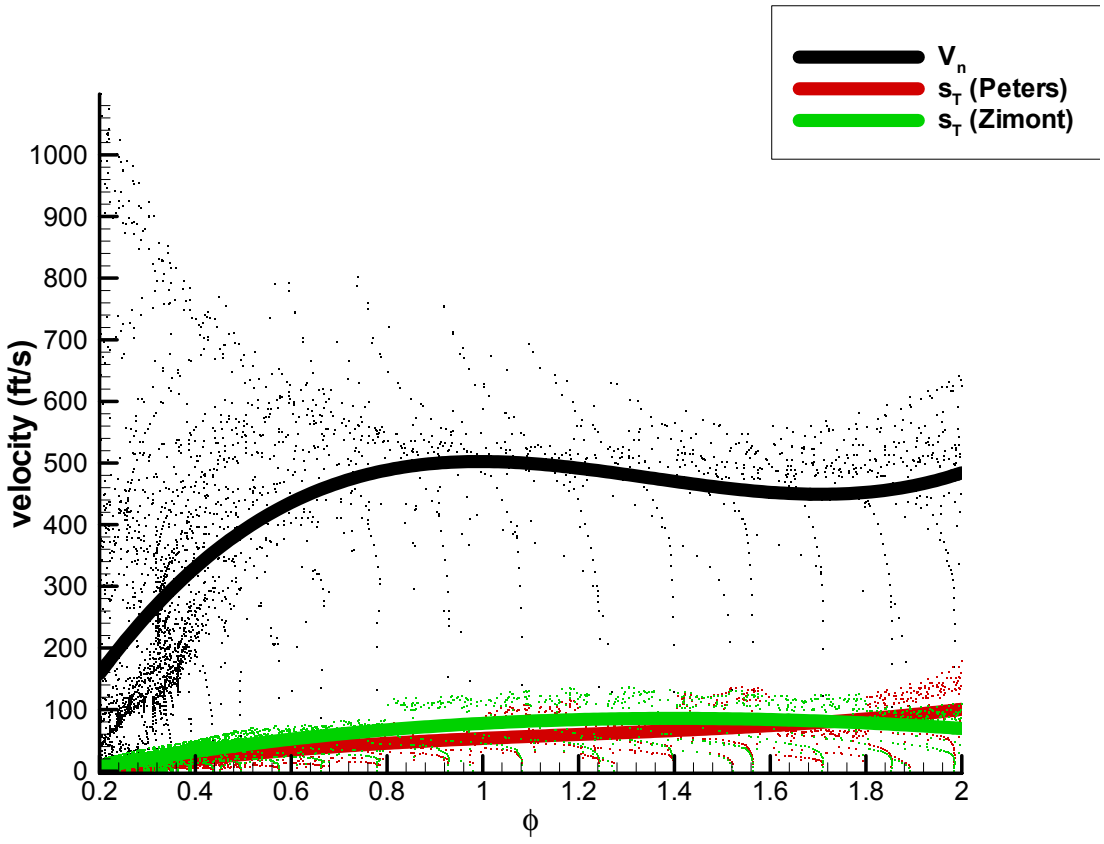

Figure 45: Turbulent flame speeds versus equivalence ratio

One thing that can be noted in Figure 45 is that the turbulent flame speed remains high in rich regions, unlike a flame speed versus equivalence ratio plot for constant temperature and pressure. The reason for this is the correlation between equivalence ratio and pressure. The pressure is higher in the rich region of the flow (*i.e.* behind the centerbody), so the usual drop in flame speed which would accompany the increase in equivalence ratio is offset by the effect of increased pressure. Figure 46 shows the velocity normal to the flame front and two turbulent flame speed estimates versus local static pressure.

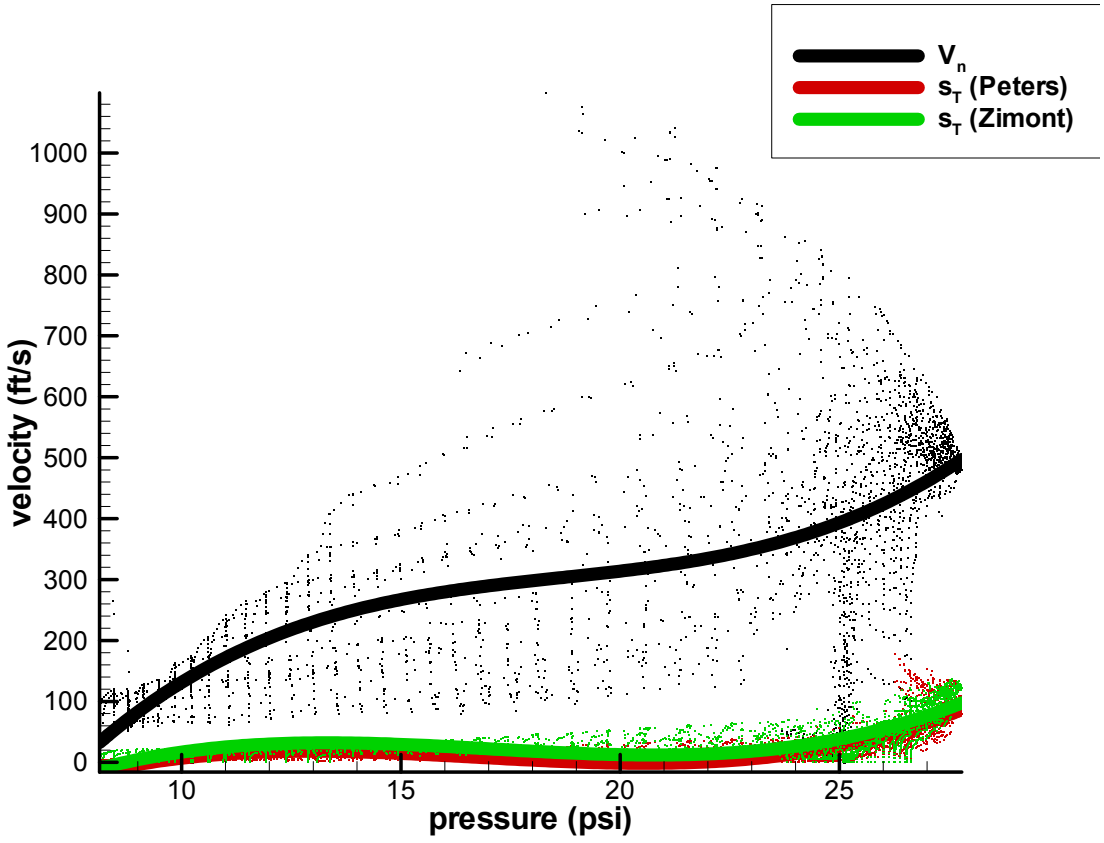

Figure 46: Turbulent flame speeds versus pressure

These plots show that the flame speed predicted by the 7-species mechanism in the CFD code shows the expected trends with respect to dependence on equivalence ratio and pressure. However, it is consistently an order of magnitude higher than the expected value. Thus, even though no experimental data on this rig can be compared with the IRS calculations, the existence of a lifted flame under these conditions is not very likely. The more likely scenario is that the flame is anchored behind the centerbody and propagates outward toward the cowl.

Conclusions

This dissertation has documented several numerical simulations of the GTX RBCC combustor in cold-flow, ejector-ramjet (ER), and independent ramjet stream (IRS) operation. The solutions for cold flow conditions and ER conditions are in reasonable agreement with available experimental data. ER results indicate that the 9-species mechanism predicts a slightly higher heat release for the diffusion flame than the 7-species mechanism, although the two are very close to each other and only slightly underpredict the experimental data. Use of the compressibility correction yielded a more accurate estimate of the mixing-driven combustion and heat release, but it compromised the results in the shock-induced separation and reattachment along the centerline.

Steady IRS solutions have been obtained for multiple reaction mechanisms, multiple grid sizes, and with multiple distributions of injected fuel. Although ER results indicate that the 7- and 9-species reaction models produce only slightly different solutions, IRS results show a much more dramatic impact. This is because of the

dependence of premixed flame structures on ignition and chain-branching kinetics. The 9-species reaction mechanism would not allow the flame front to propagate through the partially-premixed flow. This is because more complex reaction mechanisms are more sensitive to the simplifications made in the coupling of turbulence and chemistry (constant turbulent Prandtl and Schmidt numbers and assumed lack of dependence of the reaction rates on fluctuations in temperature or concentration). IRS results also showed some sensitivity to grid resolution, especially in the rocket plume where numerous shock waves are present.

Engine operation is also affected by the distribution of fuel within the fuel-air stream. More complete mixing and combustion are obtained with a more even distribution, as is the case when the fuel is distributed evenly between the upstream and downstream injector banks. It appears from the 7-species results that as long as a condition of $\phi = 1$ is maintained globally in the secondary stream, no distribution of fuel possible with the two injector banks located in the isolator region will allow the thermal throat to move to the aft section of the combustor. Thus, the addition of fuel injectors farther downstream may be necessary to provide adequate engine control. However, it is highly likely that the flame propagation will prove slower in experiments than the 7-species model predicts, so no engine modifications should be seriously considered until experiments can be performed to investigate the controllability using only the 22 existing injectors. Experiments might show that the thermal throat location is farther downstream, and they might also demonstrate a higher degree of path dependence.

If experimental results indicate that the flame propagation is reasonably close to that predicted by the 7-species model, then there should be little risk of flameout during

mode transition. However, since results obtained with the 7-species model are not consistent with estimates of the turbulent flame speed, the possibility of flameout can not be discounted until experimental results are obtained.

Although further development of modeling capabilities will be quite difficult without experimental data, future research should include investigation of the issues uncovered in this work: validation of reaction mechanisms, inclusion of the dependence of reaction rates on temperature and molar density fluctuations, and inclusion of variable turbulent Schmidt and Prandtl number effects.

Because of limitations on the experimental apparatus, all of the chamber pressures simulated in the CFD work will not be possible to duplicate in tests. Since the flowfield is mostly dependent upon $p_c / p_{t,i}$, lower inlet total pressures may be necessary to produce similar flowfields in experiment. Because the CFD work has predicted that stable engine operation is possible at $p_c / p_{t,i} > 23.4$, early IRS experiments should focus on cases with $p_c / p_{t,i}$ at or above that level. Such cases will be far more likely to be useful in validating CFD models. Also, since the CFD work has predicted that the establishment of a thermal throat is possible for $p_c / p_{t,i} > 46.9$, IRS tests which depend upon thermally choked operation will need to be started at such conditions before the actual test conditions can be achieved. In fact, if the 7-species mechanism overpredicts the engine's tendency to thermally choke, then an even higher initial $p_c / p_{t,i}$ may be necessary.

References

[1] Trefny, C. J. "An Airbreathing Launch Vehicle Concept for Single Stage to Orbit," AIAA 99-2730, 35th AIAA/ASME/SAE/ASEE Joint Propulsion Conference and Exhibit, Jun. 20-23, 1999.

[2] Steffen, C. J. and Youngster, S. "Computational Analysis of the Combustion Process in and Axisymmetric, RBCC Flowpath," NASA TM 2001-210679.

[3] Kamhawi, H., Krivanek, T. M., Thomas, S. R., and Walker, J. F. "Direct-Connect Ejector Ramjet Combustor Experiment," AIAA Paper 2003-0016, Jan. 2003.

[4] Steffen, C. J., Bond, R. B., and Edwards, J. R. "Three dimensional CFD Analysis of the GTX Combustor," JANNAF CS/APS/PSHS/MSS Joint Meeting, Apr. 8-12, 2002.

[5] Bond, R. B. and Edwards, J. R. "CFD Analysis of an Independently Fueled Ramjet Stream in an RBCC Engine," AIAA Paper 2003-0017, Jan. 2003.

[6] Hirsch, C. *Numerical Computation of Internal and External Flows: Volume 2, Computational Methods for Inviscid and Viscous Flows*, John Wiley and Sons, Chichester, 1990.

[7] McDaniel, K. S. "Three Dimensional Simulation of Time-Dependent Scramjet Isolator / Combustor Flowfields Implemented on Parallel Architectures," Master's Thesis, North Carolina State University, 2000.

[8] McBride, B. J., Gordon, S., Reno, M. A. "Coefficients for Calculating Thermodynamic and Transport Properties of Individual Species," NASA TM-4513, 1993.

[9] White, F. M. *Viscous Fluid Flow*, McGraw Hill, Boston, 1991.

[10] Wilke, C. R. "A Viscosity Equation for Gas Mixtures," *Journal of Chemical Physics*, Vol. 18, No. 4, 1950.

[11] Wilcox, D. C. *Turbulence Modeling for CFD, 2nd Edition*, DCW Industries, La Cañada, California, 1998.

[12] Jachimowski, C. J. "An Analytical Study of the Hydrogen-Air Reaction Mechanism with Application to Scramjet Combustion," NASA TP-2791, Feb. 1988.

[13] Drummond, J. P. and Rogers, R. C. "A Numerical Model for Supersonic Reacting Mixing Layers," *Computer Methods in Applied Mechanics and Engineering*, Vol. 64, 1987, pp. 39-60.

[14] Eklund, D. R. and Stouffer, S. D. "A Numerical and Experimental Study of a Supersonic Combustor Employing Swept Ramp Fuel Injectors," AIAA Paper 94-2819, Jun. 1994.

[15] Menter, F. R. "Improved Two-Equation $k-\omega$ Turbulence Models for Aerodynamic Flows," NASA TM-103975, 1992.

[16] Wilcox, D. C. "Progress in Hypersonic Turbulence Modeling," AIAA Paper 91-1785.

[17] Edwards, J. R. "A Low-Diffusion Flux-Splitting Scheme for Navier-Stokes Calculations," *Computers and Fluids*, Vol. 26, No. 6, 1997, pp. 635-659.

[18] Roy, C. J. and Edwards, J. R. "Numerical Simulation of a Three-Dimensional Flame / Shock Wave Interaction," *AIAA Journal*, Vol. 38, No. 5, 2000, pp. 745-753.

[19] McDaniel, K. S. and Edwards, J. R. "Simulation of Thermal Choking in a Model Scramjet Combustor," AIAA Paper 99-3411, Jun. 1999.

[20] McDaniel, K. S. and Edwards, J. R. "Three-Dimensional Simulation of Thermal Choking in a Model Scramjet Combustor," AIAA Paper 2001-0382, Jan. 2001.

[21] McBride, B. J. and Gordon, S. "Computer Program for Calculation of Complex Chemical Equilibrium Compositions and Applications II: User's manual and Program Description," NASA Reference Publication 1311, June 1996.

[22] Bond, R. B. and McRae, D. S. "A Conservative Interblock Communication Algorithm for Dynamically Discontinuous Block Boundary Grids," Proceedings, 6th International Conference on Numerical Grid Generation in Computational Field Simulation, Whistler, Canada, Sep. 2000, pp. 119-130.

[23] Bond, R. B. "A Conservative Interblock Communication Algorithm for Dynamically Discontinuous Multiblock Interface Grids," Master's Thesis, North Carolina State University, 2001.

[24] Bond, R. B. and McRae, D. S. "Testing of an Interblock Communication Algorithm for Dynamically Discontinuous Interfaces in 3-D Flow Fields," Proceedings, 7th International Conference on Numerical Grid Generation in Computational Field Simulation, Honolulu, Jun. 2002, pp. 539-547.

[25] Goyne, C. P., Rodriguez, C. G., Krauss, R. H., McDaniel, J. C., and McClinton, C. R. "Experimental and Numerical Study of a Dual-Mode Scramjet Combustor," AIAA Paper 2002-5216.

[26] Goyne, C. P., McDaniel, J. C., Quagliaroli, T. M., Krauss, R. H., and Day, S. W. "Dual-Mode Combustion of Hydrogen in a Mach 5, Continuous Flow Facility," *Journal of Propulsion and Power*, Vol. 17, No. 6, 2001, pp. 1313-1318.

[27] Glassman, I. *Combustion*, Academic Press, San Diego, 1996.

[28] Anderson, J. D. *Modern Compressible Flow*, McGraw Hill, Boston, 1990.

[29] Zimont, V. L., Biagioli, F., and Syed, K. J. "Modeling Turbulent Premixed Combustion in the Intermediate Steady Propagation Regime," *Progress in Computational Fluid Dynamics*, Vol. 1, No. 1, 2001, pp. 14-28.

[30] Chen, M., Herrmann, M., and Peters, N. "Flamelet Modeling of Lifted Turbulent Methane/Air and Propane/Air Jet Diffusion Flames," *Proceedings of the Combustion Institute*, Vol. 28, 2000, pp. 167-174.

[31] *CHEMKIN: A Software Package for the Analysis of Gas-Phase Chemical and Plasma Kinetics*, Reaction Design, 2000.

[32] *PREMIX: A Program for Modeling Steady, Laminar, One-Dimensional Premixed Flames*, Reaction Design, 2000.